CORROSION BEHAVIOUR OF MATERIALS FOR THE NUCLEAR HIGH LEVEL WASTE STORAGE APPLICATION

By

PRADEEP KUMAR SAMANTAROY

Enrolment No.: CHEM02200804008

Indira Gandhi Centre for Atomic Research,

Kalpakkam 603 102, INDIA

A thesis submitted to the
Board of Studies in Chemical Sciences

In partial fulfillment of requirements
For the Degree of

DOCTOR OF PHILOSOPHY

of

HOMI BHABHA NATIONAL INSTITUTE

November, 2013
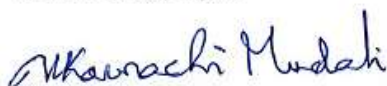
Homi Bhabha National Institute

Recommendations of the Viva Voce Board

As members of the Viva Voce Board, we certify that we have read the dissertation prepared by **Pradeep Kumar Samantaroy** entitled *"Corrosion behaviour of materials for the nuclear high level waste storage application"* and recommend that it may be accepted as fulfilling the dissertation requirement for the Degree of Doctor of Philosophy.

_____ Date: 29.04.14
Chairman – **Prof. S. Rangarajan**
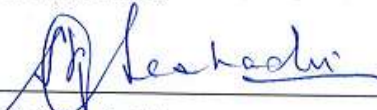
_____ Date: 29|4|14
Guide / Convener – **Prof. U. Kamachi Mudali**

_____ Date: 29.04.14
Member 1 – **Prof. C. Mallika**

_____ Date: 29|4|14
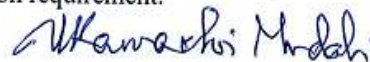Member 2 – **Prof. B. Purnachandra Rao**

_____ Date: 29.04.14
External Examiner – **Prof. S. K. Seshadri**

Final approval and acceptance of this dissertation is contingent upon the candidate's submission of the final copies of the dissertation to HBNI.

I hereby certify that I have read this dissertation prepared under my direction and recommend that it may be accepted as fulfilling the dissertation requirement.

Prof. U. Kamachi Mudali
Supervisor and Convener

Date: 29|4|14
Place: Kalpakkam

STATEMENT BY AUTHOR

This dissertation has been submitted in partial fulfillment of requirements for an advanced degree at Homi Bhabha National Institute (HBNI) and is deposited in the Library to be made available to borrowers under rules of the HBNI.

Brief quotations from this dissertation are allowable without special permission, provided that accurate acknowledgement of source is made. Requests for permission for extended quotation from or reproduction of this manuscript in whole or in part may be granted by the Competent Authority of HBNI when in his or her judgment the proposed use of the material is in the interests of scholarship. In all other instances, however, permission must be obtained from the author.

(PRADEEP KUMAR SAMANTAROY)

DECLARATION

I, hereby declare that the investigation presented in this thesis has been carried out by me. The work is original and has not been submitted earlier as a whole or in part for a degree /diploma at this or any other Institution/ University.

(PRADEEP KUMAR SAMANTAROY)

List of Publications Arising from the Thesis

Journal

1) "Corrosion behavior of Alloy 690 and Alloy 693 in simulated nuclear high level waste medium", Pradeep Kumar Samantaroy, Girija Suresh, Ranita Paul, U. Kamachi Mudali and Baldev Raj, *Journal of Nuclear Materials*, **2011,** *418*, 27-37.

2) "Effect of heat treatment on corrosion behavior of Alloy 690 and Alloy 693 in simulated nuclear high-level waste medium", Pradeep Kumar Samantaroy, Girija Suresh and U. Kamachi Mudali, *Corrosion*, **2012,** *68,* 046001-1-046001-13.

3) "Corrosion behavior of Alloy 600 in simulated nuclear high level waste medium", Pradeep Kumar Samantaroy, Girija Suresh, N. G. Krishna and U. Kamachi Mudali, *Journal of Materials Engineering and Performance*, **2013,** *22,* 1041-1053.

4) "Corrosion enhancement of Ni base superalloys by laser surface melting", Pradeep Kumar Samantaroy, Girija Suresh, Rakesh Kaul and U. Kamachi Mudali, *Surface Engineering*, **2013,** *29,* 522-530.

5) "Effect of heat treatment on pitting corrosion resistance of nickel based superalloys in acidic chloride medium", Pradeep Kumar Samantaroy, Girija Suresh and U. Kamachi Mudali, International *Journal of Material Science*, **2013,** *3,*170-178.

6) "Corrosion investigation of nickel base superalloys in simulated high level waste medium using electrochemical impedance spectroscopy", Pradeep Kumar Samantaroy, Girija Suresh and U. Kamachi Mudali, (communicated).

7) "Intergranular corrosion behavior of nickel base superalloys", Pradeep Kumar Samantaroy, Girija Suresh, T. Nandakumar and U. Kamachi Mudali, (to be communicated).

Conference Proceedings & Presentations:

1) **Pradeep Kumar Samantaroy**, Girija Suresh, Ranita Paul and U. Kamachi Mudali, "Corrosion resistance of Ni 690 and Ni 693 in simulated nuclear high level waste", edited by T.S. Sudarshan, U. Kamachi Mudali and Baldev Raj, Surface Modification Technology, XXIII (2009), pp. 353-360.

2) **Pradeep Kumar Samantaroy**, Girija Suresh and U. Kamachi Mudali, Effect of heat treatment on corrosion behavior of Alloy 690 and Alloy 693 in simulated nuclear high level waste medium, <u>International Conference on Advanced Materials - 2011 (ICAM-2011)</u>, Coimbatore, Dec. (2011).

3) **Pradeep Kumar Samantaroy**, Girija Suresh and U. Kamachi Mudali, "Pitting corrosion behavior of heat treated nickel base superalloys in acidic chloride medium", <u>16th National Congress on Corrosion Control (16th NCCC)</u>, Kolkata, India, Aug. (2012).

4) **Pradeep Kumar Samantaroy**, Girija Suresh, Rakesh Kaul and U. Kamachi Mudali, "Corrosion behavior of laser surface melted nickel base superalloys in simulated nuclear high level waste medium", <u>16th Asian Pacific Corrosion Control Conference (16th APCCC)</u>, Kaohsiung, Taiwan, Oct. (2012).

5) **Pradeep Kumar Samantaroy**, Girija Suresh, U. Kamachi Mudali, "Studies on nickel base superalloys for nuclear high level waste storage application", <u>International Corrosion Prevention Symposium for Research Scholars (CORSYM-2013)</u>, Chennai, India, 28 Feb-02 Mar (2013).

Awards

1) **1st Prize for Oral Presentation: Pradeep Kumar Samantaroy**, Girija Suresh and U. Kamachi Mudali, "Pitting corrosion behavior of heat treated nickel base superalloys in acidic chloride medium", 16th National Congress on Corrosion Control (16th NCCC), Kolkata, India, Aug. (2012)

(PRADEEP KUMAR SAMANTAROY)

Dedicated To…

My Beloved Parents

and

My Brother

ACKNOWLEDGEMENTS

CONTENTS

CHAPTER 4

CHAPTER 5

CHAPTER 6

CHAPTER 7

SYNOPSIS

Management of the highly radioactive spent fuel discharged from nuclear reactors has been considered as an important issue owing to economic and social implications associated with it. Though nuclear industries adopting closed fuel cycle are able to execute the reprocessing of spent nuclear fuel, various issues need to be solved for the management of waste generated from different stages of reprocessing. Owing to the high radioactivity associated with the nuclear waste, it must be managed carefully. Reprocessing, refabrication and management of radioactive waste are the three major steps identified to achieve success in the back-end of nuclear fuel cycle [1-5]. Nuclear waste comprises a variety of materials requiring different types of treatment for its safe disposal. The time required for processing of the spent fuel is one of the major factors in managing the nuclear waste, as this depends on the type of radioactive isotopes produced and particularly the half life characteristics of each of these isotopes.

Based on the specific activity, the dose rate, the radiotoxicity, the origin of waste, its physico-chemical nature, type or radiation, half life of the nuclides etc. various classification systems are available to categorize radioactive wastes. A general classification of radioactive wastes, on the basis of their physical state is

(a) Liquid Waste

(b) Solid Waste and

(c) Gaseous Waste

As the work reported in the present thesis is related to only liquid waste, further discussions have been focused towards liquid waste.

Three general principles employed in the management of liquid radioactive waste [6] are:

(a) *Dilute and disperse:* A method followed when the radioactivity in the effluent can be reduced to levels acceptable for discharge into the environment.

(b) *Concentrate and contain:* A method adopted for liquid waste with a high level of radioactivity and toxic materials. The radioactive materials are concentrated by volume reduction and the waste stored in special tanks until further treatment.

(c) *Delay and decay:* In this method, the waste containing short half life elements are held in a suitable container over a certain period, until the radioactivity is reduced to a level acceptable for discharge or for further treatment.

Out of these three methods, the first two are also used in the management of non-radioactive wastes. However, delay and decay is unique to radioactive waste management; it means that the waste is stored and its radioactivity is allowed to decrease naturally through decay of the radioisotopes present in it. According to the amount and type of radioactivity, the nuclear waste materials can be classified under three categories, namely low level waste (LLW), intermediate level waste (ILW) and high level waste (HLW).

(a) Low Level Waste:

LLW includes items that have been contaminated with radioactive material or have become radioactive through exposure to neutron radiation. This type of waste is generated from hospitals, laboratories and industry as well as in every stage of the nuclear fuel cycle. It includes many kinds of materials such as paper, rags, tools, clothing, shoe covers, filters, fireproof fabrics and protective plastic sheets used in maintenance work, and equipment parts and pipes removed from a nuclear power plant.

The level of radioactivity and the half life of the radioactive isotopes in LLW are relatively small. Such waste is comparatively easy to dispose. Storing the waste for a period of 10 to 50 years will allow most of the radioactive isotopes in LLW to decay, at which point the waste can be disposed off as normal waste. LLW is generally buried in shallow landfill sites.

(b) Intermediate Level Waste:

ILW contains higher amount of radioactivity and in some cases it requires shielding when handled. This waste includes the ion exchange resins used to purify the water circulating through the reactor, chemical sludge and metal reactor fuel cladding, as well as contaminated materials from reactor decommissioning. It may be solidified in concrete or bitumen for disposal. The short-lived waste other than fuel materials from reactors is buried in shallow repositories, while the long-lived waste which are generated from fuel fabrication and fuel-reprocessing operations is deposited in deep underground facilities.

(c) High Level Waste:

HLW is the first cycle raffinate generated from spent nuclear fuel reprocessing and consist of unrecovered uranium, plutonium, fission product elements and other corrosion products leached from clad. The yield of the fission products depends on the type of fissile atom loaded in the reactor, burn-up and the neutron energy. Most of the radioactive isotopes in HLW emit large amount of radiation. Some of them have extreme long half-lives requiring long time periods before the waste settles to safe

levels of radioactivity. While it is only 3% by volume of total waste, it holds 95% of the radioactivity. It generates considerable amount of heat and requires cooling as well as special shielding during handling and transport. The HLW is vitrified by incorporating it into borosilicate glass and is sealed inside canisters for eventual disposal into deep underground.

The Constituents of HLW are

(a) *Corrosion products:* In the case of stainless steel as clad tubes for containing fuel, depending of the burn up the clad corrodes in boiling nitric acid used for dissolution. The reprocessing plant components for spent nuclear fuels are normally constructed from stainless steel. As corrosion of the clad tubes and of vessels inner surfaces takes place because of the use of boiling nitric acid, the solution will contain primarily iron, chromium, nickel and manganese.

(b) *Fission products:* Depending on the composition of the fuel, the fission products Cs, Rb, Sr, Ba, Ru, Mo, Zr, Pd, Tc, Rh, Te, Sb and rare earths have been observed to be present in HLW after reprocessing.

(c) *Unextracted uranium and plutonium:* Although the basic objective of the reprocessing plant is to separate uranium and plutonium from the dissolved fuel solution for subsequent reuse, the separation can never be perfect and traces of uranium and plutonium will end up along with the fission products in the waste solution.

(d) *TRU elements:* The trans-uranium elements neptunium, americium and curium are formed from uranium by neutron capture followed by β-decay. These elements are α-active and are of particular concern in long-term waste management because their half-lives are very long.

(e) *Chemical additives:* Variety of chemicals like HNO_3, Al, Na^+, PO_4^{3-}, SO_4^{2-}, Cl^-, F^- etc. introduced at various stages of reprocessing are present in HLW.

(f) *Organic impurities:* Organic materials like dibutylphosphoric acid and monobutylphosphoric acid, which are the degraded products of tributyl phosphate dissolve in nitric acid, and the solvent kerosene and tributylphosphate form emulsions. These components, if present in significant amounts, could cause difficulties during the waste treatment steps.

Disposal of HLW:

The procedure for the disposal of high level nuclear waste is complex, unlike the LLW and ILW. The methods for the disposal of nuclear waste include:

(i) *Short term storage:* Short term storage will reduce the radioactivity of the HLW (raffinate) significantly. The reduction in radioactivity during short term storage makes handling and shipment of the waste much easier. After short term storage, the waste will be sent for transmutation or long term storage.

(ii) *Long term storage:* Long term refers to a period of thousands of years. The waste must not be allowed to escape into the outside environment by anyway, which includes accidental uncovering, leaching of the waste into the water resources and exposure due to earthquake or other geological activities.

(iii) *Transmutation:* Transmutation is the transformation of one element into another. The goal of transmutation in radioactive waste disposal is to transmute long half-life, highly radioactive elements into shorter half life and low radioactive waste elements.

Prior to vitrification and deep geological disposal, the HLW is stored in tanks having capacities varying from a few hundred to lakhs of litres. Corrosion and tank integrity are major issues concerning the personnel and environmental safety. Carbon steel and austenitic stainless steels like 304L and 316L are widely used in the nuclear industries for waste storage. Out of these steels, some are susceptible to sensitization in the welded zones, which involves chromium depletion at grain boundaries. These alloys also suffer from pitting corrosion and transgranular stress corrosion cracking (TGSCC) in chloride containing solutions [7]. In order to minimize these problems, austenitic nickel-based alloys serve as a good alternative, because of their better corrosion resistance, thermal conductivity and mechanical properties. In the electrochemical series, nickel is more noble than iron [8]. Thus, in reducing environments, the corrosion resistance of Ni is better than iron. Alloying with chromium provides superior corrosion resistance in both reducing and oxidizing environments. Nickel based alloys have a higher tolerance for alloying elements in solid solution than stainless steels and other iron based alloys, while maintaining good metallurgical stability. Alloy 690 is therefore used in many nuclear and petrochemical industries [9], and has been suggested as an alternate material for 304L stainless steel.

The main objective of the present thesis is to investigate the corrosion behaviour of new materials proposed for HLW storage application. Corrosion measurements were carried out on three nickel based superalloys (Alloy 600, Alloy 690 and Alloy 693) in synthetic HLW solution simulated with fission and corrosion product elements in 3M HNO_3. Heat treatment and surface modification were carried out to evaluate the change in corrosion behaviour of these materials. The thesis consists of seven Chapters and the summary of each chapter is given below.

Chapter 1

A brief introduction to the origin of nuclear waste and the requirement of safe storage is discussed in Chapter 1. The reprocessing of spent nuclear fuel for the extraction of uranium and plutonium and for closing the fuel cycle are also discussed in this Chapter. The reprocessing of spent nuclear fuel is carried out by two different processes; (i) aqueous process and (ii) non-aqueous process. The aqueous process is well established and has been employed in all thermal reactors. The most popular aqueous method for reprocessing is the PUREX (Plutonium and Uranium Recovery by Extraction) process. The main goal of this method is to separate uranium and plutonium from the fission products and from one another. The first step of this process is the dissolution of irradiated fuel in aqueous nitric acid. Uranium and Plutonium are subsequently transferred to an organic phase by intensive mixing and extracting with an organic solvent (30% Tributyl Phosphate in Dodecane or n-paraffin hydrocarbon, NPH). While Uranium and Plutonium go to the organic phase, the fission products, other impurities and corrosion products remain in the aqueous nitric phase. The organic phase partitioned enables to separate Uranium and Plutonium from one another. The remaining aqueous phase comprising all the metal ions except the fuel elements, in nitric acid medium is known as HLW or raffinate.

Chapter 2

This Chapter discusses the literature data available and the experience of various countries towards nuclear waste treatment and selection of materials for the storage of different kind of wastes. A summary of the materials used at various waste storage sites all around the world is reported in this Chapter. Carbon steel, stainless steel 348, 316L and 304L are the

commonly used materials for the purpose of waste storage at various sites. This Chapter also gives a brief account of the failures faced at different sites during HLW storage. The necessity for the introduction of advanced materials for waste storage tank and the scope for the thesis work are included in this Chapter.

Chapter 3

Chapter 3 describes briefly the criteria for materials selection for the present study, details about nuclear HLW and the experimental techniques employed for the electrochemical measurements and metallurgical characterization for evaluating the corrosion behaviour.

The experimental techniques used in the present thesis are described below. The corrosion behavior of the alloys were evaluated using various electrochemical techniques. Potentiodynamic anodic polarization studies provided the data on the corrosion potential, passivation current density, transpassive potential and the passive range. Using the data, a comparison was made on the corrosion resistance of nickel based superalloys under various conditions like as-received, solution annealed, sensitized and surface melted after laser treatment. Electrochemical impedance spectroscopy was used to analyze the behaviour of passive film formed at the metal and solution interface in simulated HLW medium. To measure the degree of sensitization (DOS) of sensitized, solution annealed and laser surface melted (LSM) specimens, double loop electrochemical potentiokinetic reactivation (DL-EPR) test was carried out. Pitting corrosion resistance of these materials was also compared using the electrochemical techniques discussed above.

Optical microscopy and scanning electron microscopy (SEM) images were used to investigate the microstructure as well as corrosion attack on the surface of specimens. X-ray

photoelectron spectroscopy was employed to evaluate the surface composition of passive film formed over the specimens in the simulated HLW medium. X-ray Diffraction technique was used to reveal information regarding the phase changes after laser surface melting.

Chapter 4

The corrosion behaviour of the three as-received nickel based superalloys (Alloy 600, 690 and 693) in simulated HLW medium is described in Chapter 4. Electrochemical studies were carried out in simulated HLW solution in 3M HNO_3, using potentiodynamic anodic polarization and electrochemical impedance spectroscopic techniques. The specimens were etched electrolytically and examined under SEM. All the alloys, in the as-received condition were found to possess good corrosion resistance in simulated HLW, at 25 ^{0}C as well as at 50 ^{0}C. X-ray photoelectron spectroscopic studies were carried out, to investigate the passive film formed in simulated HLW medium. The passive films formed on the Alloy 690 and Alloy 693 were found to consist of a mixed oxide of Ni-Cr-Fe in simulated HLW, only oxides of Cr could be observed in Alloy 600. In the as-received condition, Alloy 690 exhibited superior corrosion resistance compared to Alloy 693, followed by Alloy 600 in simulated HLW medium.

Studies were undertaken to evaluate the pitting corrosion resistance in 3 M HNO_3 containing various concentrations of chloride ions (500, 1000, 2000 and 3000 ppm) under aerated condition. With increase in chloride ion concentration the passivation current density was found to increase, whereas the pitting potential decreased. This indicated the decrease in pitting corrosion resistance with increase in chloride ion concentration. The population of

pits was also observed to increase with chloride ion concentration. Alloy 690 was found to possess superior pitting corrosion resistance compared to Alloy 693 and Alloy 600.

Huey test as per ASTM A262 practice C was carried out to examine the intergranular corrosion resistance of the alloys in 65 % boiling nitric acid solution for five periods with the duration of 48 hour in each period. The weight loss was measured after each period of testing. The tested specimens were observed under SEM. Severe grain boundary attack was observed in Alloy 693 with dissolution of matrix. However, Alloy 690 showed excellent resistance towards intergranular corrosion compared to Alloy 693 and Alloy 600. The microstructural investigations and the evaluation of corrosion resistance of the three alloys in the as-received condition were described in details in Chapter 4.

Chapter 5

The chemistry and structure of materials play a critical role in improving the resistance towards corrosion attack. Heat treatment can affect the properties of materials by way of inducing chromium depletion, segregation of impurities to grain boundaries, and modifying the composition, structure and distribution of intergranular carbide precipitates [10]. Chapter 5 describes the effect of heat treatment on corrosion behaviour of nickel based superalloys in simulated HLW medium. Heat treatment facilitated the three nickel based superalloys to undergo solution-annealing followed by sensitization. SEM study revealed the effect of heat treatment on grain size and dissolution or enrichment of precipitates. The DL-EPR test was carried for all the alloys in 0.5 M H_2SO_4 medium containing 0.0001 M KSCN. The ratio of peak reactivation current density to the peak anodic current density was used as the basis for measuring the DOS. The solution-annealed specimens showed very low DOS. Alloy 690

was found to contain no reactivation peak, due to the high chromium concentration. Passivation has been observed to be stable throughout the back scanning period, indicating that the extent of Cr-depletion adjacent to the grain boundaries was insignificant even after sensitizing the specimens at 700^{0}C for 1 hour. The corrosion behaviour of heat treated specimens was investigated in simulated HLW solution in 3M HNO_3. All the alloys were found to possess good corrosion resistance in 3 M HNO_3 and in simulated HLW at 25 ^{0}C, in the solution-annealed condition. Increasing the solution temperature to 50 ^{0}C favoured the corrosion potential as well passivation current density to increase. The sensitized specimens were found to possess a lower corrosion resistance compared to solution-annealed specimens in 3 M HNO_3 as well as in simulated HLW. However, the passivation current densities were observed to be in close proximity. Pitting corrosion resistance of the heat treated specimens were measured in 3 M HNO_3 containing various concentrations of chloride ions. The passivation current density was observed to increase with increase in chloride ion concentration. Similarly, the pitting potential and hence pitting corrosion resistance decreased with increase in chloride ion concentration.

Chapter 6

In Chapter 6, the effect of surface modification by laser surface melting, on the corrosion behaviour of nickel based superalloys (Alloy 600, 690 and 693) in simulated HLW and in chloride medium is discussed. In the last few decades, laser surface modification of materials has found wide ranging technological applications in enhancing surface properties by altering the surface chemistry and structure. The advantages in laser surface modification is the rapid heating and melting which facilitates the feasibility of extended solid solution,

fine microstructure, composition homogenization, excellent metallurgical interface etc. [11-14]. Short processing time, flexibility in operation, economy in time, energy, material consumption etc., [15-19] are the added advantages of laser surface modification over conventional processes.

In the fabrication of waste storage tanks, sensitization occurs during welding. The work reported in Chapters 4 and 5 indicated that Alloy 600 and Alloy 693 are susceptible to sensitization. Sensitization can be avoided by solution-annealing and rapid cooling through the sensitization temperature range. However, it is difficult to control the experimental parameters during such treatments and practically impossible to subject bulk components like HLW storage tanks in nuclear industries to these heat treatments. Further, large thermal stresses may be induced during such rapid cooling. Thus, laser surface melting is a suitable method for eliminating sensitization of heat affected zones of welded areas of various components used for HLW storage [20]. Chapter 6 presents the results of the corrosion studies performed on Ni based alloys after modifying their surfaces by laser melting. Surface characterization of the laser melted specimens was carried out by optical microscopy, SEM and X-ray diffraction. Laser surface melting of the Ni alloys resulted in cellular microstructure without any precipitates. These alloys found to possess same crystal structure (cubic) in both as-received as well as LSM condition. DL-EPR test in 0.5 M H_2SO_4 containing 0.0001 M KSCN showed low DOS compared to the solution-annealed specimens, indicating the absence of chromium depleted zones after laser surface melting. Laser surface melting resulted in the enhancement of corrosion resistance of the alloys in simulated HLW compared to the as-received and solution-annealed specimens; nevertheless, no discernable difference could be observed between LSM Alloys 600, 690 and 693 in

simulated HLW. The LSM specimens showed better pitting corrosion resistance in chloride medium when compared to the as-received and solution-annealed specimens, due to the refinement of microstructure and dissolution of precipitates, which are the initiation sites for pitting. Superior pitting corrosion resistance was exhibited by LSM Alloy 690 when compared to Alloy 600 and 693.

Chapter 7

In this Chapter, a summary of the investigations performed on the corrosion behavior of Ni based alloys namely Alloy 600, 690 and 693 in simulated HLW solution in 3 M HNO_3 and in different concentrations of chloride ions in the as-received as well as different heat treated condition is discussed and the scope for future research based on the present work has been proposed. Though all the three materials showed good corrosion resistance in simulated HLW medium, Alloy 690 was found to possess better corrosion resistance compared to Alloy 693 followed by Alloy 600. Solution-annealing aided in improving the corrosion resistance of the alloys. Laser surface melting using CO_2 laser had enhanced the general as well as pitting corrosion resistance of all the specimens. Alloy 690 was found to possess excellent IGC resistance compared to Alloy 600 and Alloy 693, which could be attributed to the higher chromium content and lower carbon percentage. The corrosion resistance of the alloys investigated in the present thesis work follows the order:

Alloy 690 > Alloy 693 > Alloy 600

For plant applications, the corrosion behavior of welded specimens of Ni based alloys needs to be established, since the welded region (heat affected zone) in the waste storage tank is prone to sensitization. Since, online monitoring of corrosion behavior can be realized from

electrochemical noise measurements, electrochemical probes based on this technique can be adopted for evaluating the influence of temperature, acid concentration and oxidizing ions present in HLW on the corrosion propagation in the waste storage containers. Owing to the high burn-up of FBR fuels the concentration of fission products is much higher in the HLW generated from the reprocessing of FBR spent fuels. Hence, studying the corrosion behaviour of Ni based alloys in the HLW of spent fuels of FBRS and identifying cost-effective corrosion resistant materials for the long term storage of waste in acid medium are within the scope for future work.

References

1. A. Kakodkar, Conf. on Chemical Engineering Congress (CHEMCON-2000), Calcutta, (2000), Paper Nos. CHE 6, CHE 14.

2. Baldev Raj and U. Kamachi Mudali, Prog. Nucl. Ener., 48 (2006) 283.

3. Baldev Raj, U. Kamachi Mudali, T. Jayakumar, K. V. Kasiviswanathan and R. Natarajan, Sadhana, 25 (2000) 519.

4. U. Kamachi Mudali, R. K. Dayal and J. B. Gnanamoorthy, J. Nucl. Mater., 73 (1993) 203.

5. U. Kamachi Mudali, A. Ravishankar, S. Ningshen, S. Girija, R. Sole and K. Thyagarajan, Energy Procedia, 7 (2011) 468.

6. IAEA Safety Standard Series, No-WS-R-2 (2000).

7. L. Vehovar and M. Tandler, Nucl. Eng. Des., 206 (2001) 21.

8. R. B. Rebak and P. Crook, Adv. Mater. Processes, 157 (2000) 37.

9. A. J. Bard, J. Jordan and R. Prarsons, (Eds.), "Standard Potentials in Aqueous Solutions," Marshal Dekker, New York, 1985.

10. J. Kocourek, Nucl. Eng. Int., 39 (1994) 22.

11. M. Casales, M. A. Espinoza-Medina, A. Martinez-Villafane, V. M. Salinas-Bravo and J. G. Gonzalez-Rodriguez, Corrosion, 56 (2000) 1133.

12. Z. D. Cui, H. C. Man, F. T. Cheng and T. M. Yue, Surf. Coat. Tech., 162 (2003) 147.

13. A. Viswanathan, D. Sastikumar, U. Kamachi Mudali, H. Kumar and A. K. Nath, Surf. Eng., 23 (2007) 123.

14. C. T. Kwok, K. H. Lo, W. K. Chan, F. T. Cheng and H. C. Man, Corros. Sci., 53 (2011) 1581.

15. R. Vilar, E. C. Santos, P. N. Ferreira, N. Franco and R. C. Da Silva, Acta Mater., 57 (2009) 5292.

16. J. D. Majumdar, R. Galun, B. L. Mordike and I. Manna, Mater. Sci. Eng. A, 361 (2003) 119.

17. C. W. Draper and J. M. Poate, Int. Met. Rev., 30 (1985) 85.

18. W. Darmawan, J. Quesada and R. Marchal, Surf. Eng., 23 (2007) 112.

19. A. R. Shankar, B.J. Babu, R. Sole, U. Kamachi Mudali and H.S. Khatak, Surf. Eng., 23 (2007) 147.

20. C. Huang, Y. Zhang, R. Vilar and J. Shen, Mater. Design, 41 (2012) 338.

LIST OF FIGURES

LIST OF TABLES

CHAPTER **1**

An Introduction to Indian Nuclear Programme and Aqueous Reprocessing

An Introduction to Indian Nuclear Programme and Aqueous Reprocessing

A brief overview of the Indian nuclear programme is discussed in this Chapter. The aqueous reprocessing of spent nuclear fuels for the extraction of uranium and plutonium and for closing the fuel cycle using PUREX (Plutonium and Uranium Recovery by Extraction) process are briefly described. This Chapter also deals with the types of nuclear waste, the requirement and methods adopted for the safe storage of high level waste prior to its safe disposal.

1.1 Introduction

India's economy is growing at the rate of 8 to 9 % every year. A high economic growth rate implies a high growth rate in the consumption of electrical energy. At present, fossil fuels like coal, lignite, oil and natural gas are the major contributors to electricity generation, accounting for nearly 80 % of the electricity produced annually [1]. Renewable sources such as solar power, hydroelectric power, wind energy and biomass power contribute another 18 % to the total electricity produced, whereas nuclear energy contributes only 2.3 %. As estimated, India will need 3400 TWh of electricity annually by 2070 [2], despite of setting a low benchmark of 2000 kWh consumption per capita per annum for the future. The estimated total potential of all renewable resources in India is 1229 TWh [2], which when completely realized will account for only 36.1 % of the total estimated demand of 3400 TWh in 2070. Eventually, about 100 years later, the contribution from fossil fuels will also be dwindled, given the rate at which these are depleting due to their high consumption. The only sustainable energy resource available in the long run is the nuclear energy, which has

the capability to generate sufficient and clean electricity to meet India's growing energy demands. Among the nuclear fuel resources available, uranium resources in India are limited; however, vast resources of thorium are available. In order to fully exploit the available nuclear fuel resources for energy production, a three-stage nuclear program has been envisaged in India. This three stage program is based on a closed fuel cycle involving the reprocessing of spent fuel to recover unused uranium and plutonium for subsequent use as fuels in the reactors.

1.2 The three stage nuclear program

About 13.5 % of the total electricity generated worldwide is from nuclear reactors. At present there are 430 commercial nuclear reactors operating in 31 countries and producing this electricity with a total generating capacity of around 372 GWe [3]. In India 20 reactors are under operation and 7 reactors are under construction [4]. The amount of uranium available in India could set a limitation to the growth of nuclear energy as in the case of fossil fuels. However, the production of Pu-239 and U-233 fissile materials in breeder reactors overcomes this limitation. Pu-239 can be generated from the isotopes, U-238 present in natural uranium and U-233 can be generated by using the fertile thorium with fast breeder reactors. Keeping this in view, India follows a three stage nuclear program linking the fuel cycles of Pressurized Heavy Water Reactors (PHWR), Fast Breeder Reactors (FBR) and thorium based FBRs and Advanced Heavy Water Reactors (AHWR) [5].

India's three-stage nuclear program was formulated by Dr. Homi J. Bhabha in 1950's to secure the country's long term energy issues through the use of uranium and enormous thorium available in the country. A schematic of Indian three stage nuclear program is

depicted in Fig. 1.1. This program is based on a closed fuel cycle, wherein the spent fuel of one stage is reprocessed to produce fuel for the next stage. The closed fuel cycle thus, multiplies manifold the energy potential of the fuel and greatly reduces the quantity of waste generated.
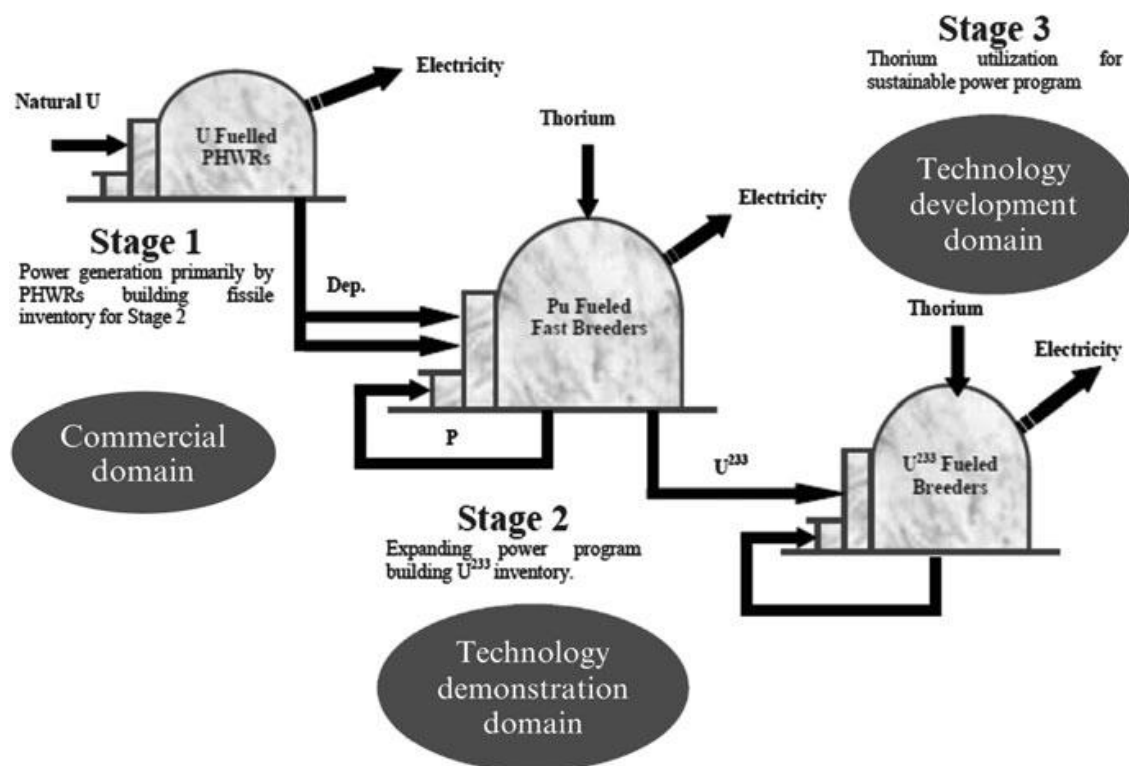
Fig. 1.1: Schematic diagram of Indian nuclear power program [6]

The first stage comprises Pressurized Heavy Water Reactors fuelled by natural uranium, produce electricity while generating Pu-239 as a by-product. Natural uranium contains only 0.7 % of the fissile isotope U-235, which undergoes fission to release energy. The remaining 99.3 % comprises U-238, which is not fissile; however, the fertile U-238 isotope is converted in the nuclear reactor to the fissile element, Pu-239 formed by transmutation of

uranium-238. Almost all the existing base of Indian nuclear power is from the first category of PHWRs, with the exception of two Boiling Water Reactor (BWR) units at Tarapur.

In the second stage, the FBRs are fuelled by mixed oxide of U-238 and Pu-239, recovered by reprocessing of the spent fuel from the first stage reactors. In FBRs, Pu-239 undergoes fission, generating energy and producing Pu-239 by transmutation of U-238. Since FBRs produce energy and fuel, they are termed as Breeders. FBRs produce more fuel than they consume and hence, are technically capable of growing the nuclear capacity to a very high level. Th-232, which constitutes world's third largest reserves in India, is not fissile; therefore, it needs to be converted to a fissile material, U-233, by transmutation in a FBR. This is to be achieved through the second stage of the program, by commercial operation of FBRs. Thorium is used as a blanket material around the fuel in FBR to produce fissile U-233 which will form the fuel for the third stage of the program [5].

In the third stage, the fissile element U-233 will be used in thermal or fast breeder reactors to produce electricity as well as for further breeding of U- 233 from thorium [5]. This would be a thermal breeder reactor which in principle can be refuelled - after its initial fuel charge - using only naturally occuring thorium. According to the three-stage programme, Indian nuclear energy could grow to about 10 GW through PHWRs fueled by domestic uranium and the growth expected to come from FBRs will be about 50 GW [7]. The third stage is to be deployed only after the successful achivement of 2nd stage.

1.3 Spent fuel reprocessing

The fuel discharged from nuclear reactors after maximum burn up is referred to as 'spent fuel' [8, 9]. The spent fuel contains fission fragments from the spontaneous fission of the

fissile elements and transuranic (TRU) actinides produced by the absorption of neutrons in addition to the un-burnt fuel. The spent fuel would be removed from any reactor after it has achieved a significant burn-up. It is both highly radioactive and a rapidly diminishing source of heat. For sustaining nuclear power production, two options exist with regard to the processing of spent fuel which are of relevance and are under consideration at the present juncture. They are the once through cycle with permanent disposal of the spent fuel and the closed fuel cycle with reprocessing. Both options demand efficient and safe waste management strategies and are significantly different with reference to the choice. Without reprocessing, the entire discharged spent fuel, containing about 97 percent unused uranium and transuranium elements, may be required to be managed as long-term waste. With reprocessing, most of these elements removed from the spent fuel and recycled back into the nuclear fuel cycle, where they contribute to the generation of energy by fission and the left-over relatively short half-life, fission product nuclides would be managed as waste.

(i)   Recovery of the valuable fissile constituents (primarily U-235/U-233 and plutonium) for subsequent reuse as recycled fuel

(ii)   Reduction in the volume of high-level liquid waste (HLLW) that must be processed for disposal in a geological repository and

(iii)   Recovery of special isotopes.

The advantage of reprocessing of the spent fuel over once through cycle could be summarized as follows:

➤   Recovers 97 % unused fuel and hence, contributes to energy production by recycling of the fuel elements.

➤   Recovers the other transuranium elements in the spent fuel.

➢ Allows transition to the Fast Breeder cycle of reactor operation.

➢ Makes available, at least 100 times more energy than the option by not reprocessing, opens up a way for utilization of lower grade uranium ore deposits and using thorium as fuel, and reduces the need for uranium enrichment.

➢ Separates the 3-5 percent by volume of highly active fission product waste from spent fuel.

➢ Produces low volumes of liquid waste requiring a relatively short, waste-management interval.

➢ Minimizes the requirement for long-term safety and security considerations.

Two types of techniques mainly available for the reprocessing of spent nuclear fuel are aqueous reprocessing and pyrochemical reprocessing. In aqueous reprocessing, combinations of solvent extraction and ion exchange separation techniques are employed [12, 13]. This technique is a well established process for the reprocessing of thermal and FBR fuels. The pyrochemical process is applicable mainly for the reprocessing of metallic fuel from fast reactors by using electrometallurgical processes.

Reprocessing forms an integral part of the Indian Nuclear Energy Programme because closing the nuclear fuel cycle by reprocessing the spent fuel and recycling of uranium and plutonium back into reactor systems facilitates in exploiting the full potential of nuclear power and maximizes the utilization of the resources [14]. Further, the Indian three-stage nuclear power program can sustain only with efficient reprocessing technology and the associated waste management program in addition to the development of re-fabrication technologies - essentially the closing of the backend of fuel cycle. The initiative for nuclear

fuel reprocessing in India started in 1964 [15]. At present India has three nuclear fuel reprocessing plants; one at Trombay with the reprocessing capacity 60 ton per year, the second and third plants located at Tarapur and Kalpakkam respectively with the capacity of reprocessing 100 ton of power reactor fuel per year. In all the three plants for the reprocessing of spent nuclear fuels, PUREX process has been employed for the separation of U and Pu from the fission products.

1.4 PUREX process

The PUREX process has been the workhorse of fuel reprocessing for the last few decades and no other process developed before or after can claim its versatility [15, 16]. PUREX stands for Plutonium and Uranium Recovery by Extraction, the acronym was given by Lanham and Runion [17]. All commercial reprocessing plants active at present as well as many which have been decommissioned, use the PUREX process. The process was invented in 1947 at the University of Chicago as part of the Manhattan Project. It was first implemented on a large scale at the Savannah River Site in 1954 [18, 19], and has since been adopted by many other countries. The schematic of a typical PUREX process flow sheet is shown in Fig. 1.2 [20]. This process makes use of solvent extraction technique, in which the spent fuel pin is dissolved in nitric acid after chopping to small pieces and extracting the fuel elements U and Pu by an organic solvent, leaving behind minor actinide nitrates and other fission products in the aqueous nitric phase. The organic solvent employed for the separation of U and Pu is 30 % tributyl phosphate (TBP) diluted with 70 % n-dodecane or normal paraffin hydrocarbon (NPH) which being immiscible with nitric acid eventually extracts uranium and plutonium as nitrates, leaving behind fission product nitrates in the aqueous

solution. The process aims at nearly complete recovery of uranium and plutonium with fission product decontamination factors in the range of 10^6-10^8. Countries which have produced significant quantities of plutonium used the PUREX process [21-25]. The flow sheet for this process generally has two product streams and three waste streams: Product streams are uranium nitrate and plutonium nitrate solutions and the waste streams are classified as high active, intermediate and low active wastes according to the levels of radioactivity [26]. The basic steps involved in the PUREX process could be summarized as follows [15, 26]:

(i)   Head end treatment involving chopping of fuel pins, dissolution of fuel pellets in nitric acid, feed clarification and adjustment of the chemical states of the dissolved solution for solvent extraction.

(ii)   Co-decontamination involving extraction of U(VI) and of Pu(IV) in 30 % TBP leaving bulk of the fission products in aqueous phase which goes as high active waste.

(iii) Washing/scrubbing of the organic stream with dilute nitric acid, sometimes using two nitric acid scrubs of different HNO_3 concentration, to backwash some of the fission products co-extracted with uranium and plutonium.

(iv)   Partitioning of uranium and plutonium by selective reduction of Pu(IV) in the organic phase to Pu(III) in the aqueous phase, and back extraction of U(VI) with dilute nitric acid.

(v)   Further treatment of uranium and plutonium in the aqueous streams to obtain U and Pu products of desired purity.

(vi)   Waste management.
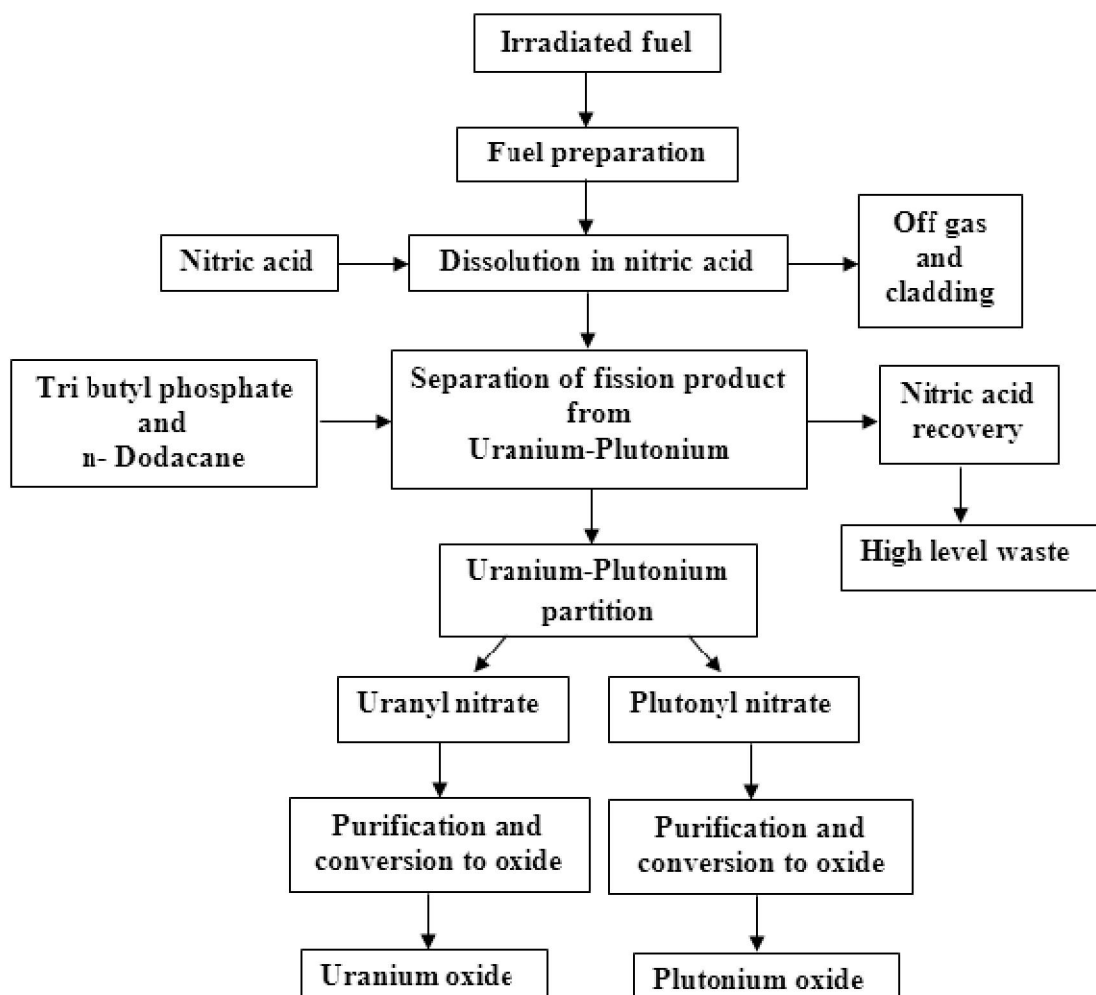
Fig. 1.2: Flow sheet of PUREX process [20]

Although PUREX is a well established and widely used process today, it is far from perfection. One main argument against reprocessing is the concern for nuclear weapons proliferation. In the conventional PUREX reprocessing technology, a pure stream of weapon grade plutonium is separated out of the spent fuel. The plutonium mixed with uranium to fabricate MOX fuel cannot be used as a weapon. Although the final fuel product is not weapon grade nuclear material, the intermediate step in extracting pure plutonium could

allow developed nations to either create weapon materials for their own purposes or increase the threat of theft of the weapon's material from reactor facilities [27]. Another important concern is that with any buildup of uranium or plutonium there is a possibility of critical mass being attained. Although a chain reaction resulting from such a small amount of lowly enriched material would not be devastating, it could result in the direct exposure of workers to high energy gamma and neutron radiation, minor concern for fallout of material into the environment, and decommissioning of the plant. The third and major concern of reprocessing is the volume of waste produced. Ideally, reprocessing of the spent fuel should aim to reduce the radioactivity of waste. While PUREX process accomplishes this to a certain extent, a large quantity of low level radioactive waste is generated in the aqueous reprocessing.

1.5 Waste management after reprocessing

Management of the highly radioactive spent fuel discharged from nuclear reactors has been considered as an important issue owing to economic and social implications associated with it. Though nuclear industries adopting closed fuel cycle are able to execute the reprocessing of spent nuclear fuel, various issues need to be solved for the management of waste generated from different stages of reprocessing. Owing to the high radioactivity associated with the nuclear waste, it must be managed carefully. Reprocessing, refabrication and management of radioactive waste are the three major steps identified to achieve success in the back-end of nuclear fuel cycle [12, 28-31]. Nuclear waste comprises a variety of materials requiring different types of treatment for its safe disposal. The time required for processing of the spent fuel is one of the major factors in managing the nuclear waste, as this

depends on the type of radioactive isotopes produced and particularly the half life characteristics of each of these isotopes.

Three general principles employed in the management of radioactive waste [32, 33] are:

(a) *Dilute and disperse:* A method followed when the radioactivity in the effluent can be reduced to levels acceptable for discharge into the environment.

(b) *Concentrate and contain:* A method adopted for liquid waste with a high level of radioactivity and toxic materials. The radioactive materials are concentrated by volume reduction and the waste stored in special tanks until further treatment.

(c) *Delay and decay:* In this method, the waste containing short half life elements are held in a suitable container over a certain period, until the radioactivity is reduced to a level acceptable for discharge or for further treatment.

Out of these three methods, the first two are also used in the management of non-radioactive wastes. However, delay and decay is unique to radioactive waste management; it means that the waste is stored and its radioactivity is allowed to decrease naturally through decay of the radioisotopes present in it.

In order to manage nuclear wastes, various classification systems are available based on the specific activity, the dose rate, the radiotoxicity, the origin of waste, its physico-chemical nature, type or radiation, half life of the nuclides etc. Based on their physical characteristics, they can be classified as (i) solid waste, (ii) liquid waste and (iv) gaseous waste. Similarly, according to the amount and type of radioactivity, the nuclear waste materials can be classified under three categories, namely Low Level Waste (LLW), Intermediate Level Waste (ILW) and High Level Waste (HLW).

1.5.1 Low Level Waste

LLW includes items that have become contaminated with radioactive material or have become radioactive through exposure to neutron or gamma radiation. Low-level wastes are not spent fuel, milling tailings, reprocessed materials, or transuranic materials. However, "low level" does not mean "not dangerous". The level of radioactivity and the half life of the radioactive isotopes in LLW are relatively less. This type of waste is generated from hospitals, laboratories and industry as well as in every stage of the nuclear fuel cycle. LLW which come from reactors can be divided into two categories: (i) fuel wastes which are fission products that leak out of fuel rods into cooling water and (ii) non-fuel wastes result when stray neutrons bombard any material in the core other than the fuel such as the reactor vessel itself and cause them to become radioactive. LLW contains virtually no alpha emitters, and is comparatively easy to dispose. Storing the waste for a period of about 10 to 50 years will allow most of the radioactive isotopes in LLW to decay, at which point the waste can be disposed off as normal waste. LLW is generally buried in shallow landfill sites. Examples of low-level wastes are

✓ Ion exchange resins and filter materials used to clean water at a nuclear power plant.

✓ Contaminated hand tools, components, piping and other equipment from nuclear power plants and other industries.

✓ Research equipment from laboratories where radioactive materials are used.

✓ Shoe covers, lab coats, cleaning cloths, paper towels etc., used with radioactive material.

✓ Containers, cloth, paper, fluids and equipment in contact with radioactive materials used in hospitals to diagnose or treat a disease.

✓ Filters from sampling devices used to test for airborne radioactive contamination.

✓ Scintillation fluids in which filters from some sampling devices must be dissolved in order to determine the amount of radioactive material present.

✓ Carcasses of animals treated with radioactive materials used in medical or pharmaceutical research.

1.5.2   Intermediate Level Waste

ILW contains higher amount of radioactivity and in some cases it requires shielding for handling. This waste includes ion exchange resins used to purify the water circulating through the reactor, chemical sludge and fuel cladding material as well as contaminated materials from reactor decommissioning. It may be solidified in concrete or bitumen for disposal. The short-lived radioactive waste other than fuel materials from reactors is buried in shallow repositories, while the long-lived waste which are generated from fuel fabrication and fuel-reprocessing operations is deposited in deep underground facilities.

1.5.3   High Level Waste

HLW is the first cycle raffinate generated from the aqueous reprocessing of spent nuclear fuel and it consists of unrecovered uranium and plutonium, fission product elements and other corrosion products leached out from clad. The yield of fission products depends on the type of fissile atom loaded in the reactor, burn-up and the neutron energy. Most of the radioactive isotopes in HLW emit large amount of radiation. Some of them have extremely long half-lives requiring longer time periods before the waste settles to safe levels of radioactivity. While it is only 3 % by volume of total waste, it holds 95% of the radioactivity. It generates considerable amount of heat and requires cooling as well as

special shielding during handling and transport. The HLW is vitrified by incorporating it into borosilicate glass and is sealed inside canisters for eventual disposal into deep underground.

The constituents of HLW are

(a) *Corrosion products:* Depending on the burn-up, the stainless steel clad tubes used to contain the fuel, corrode in boiling nitric acid during the dissolution of spent fuel. The reprocessing plant components for spent nuclear fuels are normally constructed from stainless steel. As corrosion of the clad tubes and of vessels inner surfaces takes place because of the use of boiling nitric acid, the solution will contain primarily iron, chromium, nickel and manganese.

(b) *Fission products:* Depending on the composition of the fuel and burn-up, the fission products Cs, Rb, Sr, Ba, Ru, Mo, Zr, Pd, Tc, Rh, Te, Sb and rare earths have been observed to be present in HLW after reprocessing.

(c) *Unextracted uranium and plutonium:* Although the basic objective of the reprocessing plant is to separate uranium and plutonium from the dissolved fuel solution for subsequent reuse, the separation can never be perfect and traces of uranium and plutonium will end up along with the fission products in the waste solution.

(d) *TRU elements:* The trans-uranium elements neptunium, americium and curium are formed from uranium and plutonium by neutron capture followed by β-decay. These elements are α-active and are of particular concern in long-term waste management because their half-lives are very long.

(e) *Chemical additives:* Variety of chemicals like HNO_3, Al, Na^+, PO_4^{3-}, SO_4^{2-}, Cl^-, F^- etc. introduced at various stages of reprocessing are present in HLW.

(f) *Organic impurities:* Organic materials like dibutyl phosphoric acid and mono butyl phosphoric acid, which are the degraded products of tributyl phosphate dissolve in nitric acid, and the degraded product of the diluents (n-dodecane/NPH) and tributylphosphate form emulsions. These components, if present in significant amounts, could cause difficulties during the waste treatment steps.

1.6 Disposal of nuclear waste

The procedure for the disposal of high level nuclear waste is complex, unlike the LLW and ILW. Methods for the disposal of nuclear waste include:

(a) *Short term storage:* Short term storage will reduce the radioactivity of the HLW (raffinate) significantly. The reduction in radioactivity during short term storage facilitates handling and shipment of the waste much easier. After short term storage, the waste will be sent for transmutation or long term storage.

(b) *Long term storage:* Long term refers to a period of thousands of years. The waste must not be allowed to escape into the outside environment by anyway, which includes accidental uncovering, leaching of the waste into the water resources and exposure due to earthquake or other geological activities.

(c) *Transmutation:* Transmutation is the transformation of one element into another. The goal of transmutation in radioactive waste disposal is to transmute long half-life, highly radioactive elements into shorter half life and low radioactive waste elements.

1.7 HLW management in India

HLW generated during reprocessing of spent nuclear fuels is concentrated by evaporation and stored in stainless steel tanks with the capacity of 250-500 m^3 each. These storage tanks require cooling and continuous surveillance. Liquid storage in stainless steel tanks is at best an interim step and a three-step strategy for the management of HLW has been adopted in India [34-37].

Stage 1: Immobilization of HLW by converting it into inert and stable vitreous matrices

Stage 2: Interim storage under surveillance and cooling

Stage 3: Ultimate disposal of solidified HLW

The vitrification facilities are co-located near the reprocessing plants to avoid long-term transportation of HLW. HLW is transferred from the reprocessing plant to vitrification plant through underground piping. India has a unique distinction of having operating vitrification plants at Tarapur & Trombay and another vitrification plant is under advanced stage of construction at Kalpakkam. A solid storage and surveillance facility (SSSF) has been set up at Tarapur for interim storage of vitrified HLW. An elaborate programme on deep geological disposal is being pursued to realize the third stage of the programme.

The long term strategy for the treatment of HLW would involve its partitioning that would not only result in the reduction of radioactivity but could also have resource advantage. The final utilization/transmutation of the partitioned long lived radionuclides would be evolved based on the available technological options involving FBRs and Accelerator Driven Systems.

Development of ceramic waste forms like synroc, NZP and metal waste forms etc. is also being pursued to address specific waste streams on account of partitioning leading to waste volume reduction and enhanced long term safety. The procedure adopted for radioactive waste management in India is summarized in Fig. 1.3.

CHARACTERIZATION	TREATMENT			CONDITIONING

LL	Liquid	LIQUID WASTE	SOLID WASTE	GASEOUS WASTE	Cementation
		Chemical Treatment	Compaction	Scrubbing	Polymerisation
IL	Solid	Ion Exchange	Incineration	Adsorption/Absorption	Bituminisation
		Reverse Osmosis	Size Fragmentation	Prefiltration	
HL	Gaseous	Evaporation	Repackaging	High Efficiency Filtration	Vitrification

INTERIM STORAGE	DISPOSAL		ENVIRONMENTAL MONITORING/CONTROL
• Alpha Contaminated Waste	LIL Waste Short lived	HLW & Long Lived Waste	• Monitoring of water, soil, vegetation, near waste management facility.
• Wastes requiring treatment / conditioning in future	• Earth/Stone lined trenches		• Monitoring of environment near nuclear facility.
	• Reinforced Concrete trenches	• Deep Geological Disposal	• Institutional control of near surface disposal facility for 300 years.
• Vitrified waste for cooling pending disposal	• Tile Holes		

Fig. 1.3: Radioactive waste management in India [35].

1.8 Summary

Nuclear energy is the only sustainable energy resource available in the long run, as it has the capability to generate sufficient electricity to meet India's growing energy demands. Exploiting the available nuclear fuel resources for energy production is a major challenge due to the radioactivity. Material selection for the storage of nuclear waste is a major issue

as it is directly related to national safety. Hence, before choosing any material for nuclear waste storage, an in-depth review of materials used for the same is necessary.

References:

1. www.cea.nic.in/sitemap.html accessed on 25/07/2013.

2. S. P. Sukhatme, Curr. Sci. 101 (2011) 624.

3. http://www.world-nuclear.org/info/Current-and-Future-Generation/Nuclear-Power-in-the-World-Today/#.Uf3lZpKBGDg accessed on 04/08/2013.

4. http://world-nuclear.org/NuclearDatabase/rdResults.aspx?id=27569 accessed on 04/08/2013.

5. http://www.barc.ernet.in/about/anu1.html.

6. P. Sengupta, C. P. Kaushik, G. K. Dey, M. Ramkumar (ed.), On a sustainable future of the earth's natural resources, Springer Earth System Sciences, DOI 10.1007/978-3-642-32917-3_2, Springer-Verlag Berlin Heidelberg (2013).

7. http://www.iea.org/publications/freepublications/publication/India_study_FINAL_WEB.pdf accessed on 24/11/2013.

8. K. R. Rao, Curr. Sci. 81 (2001) 1534.

9. I. Johnson, J. Nucl. Mater. 154 (1988) 169.

10. Baldev Raj, H. S. Kamath, R. Natarajan, P. R. V. Rao, Prog. Nucl. Energy 47 (2005) 369.

11. P. Hogselius, Energy Policy 37 (2009) 254.

12. Baldev Raj, U. Kamachi Mudali, Prog. Nucl. Energy 48 (2006) 283.

13. L. R. Bairi, Ph.D. thesis (2012), www.hbni.ac.in, HBNI, Mumbai.

14. A. Kakodkar, Nuclear Power in India: An inevitable option for sustainable development of a sixth humanity, World Nuclear Association Annual Symposium, London (2002).

15. P. K. Dey, N. K. Bansal, Nucl. Eng. Des. 236 (2006) 723.

16. P. K. Dey, "Spent fuel reprocessing: An overview" in Eds. Baldev Raj, P.R.V. Rao, Nuclear fuel cycle technologies-closing fuel cycle, BRNS, Mumbai (2006) 221-237.

17. W. B. Lanham, T. C. Runion, USAEC Report ORNL-479 (1949).

18. Purex Technical Manual, USAEC Report HW-31000 (1955).

19. M. McKibben, Radiochim. Acta 36 (1984) 3.

20. N. Padhy, Ph.D. thesis (2011), www.hbni.ac.in, HBNI, Mumbai.

21. A. Naylor, H. Eccles, Proc. ISEC-88, Moscow, Vol. 1 (1988) 31.

22. E. B. Sheldon, USAEC Report DP-1467 (1977).

23. K. Ebert, Nucl. Energy 27 (1988) 361.

24. W. Fournier, D. Hugelmann, E. Dalverny, Solvent Extraction 1990, T. Sekine (Ed.), Pt A, Elsevier Sci., Publ. B.V. (1992) 747.

25. B. Anderson, J. D. Frew, O. Pugh, P. J. Thompson, The Nucl. Engineer, 35 (1994) 129.

26. D. D. Sood, S.K. Patil, J. Radioanal. Nucl. Chem, 203 (1996) 547.

27. T. P. Lagus, Reprocessing of spent fuel-A Policy Analysis, Washington Interships for Students of Engineering, Aug. (2005).

28. A. Kakodkar, Conf. on Chem. Eng. Cong., Calcutta (2000), Paper Nos. CHE 6, CHE 14.

29. Baldev Raj, U. Kamachi Mudali, T. Jayakumar, K. V. Kasiviswanathan, R. Natarajan, Sadhana 25 (2000) 519.

30. U. Kamachi Mudali, R. K. Dayal, J. B. Gnanamoorthy, J. Nucl. Mater. 73 (1993) 203.

31. U. Kamachi Mudali, A. Ravishankar, S. Ningshen, S. Girija, R. Sole, K. Thyagarajan, Energy Procedia 7 (2011) 468.

32. IAEA Safety Standard Series, No-WS-R-2 (2000).

33. P.A. Baisden, G.R. Choppin, Nuclear waste management and the nuclear fuel cycle, in Radiochemistry and Nuclear Chemistry, [Ed. Sándor Nagy], in Encyclopedia of Life Support Systems (EOLSS), Eolss Publishers, Oxford, UK (2007).

34. http://www.barc.gov.in/publications/eb/golden/nfc/toc/Chapter%2013/13.pdf

35. K. Raj, K. K. Prasad, N. K. Bansal, Nucl. Eng. Design 236 (2006) 914.

36. IAEA, Technical Report Series No. 339, IAEA, Vienna (1992).

37. S. Girija, U. Kamachi Mudali, Baldev Raj, J. Appl. Electrochem. 41 (2011) 973.

CHAPTER **2**

Materials Challenges in the Storage of Nuclear High Level Waste

Material Challenges in the Storage of Nuclear High Level Waste

This Chapter reviews the literature data available on the experience of various countries towards nuclear waste treatment and selection of materials for the storage of different kind of wastes. A summary of the materials used at various waste storage sites all around the world is reported. This Chapter also gives a brief account of the failures encountered at different sites during HLW storage. The need for the identification of advanced materials for waste storage tank and the scope for the thesis work are highlighted in this Chapter.

2.1 Storage of HLW

If nuclear power is to be continued as a sustainable source of electricity, it is important that the resulting wastes are safely managed. Management of radioactive waste covers the entire range of activities starting from handling, treatment, conditioning, transport, storage and final disposal.

The major component of the high level liquid waste (HLLW) is the aqueous raffinate resulting from the PUREX cycle. These wastes are stored in tanks made up of various materials based on their chemical nature. The HLLW storage tanks have a volume varying from 50 to 500 m^3. They have provision for stirring, removal of radiolytic gases, control of liquid level, measurement of pH and radioactivity. The tanks are usually double-walled, have heavy concrete shielding and are often placed underground. Storage in tanks is only an interim procedure for waste management. However, the container of the HLLW has a key role since it prevents the escape of radioactive particles to the atmosphere. The short-term storage period is usually 30 to 50 years, but may also extend in certain cases. Although these containers will be used for storing the waste until further treatment like vitrification, their

service life depends on the strength, stability and corrosion resistance of the material of construction. The container materials will be exposed to significant radiation, elevated temperatures, oxidizing compounds etc. Additionally, the containers will have welds that have heterogeneous composition due to solute segregation and that may retain significant residual stress.

Corrosion of a metal is a complex process, involving several coupled reactions. As corrosion progresses, a thin layer of metallic compound formed on the metallic surface may limit the flow of metal ions to solution, thus slowing the corrosion rate. This property is called passivity and it must be exhibited by any proposed container material for storing HLW. The formation of passive film will slow down further corrosion. When the passive film is disrupted or suffers chemical breakdown, localized corrosion like pitting etc. occurs which assumes importance in the context of storing nuclear waste, as any small perforation may allow significant release of radioactivity. Localized corrosion may also occur as a result of stress present particularly at welds.

The storage container should be able to withstand a minimum period of 30 years if put into temporary storage within the power plant, where the premises are dry and the average temperature is not high. In this case, external corrosion factors are not relevant and the lifetime of the containers depends only on the aggressiveness of the radioactive waste and the corrosion resistance of the container material.

2.2 Criteria for the selection of container material

The selection criteria of a material for the storage of HLW should consider the performance of the material in terms of the following factors:

2.2.1 Chemical corrosion

The storage tanks should accommodate the HLW comprising corrosive media such as acid, water, acid vapor, oxidizing ions, hydrogen, oxygen, radiations etc.. Wet corrosion occurs when liquid is present, while dry corrosion occurs at high temperatures when vapor or gases are involved. Corrosive agents like chloride ions present at various degrees in water can penetrate the passive surfaces of the container material and cause pitting corrosion. Pitting is initiated when a small anodic site is created by breaking of the protective film and the surrounding passive surface acts as a cathode.

Additionally, pits are stress raisers; they increase the stress in the metal at the pitting initiation site. Crack propagates by the residual stresses from welding or cold work and the resistance to crack propagation will be reduced by corrosion simultaneously. This results in stress corrosion cracking (SCC).

Another form of corrosion which influences the performance of the container material is microbiologically induced corrosion. Microorganisms can produce a corrosive acid as a byproduct of their metabolic cycle and may either enhance the electron transfer involved in the electrochemical reactions [1] or may ionize the metal surface [2]. Microorganisms can attack most of the metals and in the case of steel, microorganisms have been observed particularly to attack weldments [3]. Compositional and microstructural variations between parts of the container, created by different fabrication routes can establish local galvanic cells in the adjacent regions (assuming the presence of an electrolyte). If filler wire based welding processes are used, compositional and microstructural inhomogeneities between the filler and the base metal can create a similar galvanic effect; the effect is more harmful if the material in the weld is anodic since the attack will then be concentrated over a small area.

Storage of liquid nuclear waste requires the metallic tanks to have excellent corrosion resistance to the acidic waste containing nitric acid. Corrosion of storage tank material becomes more severe due to the accumulation of oxidizing corrosion products in the stored fluid over a long storage period. This calls for materials which have a low rate of general corrosion.

2.2.1.1 Corrosion in nitric acid medium

In strong oxidizing nitric acid medium corrosion of a material occurs in the transpassive zone. If any species which reduces the transpassive potential is present in the solution, then it will affect the corrosion resistance of the material. Similarly, corrosion rate increases, if any species tends to increase the oxidising power of the medium. However, general corrosion rate is less in the case of materials forming stable passive film on the surface. Presence of inclusions (mainly sulphides of iron and manganese) in the matrix lead to severe pitting and intergranular corrosion. Hence, these issues must be taken into account at the time of manufacturing the storage tank material. Therefore, the storage material for use with nitric acid medium must have low level of inclusions, should be resistant to sensitization, intergranular corrosion and should have low general corrosion rate [4, 5].

Autocatalytic reduction of nitric acid

Nitric acid is a strong acid, completely soluble in water and is stable under ambient conditions. Apart from this, it is a powerful oxidizing agent even in very dilute solutions. The reduction mechanism of nitric acid is widely investigated due to the large industrial applications, especially with regard to the corrosion of stainless steel as well as the disposal of radioactive waste containing nitric acid from spent nuclear fuel reprocessing plant.

Reduction mechanism of nitric acid is dependent on the concentration of nitric acid, and the auto-catalytic activity of nitrous acid produced as a result of reduction [6-14]. Being a strong acid, nitric acid completely ionizes to hydrogen ions (H^+) and nitrate ions (NO_3^-) as shown below.

$$HNO_3 \longleftrightarrow H^+ + NO_3^- \tag{2.1}$$

The nitrate ion gets reduced to nitrous acid, which is the electroactive species.

$$NO_3^- + 3H^+ + 2e^- \longleftrightarrow (HNO_2)_{aq} + H_2O \tag{2.2}$$
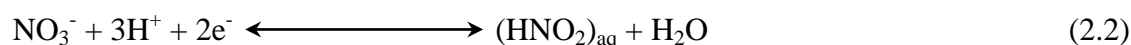
Nitrous acid is further reduced to nitric oxide (NO) and nitrogen dioxide (NO_2) depending upon the concentration of nitric acid. When the concentration of nitric acid is lower than 8M, the reduction product is NO and when the concentration is higher than 8M the reduction product is NO_2 [6, 10]. The schematic of autocatalytic reduction of nitric acid with variation of nitric acid concentration is represented in Fig. 2.1.
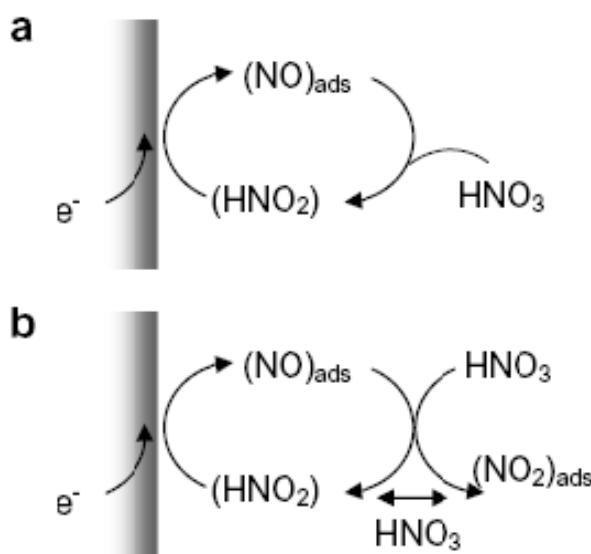
Fig. 2.1: Schematic of autocatalytic reduction of nitric acid (a) < 8 M (b) > 8 M concentration [10]

$$HNO_2 + H^+ + e^- + s \longleftrightarrow (NO)_{ads} + H_2O \tag{2.3}$$

$$HNO_3 + (NO)_{ads} \longleftrightarrow (HNO_2)_{el} + (NO_2)_{ads} \tag{2.4}$$

$$HNO_3 + (HNO_2)_{el} + 2s \longleftrightarrow 2(NO_2)_{ads} + H_2O$$

$$\tag{2.5}$$
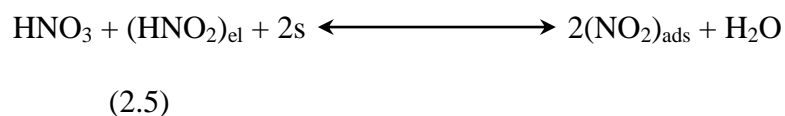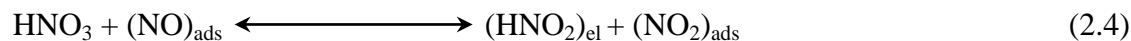
However, the overall reduction process depends upon the concentration of nitric acid.

2.2.2 Hydrogen embrittlement

The atomic hydrogen produced from a corrosion reaction may diffuse through the container material, along a stress gradient towards the stressed crack tip. Presence of hydrogen within the process zone at the crack tip decreases the ductility of the material [15]. Hydrogen absorbed during storage may cause embrittlement on the surface of the metal. Once the container material is exposed to high pressure or high temperature, carbon contained in the carbides in the material reacts with hydrogen, resulting in the decarburization of the steel and cavitations in the material. Thus, hydrogen embrittlement is an important concern because it is likely to cause a brittle fracture failure far more severe than any other corrosion. Since, susceptibility to hydrogen embrittlement increases with increasing material's strength, material with very high strength should not be selected for the storage of corrosive media.

2.2.3 Mechanical properties

As hydrogen embrittlement is a serious concern, alloys with very high mechanical strength are not favored for storage material. However, the ductility and fracture toughness need to be high for the candidate materials. The material must have very good thermal stability: this is an important feature of any alloy system in overlay welding and welding of thick sections,

where multiple passes will be required. Presence of detrimental inter-metallic phases during welding causes pitting and intergranular attacks. The material selected as container must be weldable and brittle microstructures must not occur in the heat-affected zone.

2.2.4 Effect of radiation

It has been reported that the processes and reactions resulting in the corrosion of materials are similar under irradiated and unirradiated conditions [16, 17]. Even though the processes and reactions are similar, the corrosion potential at crack tip might be much larger under irradiated conditions than under unirradiated conditions. This difference results from the penetration of gamma radiation through the stagnant solution within the crack. Irradiation may elevate corrosion potential by creating an oxidizing environment in the crack and assist the crack growth [15]. Radiation also generates hydrogen gas through radiolytic interaction with water. Considering these factors, the radiation effect on the storage material for high level waste must be assessed.

Based on the discussions, the materials to be selected for HLW storage must possess the following properties:

(1) Good mechanical strength and toughness

(2) Fabricability and cost effective

(3) Metallurgical phase stability even after welding, heat treatment, cold working etc.

(4) Resistance to

    (i)   Uniform corrosion and dissolution

    (ii)   Pitting

    (iii)   Crevice corrosion

(iv)   Stress corrosion cracking

(v)   Hydrogen embrittlement

(vi)   Radiation-enhanced corrosion and

(vii)   Microbiologically induced corrosion

2.3 Materials in use for HLW storage

Different structural materials have been used for the fabrication of HLW storage tanks depending on the HLW medium at various waste storage sites. Materials being used for the waste storage tanks are

(i)   Carbon steel

(ii)   304L stainless steel (SS)

(iii)   316L SS

(iv)   347 SS

Laboratory tests and in-service observations have revealed that carbon steel is susceptible to localized attack in dilute, uninhibited waste solutions. Tests performed with coupons in simulated waste solutions indicated that the coupon material is susceptible to pitting in the wetted film region above the water line [18]. The attack resulted from the depletion of hydroxide inhibitor which occurred due to the absorption of CO_2 into the wetted film and was induced by nitrate. It has also been reported by many authors that carbon steel undergoes nitrate induced stress corrosion cracking under waste storage condition [19-22].

Though no failure incident has been reported in the literature so far, with stainless steel in waste storage condition, it may not be the ideal material for long term storage. It has been predicted that use of conventional stainless steels for the fabrication of storage tanks for

HLW is not favorable under highly oxidizing conditions as these may undergo intergranular corrosion even in non-sensitized condition [23, 24]. Also, they are susceptible to sensitization in the welded zones, which involves chromium depletion at grain boundaries. In addition, these alloys suffer from pitting corrosion and transgranular stress corrosion cracking (TGSCC) in chloride containing solutions [25]. These issues necessitate the introduction of advanced materials and the present thesis projects nickel base superalloys to serve as candidate materials for the high level waste storage application.

2.4 Failure reports

A nuclear accident has both direct as well as indirect negative effect on public. Direct effect is the damage from the released radioactive materials. There is no spatial limit to the diffusion of radioactive materials in the air and the half-life of radioactive isotopes is generally long. Therefore, every being on earth is affected by radioactive contamination [26]. A few incidents describing the radioactive nuclear high level waste leakage at various waste storage sites across the globe are as follows:

2.4.1 Leakage at Hanford waste storage site

It has been reported that 67 of the 149 single shelled tank (SST) containing highly radioactive liquid waste at the Hanford waste storage site have leaked waste to the surrounding soil [27-29]. Leaks began to appear in the single-shell tanks shortly after the introduction of untreated nitrate-based wastes in the 1950s [30]. The first leakage (approximately 55,000 gallon from SST 241-U-104) was reported in 1956. The most significant leak (approximately 115,000 gallon (435,322 L)) was recorded in 1973. When

the leakages were discovered, the remaining liquid waste from the leaking tank was transferred to another tank. Despite this effort, it had been estimated that as much as one million gallon of waste (including cooling water) would have leaked from the SST.

Pitting and nitrate induced stress corrosion cracking had been identified as the primary modes of corrosion for the majority of the materials used in the radioactive waste tanks [31, 33].

In August 2012, it was reported that a double walled tank (AT-102) containing nearly 850,000 gallon of sludge has started leaking [34]. Recently in February, 2013, federal authorities of United States of America disclosed that one of the single shell tanks containing high level waste is leaking at a rate of 150-300 gallon per year at the Hanford site [35].

2.4.2 Leakage at Savanna River Site

The Savanna River Site has various types of high level waste tanks with secondary containment that are currently in service. Carbon steels like ASTM A285, ATTM A212 etc. were used for the construction of the tanks during the 1950's and 1960's. These tanks contain alkaline waste. Of the 16 tanks, 11 have leaked waste into the annular space. The cracks found in the waste tanks were reported to be initiated by nitrate induced stress corrosion cracking caused by the residual stresses around the weld during fabrication [36-40].

A detailed inspection and failure analysis of one of the failed storage tanks (Tank 16) at Savanna River Site identified more than 300 through-wall cracks [41-43]. Nitrate-induced SCC was attributed to be the most likely mode of failure for the Hanford SST. Later,

laboratory work focused on the effects of pitting and general corrosion. In the order of significance, research has indicated that SCC, pitting, crevice corrosion and uniform corrosion to be the major modes of degradation for the SST [28, 31].

2.4.3 Explosion at Production Association "Mayak"

A radiation accident occurred at the production association "Mayak", Chelyabinsk-40, Russia in September, 1957, which was made to public later. A tank containing 80 ton of highly-radioactive liquid waste exploded at the Mayak plutonium plant in the Southern Urals, 15 km east of the Russian city of Kyshtym. This waste consisted of solution of salts primarily of, sodium nitrate and acetate. Besides the enumerated salts, the storage tank contained radioactive elements. The accident was caused by a chemical explosion of a tank storing radioactive waste generated from the production of weapons-grade plutonium. The exploded tank had a cylindrical shape with a plane bottom without a cover. The tank made of stainless steel was placed in a separate canyon of reinforced concrete. The top of the canyon was closed with a cylindrical plate of reinforced concrete. Failure of the cooling system of the tank resulted in the rise in the temperature of the tank's content and eventually the water content evaporated from the solution [44-47].

In addition to the routine releases of nuclear waste into the Techa river there were accidental releases. These wild releases occurred when radioactive products from the HLW storage tanks leaked into drainage or cooling water as a result of the deterioration of cooling or transport pipes. The radiation safety service of the Mayak Production Association detected such accidental releases on September 27-29, on October 9, 26, and 31, on November 2, and on December 12, 1951 [48].

2.4.4 Radioactivity release at Asse storage facility

Electricity is being produced from nuclear fission in Germany for more than 60 years; but there is no final repository for the resulting waste. Since the 1960s, much of the waste has ended up at the Asse storage facility, a salt mine which was expected to protect the radioactive garbage for the next 100,000 years. However, just 40 years later, massive problems were observed. It was observed that 12,000 liter of water leaked out into the site each day and rusting the drums resulted in the release of radioactivity. Neverthless, there is neither a proposal for the management of the resulting sludge nor a plan in place for solving the Asse problem in Germany. Many of the waste drums were simply piled up, instead of neatly stacked. It is impossible to get close enough to begin a cleaning program [49].

These failure reports indicate that the container material for HLW storage is a vital issue, which necessisates the introduction of new and advanced materials after characterizing them for their corrosion behaviour and phase stability.

2.5 Advanced nickel base alloys

Nickel, either in elemental form or alloyed with other metals and materials has made significant contributions to the present-day society. It is a versatile element and can form alloys with most of the metals. Nickel-copper base Alloy 400 (Monel 400, UNS N04400) was developed as the first nickel-base alloy at the beginning of the twentieth century [50]. This alloy was developed as an alternative chloride-corrosion resistant material to austenitic stainless steel.

Many nickel-base alloys have been developed and applied as corrosion-resistant alloys in various environments, as well as creep-resistant alloys in high-temperature applications.

Owing to their versatility, complex processes and waste streams can be handled safely [51]. The wide variety of applications for Ni and Ni base alloys include components used in the chemical and petrochemical industries, pollution control equipment, coal gasification and liquefaction systems, parts used in pulp and paper mills, aircraft gas turbines, steam turbine power plants, turbochargers and valves in reciprocating engines, electrical and electronic applications, and heat-treating equipment. A number of other applications for nickel alloys involve the unique physical properties of special-purpose alloys such as controlled-expansion alloys, electrical-resistance alloys, soft-magnetic alloys and shape-memory alloys. In the nuclear power industry, nickel-base alloys have been used in pressurized water reactors (PWRs) and boiling water reactors (BWRs) since their initial development from the early 1950's [52].

2.5.1 Effects of alloying elements in nickel base alloys

Nickel provides metallurgical stability, improved thermal stability and weldability. It also improves resistance to reducing acids and caustics, and increases resistance to stress corrosion cracking particularly in chlorides and caustics.

Chromium benefits nickel by promoting and preserving passivity. It enhances the passive surface film formation in the presence of oxidizers. Cr additions to Ni impart improved resistance to oxidizing media such as nitric acid (HNO_3) and chromic acid (H_2CrO_4). Chromium also improves resistance to high-temperature oxidation and to attack by hot sulphur-bearing bases. Although alloys have been formulated with Chromium content up to 50 %, alloying additions are usually in the range 15-30 %.

Copper additions provide improvement in the resistance of nickel to reducing acids. In particular, alloys containing 30 to 40% Cu offer enhanced resistance to nonaerated sulphuric acid (H_2SO_4) and excellent resistance to all concentrations of nonaerated hydrofluoric acid (HF). Additions of 2 to 3% Cu to nickel-chromium-molybdenum-iron alloys have also been found to improve the resistance to hydrochloric acid (HCl), H_2SO_4 and phosphoric acid (H_3PO_4).

Iron is used in nickel base alloys to reduce costs and not to promote corrosion resistance. However, iron does provide nickel with improved resistance to H_2SO_4 at concentrations above 50 %. Iron also increases the solubility of carbon in nickel, which in turn improves resistance to high-temperature carburizing environments.

Molybdenum in nickel substantially improves the resistance to non oxidizing acids. Commercial alloys containing up to 28 % Mo (Hastelloy B series) have been developed for service in non oxidizing solutions of HCl, H_3PO_4 and HF, as well as in H_2SO_4 with concentrations below 60 %. Mo also improves the pitting and crevice corrosion resistance of nickel base alloys. In addition, it is an important alloying element for imparting strength to metallic materials designed for high-temperature service.

Silicon is added only in minor amounts in most of the nickel base alloys to promote high-temperature oxidation resistance. In alloys containing significant amounts of iron, cobalt, molybdenum, tungsten or other refractory elements, the level of silicon must be carefully controlled because it can stabilize carbides and harmful intermetallic phases. On the other hand, the use of silicon as a major alloying element has been found to greatly improve the resistance of nickel to hot, concentrated H_2SO_4. Alloys containing 9 to 11 % Si are produced for such service in the form of castings.

Cobalt, like iron, increases the solubility of carbon in nickel-base alloys and increases resistance to carburization. Further, the melting point of cobalt sulfide is higher than that of nickel sulfide; therefore, alloying with cobalt also tends to improve high-temperature sulfidation resistance.

Niobium is added as stabilizing element to tie up with carbon and prevent intergranular corrosion attack due to grain-boundary carbide precipitation in corrosion resistant alloys. It also improves resistance to pitting and crevice corrosion and increases high temperature strength.

Carbon added to nickel forms carbide of the formula Ni_3C at elevated temperatures, but it is unstable and decomposes into a mixture of nickel and graphite at low temperatures. Because this phase mixture tends to have low ductility, low-carbon forms of nickel are usually preferred for corrosion resistant applications.

Nitrogen enhances metallurgical stability, improves pitting and crevice corrosion resistance, and increases strength.

Sulphur addition lowers the melting point of nickel. The solubility of sulphur in solid nickel is about 0.005% [53]. Amount of sulphur in excess of the solid solubility may form grain boundary deposits of nickel sulphides or low melting eutectic of nickel-nickel sulphide and thus, lower the strength and malleability of the material. In most of the commercial nickel base alloys, sulphur content is normally kept below to about 0.010 %.

Tungsten improves resistance to reducing acids and to localized corrosion and enhances both strength and weldability. Additions of tungsten of the order of 3 to 4% in combination with 13 to 16% Mo in a nickel-chromium base results in alloys with outstanding resistance to localized corrosion.

Aluminium is often used in minor amounts for the purpose of deoxidation or to tie up carbon and/or nitrogen, respectively. It improves resistance to oxidation at elevated temperatures and promotes age hardening.

Titanium combines with carbon to reduce the susceptibility to intergranular corosion due to chromium carbide precipitation resulting from heat treatments. When added together with aluminium, they facilitate the formulation of age-hardenable high-strength alloys for serving at low and elevated temperatures [54, 55].

2.5.2 Mechanical properties

Pure nickel is ductile and tough and it possesses a face-centered cubic (fcc) structure up to its melting point (1453 ^{0}C). Though Ni- base alloys in general contain a large proportion (sometimes up to 50%) of other alloying elements, nickel alloys still maintain the fcc (γ) structure from the nickel base element. Therefore, nickel and nickel alloys are readily fabricated by conventional methods and they offer freedom from the ductile-to-brittle transition behaviour of other metals and alloys, including steels. As a consequence of the fcc structure, nickel base alloys have excellent ductility, malleability and formability. Nickel alloys are also readily weldable.

2.5.3 Corrosion properties of nickel base alloys

In the electrochemical series, nickel is nobler than iron. It exhibits better corrosion resistance than iron in reducing environments due to the formation of protective corrosion films with superior passivation characteristics compared to iron. Nickel has superior corrosion resistance in caustic or non oxidizing acidic solutions and in gaseous halogens. It can be

easily alloyed with various elements like chromium, molybdenum, iron and copper. Alloying with chromium provides very good corrosion resistance in both reducing and oxidizing environments. These alloys have a higher tolerance for alloying elements in solid solution than stainless steels and other iron base alloys but maintain good metallurgical stability, which make them to out-perform the most advanced stainless steels [56]. Nickel has good resistance to corrosion in the normal atmosphere, in freshwaters and in deaerated non oxidizing acids, and it has excellent resistance to corrosion by caustic alkalis. Alloys with high nickel content have good stress corrosion cracking resistance in chloride solution. Nickel alloys, just like other alloys, may suffer two main types of corrosion, uniform corrosion and localized corrosion. Uniform corrosion occurs under reducing conditions in the active region of potentials and also under oxidizing conditions in the form of a slow passive corrosion. Localized corrosion such as pitting and crevice corrosion generally occurs under oxidizing conditions. Stress corrosion cracking or environmentally induced cracking could occur at any electrochemical potential range [56].

2.5.4 Application of nickel base alloys in nuclear industries

Commercial nickel base Alloys 600, 690, 800, X-750 and 718 have been used as materials for the fabrication of components and parts of nuclear power plants. Various nickel base alloys employed in various nuclear reactors are reported in Table 2.1.

Table 2.1 Candidates of nickel base alloys for nuclear reactors [52].

Type of Nuclear Reactor	Nickel base Alloys
BWR	600, X-750, 718, 625
PWR	X-750, 718, 690, 800, A286
CANDU	600, X-750, 718, 690, 800
LMFBR	X-750, 718, 800
HTGR	600, X-750, 718, 625, XR

2.5.5 Categories of nickel alloys

Based on the applications nickel base alloys are categorized as (a) alloys primarily used for corrosion resistance and (b) alloys used for high-temperature strength (referred as superalloys). However, this distinction is not sharp, because some of the superalloys are used in corrosion service and some of the corrosion-resistant alloys are used in high-temperature service. Many of the alloys that have high-temperature strength are multiphase alloys with precipitation-strengthening elements such as aluminum, titanium and niobium. They also have higher carbon levels. Most of the corrosion-resistant alloys are single-phase alloys that can be strengthened mainly by cold working.

Nickel and nickel alloys, like stainless steels, offer high corrosion resistance in wide range of corrosion environment. Neverthless, nickel can accommodate larger amount of alloying elements; mainly chromium, molybdenum and tungsten, in solid solution than iron [57]. Therefore, nickel base alloys in general, can be used in more severe environments than stainless steels.

Nickel base materials developed commercially for corrosion resistance fall into the following general classifications [58]:

1. Commercially pure nickel material

2. Nickel-copper alloys

3. Nickel-chromium alloys

4. Nickel-iron alloys

5. Nickel-molybdenum alloys

6. Nickel-chromium-molybdenum alloys

7. Nickel-chromium-molybdenum-copper alloys

8. Complex nickel base alloys, which may contain as many as six or more significant metallic elements (generally used as corrosion resistant material with good strength at high temperature).

Figure 2.2 shows a pictorial presentation of various kinds of nickel base alloys according to their major elemental compositions. However, new alloys and refinement of old alloys are being developed continuously. As the work reported in the present thesis is related to Nickel-Chromium alloys, further discussion is limited to Nickel-Chromium alloys only.

The nickel-chromium alloys can be thought of as nickel base analogs of the iron base austenitic stainless steel alloys, with an interchange of the iron and nickel contents. In these alloys, the chromium content in general ranges from 15 to 30 %, and iron ranges from 3 to 20 % [60]. These alloys form a stable Cr_2O_3 surface film, and offer excellent corrosion resistance in many severe environments and showing immunity to chloride-ion stress-corrosion cracking.
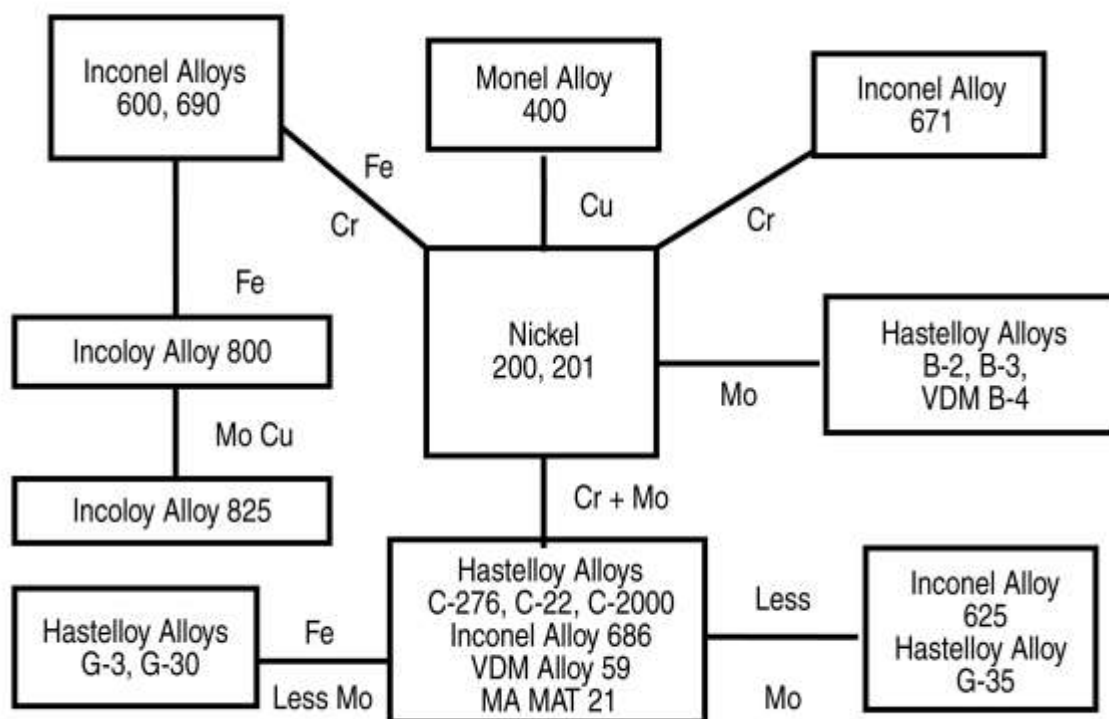
Fig. 2.2: Nickel tree [59]

Addition of chromium to nickel in amounts greater than about 10 % has a marked effect upon its electrochemical and corrosion behaviour. It causes a reduction in the critical current density required to initiate passivity, widens the passive range and reduces passivation current density.

2.5.6 Corrosion behaviour of Ni-Cr alloys in specific environments

2.5.6.1 Atmospheric corrosion

Nickel base alloys have very good resistance to atmospheric corrosion. Corrosion rates are typically < 0.0025 mm/year (0.1 mpy), with varying degrees of surface discoloration depending on the composition of the alloy [57]. Nickel-chromium alloys have very good atmospheric corrosion resistance and they remain bright indefinitely. However, they may

develop a slight tarnish after prolonged exposure, especially in sulphurous industrial atmosphere. In marine atmosphere, these alloys can develop numerous shallow pits.

2.5.6.2 Corrosion in water

Nickel-chromium alloys have high degree of resistance to fresh water, distilled water, as well as towards the most corrosive natural waters containing free carbon dioxide, chlorides and dissolved oxygen. However, because of the cost of nickel alloys, less expensive stainless steels or other materials are usually considered for pure or freshwater applications unless increased resistance to stress corrosion cracking or pitting is required. For example, Alloys 600 and 690 are used for increased stress corrosion cracking resistance in nuclear steam generators using high-purity water. The nickel-chromium alloys have good corrosion resistance in high velocity sea water. However, these alloys may undergo pitting and crevice attack when immersed in quite or low velocity water, under marine organisms, or other solids which accumulate on the alloy surfaces [61, 62].

The nickel-chromium base Alloy 600 was reported to be susceptible to stress corrosion cracking as well as intergranular corrosion in deaerated as well as aerated water at high temperatures and the corrosion resistance decreased with increase in temperature [63, 64]. However, Alloy 690, the advanced version of Alloy 600, contains lower amount of nickel with higher amount of chromium and possesses better stress corrosion cracking resistance in pure water than Alloy 600 [65-69]. McIlree et al. [70] observed that elements like carbon, sulphur or phosphorus have no effect on the intergranular resistance of Alloy 600 in deaerated water.

2.5.6.3 Corrosion by sulphuric acid

Nickel-chromium alloys have good resistance to unaerated sulphuric acid solutions up to about 60 % concentration at room temperature and the corrosion rate is normally less than 5 mils per year. However, their corrosion rate increases considerably with increase in temperature [58]. Singh et al. [71] studied the corrosion resistance of Ni-Cr alloys in sulphuric acid medium and reported a decrease in corrosion resistance of the alloys with increase in sulphuric acid concentration.

Myers et al. [72] investigated the anodic polarization behaviour of annealed high-purity nickel, chromium and a series of binary nickel chromium alloys in hydrogen saturated sulphuric acid solutions at 25 ^{0}C, using potentiostatic techniques. All the nickel-chromium alloys exhibited an active-passive transition in the sulphuric acid solutions. The addition of 9 % or more chromium to nickel significantly reduced the critical current densities. Increasing the chromium concentration expanded the passive region. Similar observations were reported by Bond et al. [73] in nitrogen saturated solutions. In both the cases the critical current density decreased to a much lower rate after a concentration of 14 % chromium.

Nickel-chromium alloys are seldom used with hot sulphuric acid solutions except in low acid concentrations or in cases where the presence of other chemicals in the solution having a passivating effect. However, the addition of oxidizing salts like ferric or cupric sulphate to sulphuric acid solution will have an inhibiting effect on the corrosion of these alloys at moderate temperatures.

Nickel-chromium base Alloy 600 was found to be susceptible to SCC and intergranular attack (IGA) in sulphuric acid due to the segregation of sulphur towards grain boundary,

which also increases the critical current density as well as passivation current density and decreases the passive range [69, 74].

2.5.6.4 Corrosion by phosphoric acid

Nickel-chromium alloys are resistant to corrosion by phosphoric acid solutions for all concentrations at ambient temperature, with corrosion rate < 2 mpy. The corrosion rate increases rapidly with increase in temperature. These alloys are not suitable for use with boiling phosphoric acid solutions. Vishnudevan et al. [75] have studied the corrosion behaviour of Alloy 600 and Alloy 601 in various concentrations of phosphoric acid and reported the increase in corrosion rate with increase in concentration of phosphoric acid and a shift of corrosion potential towards active direction.

2.5.6.5 Corrosion by hydrochloric acid

Nickel-chromium alloys have moderately good corrosion resistance to dilute non-aerated hydrochloric acid solutions at atmospheric conditions, but their corrosion rates increase considerably by increasing the acid concentration and temperature and by aeration of the acid. The corrosion resistance also increases with increase in nickel content of the alloys. Addition of oxidizing salts to hydrochloric acid solution greatly increases the corrosion of nickel-chromium alloys and often results in severe pitting attack.

2.5.6.6 Corrosion by nitric acid

Nickel-chromium alloys have better corrosion resistance in nitric acid solutions than any other nickel base alloys. With increase in the chromium content in these alloys, the corrosion

rate decreases. The nickel-chromium alloys are resistant to red and white fuming nitric acids at room temperature, but only the alloys containing 30 to 40 % chromium have useful resistance at elevated temperatures.

Alloy 600 is resistant to nitric acid solutions above about 20 % nitric acid at ambient temperature [70]. Its chromium content is not high enough to provide passivation at higher temperatures. However, nickel-chromium alloys containing 20 % or more chromium are resistant to all concentrations of nitric acid at room temperature and are considerably more resistant to hot solutions than Alloy 600.

Nickel-chromium alloys containing chromium below 25 % and carbon more than 0.02 % are susceptible to intergranular corrosion in hot nitric acid solutions. The attack decreases with increase in chromium concentration and is particularly eliminated when the chromium concentration is more than 35 % [76].

2.5.6.7 Corrosion by alkalis

Alloy 600 has good corrosion resistance towards alkalis, except in concentrated hot caustic solutions [77]. In certain applications involving high-temperature caustics, where sulfur is present or high strength is required, Alloy 600 is used. The chromium content of Alloy 600 provides good resistance to sulfur embrittlement. Yasuda et al. [78] evaluated the corrosion behaviour of Alloy 600 in NaOH solutions in the concentration range 30-60 % at various temperatures and reported severe corrosion of the specimens in solutions saturated with oxygen under high pressure. On the other hand, the alloys were resistant to corrosion when the solutions were saturated with hydrogen. The specimens exposed to boiling NaOH

solution were corroded. They have also reported that the corrosion rate was dependent on the Ni content in the alloys; higher the Ni content, lower is the corrosion rate.

Though Alloy 690 possesses superior SCC resistance in many environments compared to Alloy 600, this alloy has been reported to be susceptible to SCC and IGA in deaerated caustic environments [70, 79]. Thermal treatment of Alloy 690 at around 700 ^{0}C that brings about semi continuous grain boundary Cr-carbide precipitates along with intragranular Cr-carbides, was observed to improve the caustic corrosion resistance of the alloy [79].

2.6 Need for the present study

Survey of literature revealed that materials like carbon steel and various stainless steels are widely used in nuclear industries for the storage of high level liquid waste. However, both the materials undergo uniform as well as localized corrosion. Carbon steel suffers from pitting as well as nitrate induced stress corrosion cracking and leakages have already been observed at many waste storage sites. Similarly, stainless steels are susceptible to sensitization in the heat affected zones at the time of welding, which involves chromium depletion at grain boundaries. Additionally, these alloys suffer from pitting corrosion and transgranular stress corrosion cracking in chloride containing solutions. Corrosion is a major issue concerning environmental safety. This necessitates the search for new materials which can minimize the corrosion issues. Literature survey indicated that austenitic nickel base alloys provide a good alternative to austenitic stainless steels because of their improved corrosion resistance, thermal conductivity and mechanical properties. Hence, an attempt has been made in the present thesis work to investigate the corrosion behaviour of various nickel base alloys for application as a nuclear high level waste storage tank material. Since the

actual waste solutions are highly radioactive, testing these alloys in actual wastes can be accomplished only in a hot cells and hence not attempted in the present work. The cost factor and the difficulties involved in handling hot waste solutions, in addition to the changing chemical state of the oxidizing fission product ions in the tank over longer years of tank operation, warranted the use of non-radioactive simulated waste solution only for this study.

References:

[1]   W. P. Iverson, Adv. Appl. Microbio. 32 (1987) 5.

[2]   J. D. A. Miller Metals. In: A. H. Rose (Ed.) Economic Microbiology, Academic Press, New Work.

[3]   S. C. Dexter (Ed.) Biologically induced corrosion, Proc. Int. Conf. on Biologically Induced Corrosion, Houston, 1986

[4]   U. Kamachi Mudali, R. K. Dayal, J. B. Gnanamurthy, J. Nucl. Mater., 203 (1993) 73.

[5]   S. Girija, V.R. Raju, U. Kamachi Mudali, R.K. Dayal, Corros. Eng. Sci. Tech. 38 (2003) 309.

[6]   F. Balbaud, G. Sanchez, P. Fauvet, G. Santarini, G. Picard, Corros. Sci. 42 (2000) 1685.

[7]   F. Balbaud, G. Sanchez, G. Santarini, G. Picard, Eur. J. Inorg. Chem. 2 (1999) 277.

[8]   U. R. Evans, The corrosion and oxidation of metals, Edward Arnold, London, 1960.

[9]   F. Balbaud, G. Sanchez, G. Santarini, G. Picard, Eur. J. Inorg. Chem. 4 (2000) 665.

[10] P. Fauvet, F. Balbaud, R. Robin, Q.-T. Tran, A. Mugnier, D. Espinoux, J. Nucl. Mater. 375 (2008) 52.

[11] D. G. Kolman, D. K. Ford, D. P. Butt, T. O. Nelson, Corros. Sci. 39 (1997) 2067.

[12] S. Ningshen, U. Kamachi Mudali, S. Ramya, Baldev Raj, Corros. Sci. 53 (2011) 64.

[13] V. P. Razygraev, R. S. Balovneva, E. Y. Panomareva, M. V. Lebedeva, Prot. Met. 26 (1990) 43.

[14] O. W. J. S. Rutten, A. V. Sandwijk, G. V. Weert, J. Appl. Electrochem. 29 (1999) 87.

[15] F. H. Huang, J. Nucl. Mater. 231 (1996) 74.

[16] W. L. Clarke, A. J. Jacobs, Proc. 2nd Int. Symp. On Env. Degradation of Materials in Nuclear Power Systems – Water reactors, Myrtle Beach, 1983, p. 451 – 461.

[17] W. L. Clarke, D. A. Hale, M. Siegler, Proc. 3rd Int. Symp. on Env. Degradation of Materials in Nuclear Power Systems–Water Reactors, Monterey, 1985, p. 442-447.

[18] S. B. Oblath, J. W. Congdon, "Inhibiting localized corrosion during storage of dilute wastes, Waste Management 87, (Tuscon, AZ: 1987).

[19] B. J. Wiersma, Constant extension rate testing of type 304L stainless steel in simulated waste tank environments (U), Report No: WSRC-MS-91-51.

[20] A study of corrosion and stress corrosion cracking of carbon steel nuclear waste storage tanks, RPP-34657-FP, September, 2007.

[21] R. N. Parkins, R. Usher, "The effect of nitrate solutions in producing stress corrosion cracking in mild steel", Proceedings First International Congress on Metallic Corrosion. London, U.K.: Butterworths (1962): 296-302.

[22] C. S. Scott, F. Gui, C. S. Brossia, J. A. Beavers, G. S. Frankel, G. L. Edgemon, et al., A study of stress corrosion cracking and localized corrosion of carbon steel in nitrate base nuclear waste, Corrosion 2009, Paper No: 09434.

[23] H. Chauve, J. Detours, R. Demay, M. Pelras, J. Simmonnet, Nucl. Europe 2 (1986) 19.

[24] U. Kamachi Mudali, R. K. Dayal, J. B. Gnanamoorthy, J. Nucl. Mater. 203 (1993) 73.

[25]   L. Vehovar, M. Tandler, Nucl. Eng. Des. 206 (2001) 21.

[26]   D. Fang, C. Z. Sun, L. Yang, Nuclear Safety, 36 (1995) 135.

[27] M. J. Rodgers, "Waste Tank Summary Report for Month Ending December 31, 2006" CH2M HILL Hanford Group, Inc. Report, HNF-EP-0182, Rev. 225, Sept 6, 2007.

[28] G. L. Edgemon, V. S. Anda, H. S. Berman, M. E. Johnson, K. D. Boomer, Corrosion, 65 (2009) 163.

[29] H. Babad, R. J. Cash, J. L. Deichman, G. D. Johnson, J. Hazard. Mater. 35 (1993) 427.

[30] P. C. Ohl, J. D. Thomson, F. R. Vollert, in: CORROSION/94, paper no. 142 (National Association of Corrosion Engineers, Houston, TX, 1994).

[31] D. C. Lini, Compilation of Hanford Corrosion Studies, Atlantic Richfield Hanford Company Report, ARH-ST-111, UC-70 (1975).

[32] G. L. Edgemon, R. P. Anantatmula, Hanford Waste Tank System Degradation Mechanisms Report, Westinghouse Hanford Company Report, WHC-SD-WM-ER-414, Rev. 1, October, 1996.

[33] Characterization of the Corrosion Behavior of the Carbon Steel Liner in Hanford Site Single-Shell Tanks, R. P. Anantatmula, E. B. Schwenk, M. J. Danielson, WHC-EP-0772, June 1994.

[34]   http://www.examiner.com/article/the-hanford-nuclear-facility-has-sprung-another-leak-of-radioactive-waste accessed on 05/08/2013.

[35]   http://www.democraticunderground.com/10022383926 accessed on 05/08/2013.

[36] K. H. Subramanian, Review of Type I High Level Waste Tanks Ultrasonic Inspection Data, WSRC-TR-2003-00560, March, 2006.

[37] B. J. Wiersma, An Assessment of the Service History and Corrosion Susceptibility of Type IV Waste Tanks, SRNS-STI-2008-00096, Sept 2008.

[38] B. J. Wiersma, R. L. Sindelar, "SRS High Level Waste Tank and Piping Systems – Structural Integrity Program and Topical Report," WSRC-TR-95-0076, June 1995.

[39] E. N. Hoffman, K. H. Subramanian, Probability Base Corrosion Control for High Level Waste Tanks: Interim Report, WSRC-STI-2007-00712, February, 2008.

[40] P. E. Zapp, J. W. V. Zee, Electrochemical Studies of Nitrate-Induced Pitting in Carbon Steel, WSRC-MS-98-00865.

[41] F. G. McNatt, "Annual Radioactive Waste Tank Inspection Program-1992(U)," Westinghouse Savannah River Company Report, WSRC-TR-93-166,December 31, 1992.

[42] W. L. Poe, "Leakage from Waste Tank 16—Amount, Fate, and Impact," Du Pont de Nemours (E.I.) and Company Report, DP-1358, November, 1974.

[43] T. L. Davis, D. W. Tharin, D. W. Jones, D. R. Lohr, "History of Waste Tank 16-1959 through 1974," Du Pont de Nemours (E.I.) and Company Report, DPSPU-77-11-17, July 1, 1977.

[44] O. A. Pavlovskiy, Radiological consequence of the kyshtym accident, in I. Khripunov et al. (Eds.) Social and Psychological Effects of Radiological Terrorism, IOS Press, 2007.

[45] http://www.spiegel.de/international/world/atomic-deserts-a-survey-of-the-world-s-radioactive-no-go-zones-a-756369-20.html.

[46] M. I. Avramenko, A. N. Averin, E. G. Drozhko, Y. V. Glagolenko, V. P. Filin, B. G. Loboiko, Y. G. Mokrov, G. N. Romanov, Atmos. Env. 34 (2000) 1215.

[47] Retracing Mayak's Radioactive cloud, Science, 283, Issue 5399, 8th Jan (1999) 164.

[48] Y. G. Mokrov, Radiat. Environ. Biophys. 42 (2003) 7-15.

[49] http://www.spiegel.de/international/world/atomic-deserts-a-survey-of-the-world-s-radioactive-no-go-zones-a-756369-5.html.

[50] A. Monell, U.S. Patent 811,239, Jan 1906.

[51] R. B. Rebak, P. Crook, Adv. Mater. Processes, 157(2), 2000, p 37-42.

[52] T. Yonezawa, Comprehensive Nuclear Materials, 2 (2012) 234.

[53] P. D. Merica, R. G. Waltenberg, Natl. Bur. Stand. Tech. Papers, 19 (1925) 155.

[54] http://www.keytometals.com/Article18.htm accessed on 7th August, 2013.

[55] http://www.parrinst.com/wp-content/uploads/downloads/2011/07/Parr_Inconel-Incoloy-Monel-Nickel-Corrosion-Info.pdf accessed on 25th Aug, 2013.

[56] Environmentally assisted cracking of nickel alloys - A review, R. B. Rebak, UCRL-PROC-205678, August, 2004.

[57] R. Davis (Ed), ASM Specialty Handbook, Nickel, Cobalt and their alloys (2000) p. 127-140.

[58] W. Z. Friend, Corrosion of nickel and nickel base alloys, John Wiley & Sons, New York (1980).

[59] F. G. Hodge, JOM, 9 (2006) 28-31.

[60] http://www.keytometals.com/Article101.htm accessed on 26/08/2013.

[61] R. B. Niederberger, R. J. Ferrara, F. A. Plummer, Mater. Prot. Perform., 9 (1970) 18.

[62] J. B. Maylor, Anti Corros. Methods Mater. 25 (1978) 3.

[63] H. Coriou, L. Grall, C. Mahieu, M. Pelas, Corrosion, 22 (1966) 280.

[64] H. Hirano, H. Takaku, T.Kurosawa, Corros. Sci., 31 (1990) 557.

[65] P. Berge, J. R. Donati Nucl. Tech., 55 (1981) 88.

[66] G. P. Airey, A. R. Vaia, R. G. Aspden, Nucl. Tech., 55 (1981) 436.

[67] J. J. Kai, M. N. Liu, Scr. Metall., 23 (1989) 17.

[68] J. R. Crum, Corrosion, 42 (1986) 368.

[69] R. A. Page, A. McMinn, Metall. Trans. A, 17A (1986) 877.

[70] A. R. McIlree, H. T. Michels, P. E. Morris, Corrosion, 31 (1975) 441.

[71] I. B. Singh, G. Venaktachari, Bulletin of Electrochem. 12 (1996) 83.

[72] J. R. Myers, F. H. Beck, M. G. Fontana, Corrosion, 21 (1965) 277.

[73] A. P. Bond, H. H. Uligh, J. Electrochem. Soc. 107 (1960) 488.

[74] I. J. Yang, Mater. Chem. Phy. 36 (1993) 42.

[75] M. Vishnudevan, G. Venkatachari, S. Muralidharan, N.S. Rengaswamy, Anticorros. Methods Mater. 45 (1998) 248.

[76] G. N. Flint, W. Barker, Proc. Chem. Eng. Group, Soc. Chem. Ind., 43 FB 1 (1966).

[77] R. W. Revie, H. H. Uhlig, Corrosion and Corrosion Control, 4th Edition (2008).

[78] M. Yasuda, K. Fukumoto, Y. Ogata, F. Hine, J. Electrochem. Soc., 135 (1988) 2982.

[79] R. S. Dutta, R. Tewari, P. K. De, Corros. Sci., 49 (2007) 303.

CHAPTER **3**

Experimental Details

Experimental Details

This Chapter describes the experimental methods employed in the thesis. It comprises the selection of materials and various modification techniques applied to materials, preparation of solutions, experimental conditions, electrochemical techniques adopted for corrosion studies and characterization of materials by various analytical techniques.

3.1 Materials

3.1.1 Introduction to the materials under investigation

Nickel base alloys are vitally important to modern industries because of their ability to withstand a wide variety of operating conditions involving corrosive environments, high temperature, and high stresses. These materials are widely used in aircraft and power generation turbines, rocket engines and other challenging environments including nuclear power and chemical processing plants [1]. Pure nickel is ductile and tough because of its face centered cubic (FCC) structure up to its melting point (1453 ^{0}C) and therefore, nickel and nickel base alloys offer freedom from ductile-to-brittle transition behaviour like other metals and alloys such as steels. Nickel has also good corrosion resistance in the normal atmosphere, in natural fresh water and deaerated non-oxidizing acid as well as caustic alkalis. Therefore, nickel is an excellent base metal to develop specialized alloys. Addition of chromium imparts improved resistance to oxidizing media such as nitric acid and chromic acid. It also improves resistance to high temperature oxidation and to attack by hot sulfur bearing gases. Although alloys have been formulated up to 50% Cr, alloying additions are usually in the range of 15 to 30%.

In the present thesis work, three nickel base superalloys have been investigated under various conditions to evaluate their corrosion behaviour for serving as a nuclear high level waste (HLW) storage container material. The chemical composition of the alloys are mentioned in Table 3.1.

Table 3.1 Chemical composition of the nickel base superalloys

Element	Ni	Cr	Fe	C	S	Mn	Cu	Si	Ti	Nb	N	Al	Mo
Alloy 600	74.2	14.7	9.6	0.03	0.008	0.53	0.30	0.15	0.26	-	-	0.3	0.30
Alloy 690	60	29.6	9.05	0.017	0.0013	0.21	<0.01	0.25	0.2	0.02	68 ppm	-	-
Alloy 693	60.9	29.3	3.96	0.097	0.002	0.19	<0.02	0.04	0.42	1.86	-	3.19	-

3.1.2 Specimen preparation

The nickel base superalloys were cut into coupons of dimensions 10 mm x 10 mm x 5 mm. These specimens were mechanically polished up to 600 grit finish using SiC emery sheet and subsequently different techniques were employed as mentioned below for the preparation of samples for microstructure characterization and investigation of corrosion behaviour.

➤ The specimens for microstructural characterization by optical microscopy and scanning electron microscopy (SEM) were polished up to 1 μm diamond finish and electrochemically etched. The etching details for various alloys are as follows;

(i) Alloy 600 was etched in 10% oxalic acid at the potential of 4 V for 20 s.

(ii) Alloy 690 was etched in 10% oxalic acid at the potential of 5 V for 15 s.

(iii) Alloy 693 was etched in 5% Nital (5% nitric acid in 95% ethyl alcohol) solution at the potential of 4 V for 45 s.

- The specimens required for evaluating the corrosion behaviour using electrochemical techniques were mounted with epoxy resin and a brass rod was attached using silver paste for electrical connection. The exposed surfaces of the mounted specimens were polished up to 1 µm diamond finish.

- Laser surface melting carried out on few specimens were mounted with the resin and then polished up to diamond finish, starting with 600 grit SiC paper. Proper care was taken while polishing so as to accommodate the laser melted zone (LMZ) within the exposed surface.

- For Huey test (practice C) the specimens were polished up to 600 grit finish in all sides with a minimum surface exposure of 5-6 cm^2.

- To carry out X-ray photoelectron spectroscopic (XPS) analysis the specimens were cut to less than 3 mm thickness and polished up to 1 µm diamond finish, followed by electrochemical passivation to obtain a passive film.

3.2 Medium

The primary medium used for all the corrosion studies was nitric acid. Nitric acid solutions were prepared from Ranbaxy made AR grade nitric acid of specific gravity 1.41 and maximum permissible impurity < 0.00005%.

3.2.1 Simulated HLW solution

Fission product (simulated) and corrosion product compounds in either oxide or nitrate form mentioned in Table 3.2 were taken in the required stoichiometric ratio and were dissolved in

3 M HNO_3. The simulated HLW solution prepared was used for all the electrochemical experiments.

3.2.2 Acidic-chloride solution

The acidic-chloride solutions for pitting corrosion studies were prepared in 3 M HNO_3 by adding different concentrations of chloride ions (500, 1000, 2000 and 3000 ppm). These solutions were prepared using reagent grade sodium chloride.

Table 3.2 Composition of simulated HLW

Element	[gL^{-1}]	Oxidation State	Chemical Used
Fe	0.72	+3	$Fe(NO_3)_3$
Cr	0.119	+6	CrO_3
Ni	0.107	+2	$Ni(NO_3)_2.6H_2O$
Na	5.5	+1	$NaNO_3$
K	0.224	+1	KNO_3
Cs	0.315	+1	$Cs\ NO_3$
Sr	0.031	+2	$Sr(NO_3)_2$
Zr	0.004	+4	$ZrO(NO_3)_2$
Ba	0.064	+2	$Ba(NO_3)_2$
La	0.18	+3	La_2O_3
Ce	0.06	+3	$Ce(NO_3)_3.6H_2O$
Pr	0.09	+3, +4	Pr_6O_{11}
Nd	0.12	+3	Nd_2O_3
Sm	0.0855	+3	Sm_2O_3
Y	0.06	+3	Y_2O_3
U	6.34	+4, +6	U_3O_8

3.3 Techniques for the modification of materials

3.3.1 Heat treatment

The conditions of heat treatment to carry out solution annealing (SA) and sensitization (SEN) are tabulated in Table 3.3. The as-received specimens were solution-annealed according to the temperature and time listed in Table 3.3 and were immediately quenched in water. Solution annealing was carried out to dissolve the pre-existing carbides and other precipitates in the matrix. A few of the solution-annealed specimens were further heat treated at the sensitization condition as per Table 3.3 and were allowed to cool in air to induce sensitization.

Table 3.3 Heat treatment parameters

Material		Temp (^{0}C)	Time (min)
Alloy 600	SA	1120	60
	SEN	800	60
Alloy 690	SA	1150	30
	SEN	700	60
Alloy 693	SA	1050	30
	SEN	700	60

3.3.2 Laser surface melting

Laser is a powerful tool to modify the microstructures of materials for improving various properties [2]. A laser beam is the heat source in laser materials processing. Though, laser is considered to be a light source, it is also a form of energy and it is a useful source of intense heat when concentrated by focusing. Because of their monochromatic, coherent and low divergence properties, lasers are able to produce high energy compared to any other ordinary

light source [3]. Hence, they are used to heat, melt and vaporize materials. Lasers are commonly used for welding, cutting and surface modification processes.

Laser surface melting (also known as skin melting or glazing) involves melting of a thin surface layer of a material which subsequently undergoes rapid solidification as a result of self-quenching, and resulting in alterations in the local microstructure. In this case, low power densities are used at higher traverse speeds to ensure that only a thin layer of the substrate which is just sufficient to induce rapid solidification is melted. The microstructural changes are accompanied by changes in properties such as hardness, corrosion resistance and wear resistance. The surface melting process results in three distinct zones in the material viz. laser melted zone (LMZ), heat affected zone (HAZ) and base material. When the melting process involves multiple scanning, there also exists an overlapping zone when the individual beam scan is made to overlap. Microstructure of the LMZ depends on the nature of the alloy. Microhardness of the LMZ is generally higher than that of the overlapping zone, whose hardness in turn is higher than that of the base material.

In the LMZ, increasing the scanning speed or decreasing the laser power results in a finer microstructure and higher microhardness. However, increasing the laser power increases the melt depth. Also, reducing the amount of overlap improves the overall microhardness [3].

In the present investigation, laser melting was obtained on one surface of the specimen using an indigenous continuous wave CO_2 laser beam at Raja Ramanna Centre for Advanced Technology (RRCAT), Indore, India. Various combinations of laser parameters like power and interaction time were used to select an optimum value of power density. The parameters used for optimum surface melting are reported in Table 3.4. A mixture of CO_2, N_2 and He gas in the ratio of 1:7:17 and at a total pressure of 50 mbar was purged during the laser

treatment. N_2 and He gas mixture was blown on the melted pool to prevent the melted zone from oxidation. In order to attain the desired thickness, it was necessary to control the laser melting parameters such as the output power, beam size, position of the focal point and the scan speed of the laser beam. To form a uniformly melted layer on the whole surface of a substrate, each beam scan was overlapped up to a certain (10–20 %) extent of the beam size.

Table 3.4 Laser parameters used for surface melting

Material	Power (W)	Current (A)	Track Width (mm)	Speed (mm/min)	Track Shift (mm)
Alloy 600	800	18	3	200	3
Alloy 690	800	18	1	60	1
Alloy 693	800	18	1	60	0.8

3.4 Surface morphology

3.4.1 Optical microscopy

Optical microscope is the conventional and most common device used for the characterization of an object, which cannot be observed with naked eye. Often it is referred to as the "light microscope", as it uses visible light and a system of lenses to magnify images of small samples. The image from an optical microscope can be captured by normal light-sensitive cameras to generate a micrograph. In the early days, images were captured by photographic film but recent advancement in complementary metal-oxide-semiconductor (CMOS) and charge-coupled device (CCD) cameras allow capturing of digital images. At present, a substantial growth in the application of optical microscope has been witnessed in characterizing a variety of materials from micron to sub-micron level. With continued development of specialized techniques such as new light source, electronic detection system,

video enhancement, advancement in chemical markers for visualizing biological structures, it has led to many advanced optical microscopes. Nevertheless, the conventional optical microscopy still maintains its popularity as the most widely used device for micron level characterization. The schematic of an optical microscope consisting of (a) illuminating source, (b) condenser lens, (c) stage to support the specimen, and (d) objective lens are shown in Fig. 3.1 [4].

In the present investigation, "Leica" make optical microscope was used to investigate the microstructure of as-received, heat treated and laser surface melted nickel base superalloys. It was also used to investigate the specimens after pitting corrosion study.
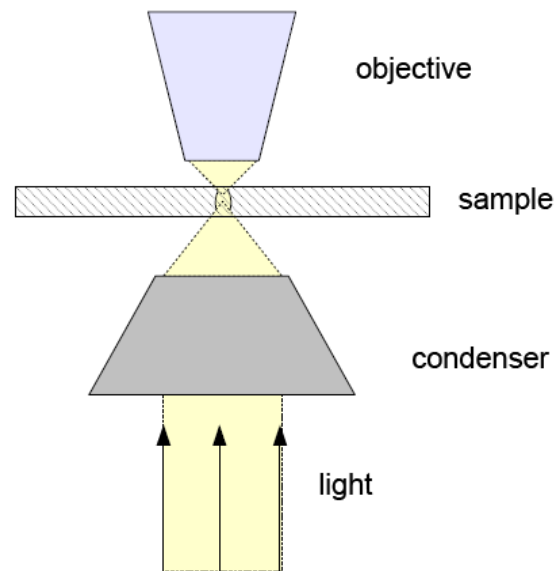
Fig. 3.1 Schematics of optical microscope [4]

3.4.2 Scanning electron microscopy

The scanning electron microscope (SEM) is one of the most advanced imaging devices used for inspecting topographies of materials. It is a type of electron microscope that produces

images of an object by scanning it with a focused beam of electrons. The electron beam is thermionically emitted from an electron gun fitted with a tungsten filament or lanthanum hexaboride (LaB_6) cathode. The accelerated electron beam of energy around 0.2 to 40 keV is focused by one or two condenser lenses to a spot of about 0.4 to 5 nm in diameter. Wavelength of the electron beam can be controlled by varying the velocity of electrons with the applied voltage. Interaction of electron beam with matter causes various physical phenomena such as absorption, reflection, backscattering and diffraction. In addition to these physical phenomena, it also causes the emission of low energy secondary electrons and X - rays, due to energy exchange between the electron beam and specimen. In SEM, the effects due to the secondary emission as well as backscattered electrons are measured. Figure 3.2 shows a block diagram of the working principle of SEM.
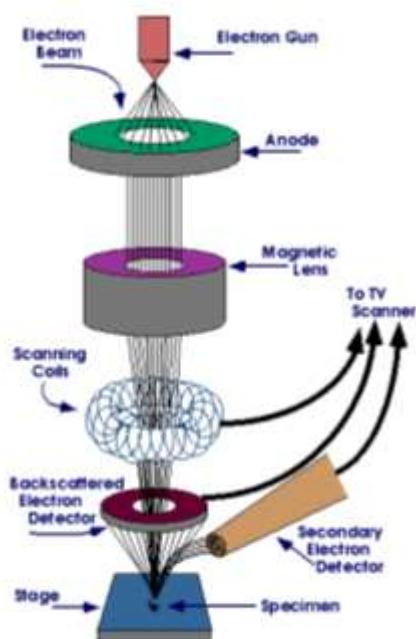
Fig. 3.2 Schematics of SEM [5]

Energy Dispersive X-ray spectroscopy (EDS) is one of the salient features of SEM and is used to determine the elemental composition of the surface of the samples. When electrons from the incident beam interact with atoms on the surface, secondary electrons from inner shells of the atoms are ejected out. Electrons from outer shells will drop into the vacant levels of the inner shells and this results in the emission of X – rays, characteristic of the atom. Hence, by measuring the energy of these characteristic X - rays, information about the elemental composition of the sample surface can be obtained.

In the present investigation, a "Philips – XL 30" Scanning electron microscope was used to observe the surface morphology of as-received, solution-annealed, sensitized and laser surface melted specimens. A "SNE3000M, Korea make" desktop mini-SEM was used to study the morphology of pitting corrosion and intergranular corrosion tested specimens.

3.4.3 X-ray photoelectron spectroscopy

X-ray Photoelectron Spectroscopy (XPS), also known as Electron Spectroscopy for Chemical Analysis (ESCA) is a widely used surface analysis technique used to investigate the bonding in different chemical states of elements. Its application is wide spread involving determination of the oxidation state of elements, identification of the chemical state of the metal oxide films, surface analysis of semi-conducting and insulating materials, elemental depth profiling etc. [6-8]. In the field of corrosion science, XPS study has been carried out for understanding the phenomena of passivity, compositional analysis at interface, selective oxidation phenomenon, assessment of mass transport process, and the interaction of materials in different electrochemical environment [9-11]. However, the inability to detect

hydrogen is one of the limitations in understanding the depth of overlapping mechanism of various corrosion phenomena [12].

In XPS, the specimen is irradiated with low-energy (~1.5 keV) X-rays, causing photoelectrons to be emitted from the specimen's surface. The kinetic energy of the photoelectron is determined by an electron energy analyzer. From the binding energy and intensity of a photoelectron peak, the elemental identity, chemical state and quantity of an element are determined. The selection of X-ray source depends on factors such as energy resolution of X-ray, energy of the photons produced and the ease of application as an anode material. Based on these criteria, Al-Kα (1486.6 eV) and Mg-Kα (1253.6 eV) are universally used as the primary sources of X-ray for XPS. The schematic of XPS process is represented in Fig. 3.3 for the emission of an electron from the 1s shell of an atom [13].
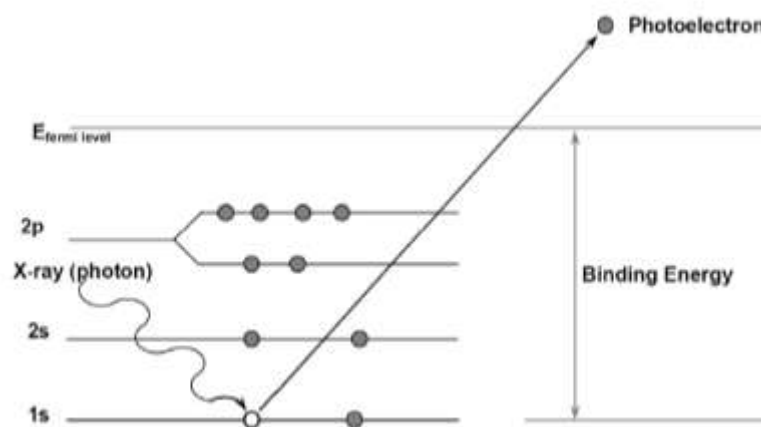
Fig. 3.3 Schematic of XPS process

The kinetic energy of the electron depends on the energy (hν) of the primary X-ray source. The characteristic parameter for the electron is its binding energy. The relation between these parameters is given by

$$E_B = h\nu - E_K - W \tag{3.1}$$

where 'E_B' is the binding energy, 'E_K' is the kinetic energy of the emitted photoelectron, 'hν' is the photon energy and 'W' is the work function of spectrometer. As the first approximation, the work function is assumed to be the difference between the energy of the Fermi level E_F and the energy of the vacuum level E_V, which is the zero point of the electron energy scale;

$$W = E_F - E_V \tag{3.2}$$

Each element has a characteristic electronic structure and hence, a characteristic XPS spectrum. In the spectrum, a number of peaks appear on the background. The background originates from the photoelectrons which undergo energy changes between photoemission from the atom and detection in the spectrometer. The peaks originating from photoemission can be grouped into three types: (*i*) from core levels, (*ii*) from valence levels at low binding energies (0 to 20 eV) and (*iii*) from X-rays excited as Auger emission (between 1100 and 1200 eV). The major information is derived from the core level peaks and the Auger peaks. The relative intensities are governed by the ionization efficiencies of the different core shells, designated by ionization cross section. The line width, defined as the full width at half maximum intensity (FWHM), is a convolution of several contributions; the natural width of the core level, the width of the X-ray line and the resolution of the analyzer [13, 14].

In the present thesis work, XPS characterization was carried out on the nickel base superalloys (Alloy 600, 690 and 693) which were electrochemically passivated in 3 M HNO$_3$ and simulated HLW. The specimens were electrochemically passivated for 1 h in the solution, at the passivation potentials (E$_{pass}$) obtained from the corresponding polarization curves. The passivated surfaces were analyzed for the composition using XPS. Measurements were carried out using SPECS make XPS system with a monochromatized Al-Kα (E=1486.74 eV) source and a PHOIBOS 150 analyzer with a chosen energy resolution for recording survey spectra. The pressure in the analysis chamber was maintained at 2x10^{-9} mbar throughout the measurements. The spectra were collected using SPECS Lab 2 data analysis software supplied by the manufacturer.

3.4.4 X-ray diffraction technique

X-ray diffraction (XRD) method is one of the most important and primary characterization tools used in chemistry, physics and materials science to elucidate the crystal structure and lattice parameters of solid materials and single crystals [15-17]. It is a scattering process where X-rays are scattered by the electrons of atoms/ions without changing the in wavelength. Only when certain geometrical conditions stipulated by Bragg's law (Eq. 3.3) are satisfied, a diffracted beam is produced by such scattering,

$$n\lambda = 2d \sin\theta \qquad (3.3)$$

where λ is wavelength of the X-ray used, d is inter planar spacing of the analyte, θ is the angle of incidence of the X-rays and n is the order of reflection.

X-ray diffraction technique requires an X-ray source, specimen under investigation and a detector. The X-rays are generated by a cathode ray tube, filtered to produce monochromatic

radiation, collimated to concentrate and directed towards the specimen. A constructive interference (and a diffracted ray) is produced by the interaction of the incident rays with the specimen by satisfying Bragg's Law. The diffracted X-rays are then detected, processed and counted. By scanning the specimen over a range of 2θ values, all possible diffraction directions of the lattice could be obtained. Conversion of the diffraction peaks to d-spacing allows the identification of the phases in crystalline materials because each material has a set of unique d-spacing. Typically, this is achieved by the comparison of d-spacing with standard reference patterns [15]. The X-ray radiation most commonly used is that emitted by copper, whose characteristic wavelength for the Kα radiation is 1.5418 Å. Other metal targets commonly used in X-ray generating tubes include Cr (Kα - 2.29 Å), Fe (Kα - 1.94 Å), Co (Kα - 1.79 Å) and Mo (Kα - 0.71 Å). X-ray diffraction methods employ single crystals as well as powder samples. Single crystal method is used to determine the space group and crystal structure while the powder diffraction technique is widely employed for phase identification and crystallite size determination.

In the present investigation, XRD characterization of the as-received and laser surface melted specimen's surface was carried out and compared with the standard patterns available in the literature. The spectra were recorded using a Philips make X'pert pro diffractometer. The specimen's surface was examined from 10-80^0 2θ range using Cu K$_\alpha$ radiation (40 kV, 30 mA, λ = 1.5418 Å) with a scan rate of 0.05^0/sec for 4 s counting time at each step.

3.5 Electrochemical study

3.5.1 Electrochemical impedance spectroscopic measurements

Electrochemical impedance spectroscopy (EIS) is a powerful and well established technique used for the characterization of electrochemical properties of the materials and their interfaces in different environments. Impedance is the opposition to the flow of current, which is given by the ratio of applied voltage to the resulting current. It is the combination of resistance and reactance in an electrochemical system [18]. The locus of impedance as a function of angular frequency is called impedance spectrum. This technique involves the determination of cell impedance, in response to a small AC signal at any constant DC potential (preferably at the OCP to minimize the DC currents), over frequencies ranging from a micro to mega-hertz.

Impedance spectroscopy is widely used to analyze the complex properties in a material such as dielectric properties, mass transport, defect density, passive film stability, coating degradation, microstructural and compositional effects on the conductance of solids, and impedance of biological membranes [19-24]. The wide spread application of this technique is due to the use of very small amplitude signal without disturbing the desired properties of materials to be measured. The major advantages of this technique are its nondestructive nature due to the application of very low potential, the rapidity in measurements with potentiostat and frequency response analyzers and data processing using appropriate software programs. Also, it has the advantage of providing the required information on the formation/interfacial reactions and protection mechanisms of a given surface layer [25, 26]. On the other hand, the difficulty in interpreting the data is major deficiency of this

technique. The most common approach is based on the equivalent circuit concept, exemplified in the model of Randles [27].

EIS technique has been successfully applied to the study of corrosion systems for a few decades and is proved to be a powerful and accurate method for measuring corrosion rates. In corrosion experiments, generally 10 to 50 mV sinusoidal voltage signal is applied to a corroding electrode interface and the current signal resulting at the same excitation frequency is measured. The impedance is measured over a domain of discrete frequencies ranging from 0.001 to 10^6 Hz. At the high-frequency end, the interfacial capacitance will dominate and hence, only the electrolyte's resistance will contribute to the impedance. At lower frequencies, interfacial resistance will contribute to the impedance. Electrochemical and diffusional processes associated with corrosion are detected at frequencies in the range $10\text{-}10^{-6}$ Hz. However, below the frequency of 10^{-3} Hz, the metallic electrochemical interface will become unstable and reliable measurements may not be possible [18].

Impedance Z, can be expressed in complex number notation as

$$Z = Z' + jZ'' \tag{3.4}$$

where Z' and Z'' represent the real and Z'' represents the imaginary components respectively. Nyquist plot and Bode plot are two types of diagrams which are most frequently used for the graphical representation of impedance data. In the Nyquist plot, the impedance is represented by a real part and an imaginary part. Therefore, the Nyquist plot is termed as the complex plane impedance plot. In the Bode plot, the modulus of the impedance and the phase angle are both plotted as a function of frequency. For a simple resistor-capacitor (*R-C*) circuit, the Nyquist plot is characterized by a semicircle. If the system is complicated, the spectra have to be fitted with an equivalent circuit model, which is representative of the

microstructural features of the materials [28, 29]. Nyquist plot allows an easy prediction of the properties of the electrode-electrolyte interface; however, it does not provide the information regarding the frequency dependence of impedance [30, 31]. Bode plot provides all the necessary information for clear interpretation of the results. The interpretation of the impedance data from either Nyquist or Bode plot is carried out by means of electrical equivalent circuit consisting of circuit elements and representing the physical phenomenon occurring in the electrochemical cell. In general, the circuit consists of the following basic elements,

(a) Charge transfer resistance (R_P) whose impedance is given as $|Z| = R$

(b) Solution resistance (R_S)

(c) Capacitance of double layer ($C\Omega$) at electrode-electrolyte interface whose impedance is given by $|Z| = 1/j\omega C$.

In order to account for non-ideal behaviour of capacitance, real capacitance is replaced by constant phase element (CPE) whose impedance is given by Eq 3.5.

$$Z_{CPE} = 1/[T(j\omega)^n] \hspace{3cm} (3.5)$$

where T and n are frequency-independent fit parameters, $j = (-1)^{1/2}$ and $\omega = 2\pi f$, where f is the frequency in Hz.

n is defined as $n = 1 - 2\alpha/180$, where α is the depression angle (in degree).

When $n = 1$, CPE describes an ideal capacitor.

The schematic of an electrical equivalent circuit consisting of the above circuit elements is shown in Fig. 3.4. Nevertheless, the circuit diagram varies with the nature of working electrode, and the physico-chemical process occurring at the electrode-electrolyte interface. Depending upon the shape of the EIS spectrum, a circuit model and initial circuit parameters

are assumed and input is provided by the operator. The program then fits the best frequency response of the given EIS spectrum, to obtain the fitting parameters. The quality of the fitting is judged by how well the fitting curve overlaps the original spectrum. By fitting the EIS data it is possible to obtain a set of parameters which can be correlated with the electrochemical properties of the substrate.
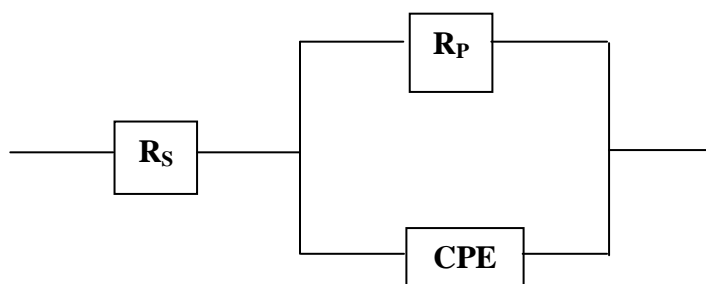
Fig. 3.4: Equivalent circuit for impedance analysis with one time constant

The instrumentation for carrying out the impedance measurement consists of a potentiostat and an electrochemical cell. The electrochemical cells for conducting the study consists of (a) working electrode i.e. specimen to be tested, (b) a non-polarizable counter electrode for completing the circuit, and (c) a reference electrode with respect to which potential has to be applied. The schematic of the electrochemical cell for carrying out polarization experiments is shown in Fig. 3.5. Reference electrode is often separated from the solution by luggin probe, and is placed close to the working electrode to eliminate the effect of solution resistance.

A three-electrode cell comprising two platinum electrodes as counter electrode was used for the electrochemical experiments in the present thesis. The nickel base superalloys (Alloy 600, 690 and 693) were used as working electrodes. All potentials were measured with reference to saturated calomel electrode (SCE) using luggin probe and the same electrolyte

as the bridge. Experiments were carried out at the solution temperature of 25^0C in both 3 M

HNO_3 and simulated HLW. The specimens were allowed to equilibrate for 30 minutes and

the open circuit potential (OCP) was monitored. EIS technique was used to investigate the

corrosion behaviour of nickel base superalloys in 3 M HNO_3 and simulated HLW media.

The impedance data were recorded using an AUTOLAB PGSTAT30 FRA system, at the

OCP and frequency range was adjusted from 100 KHz to 0.01 Hz with an applied ac

perturbation of 10 mV. The impedance data were analyzed by a commercial software

package "NOVA". According to literature, values of error less than 5% in modeling of EIS

results give the best electrochemical interpretation. Constant phase element has been used in

the present investigation to obtain better fit for the experimental data, which would represent

the capacitance of the passive oxide layer.
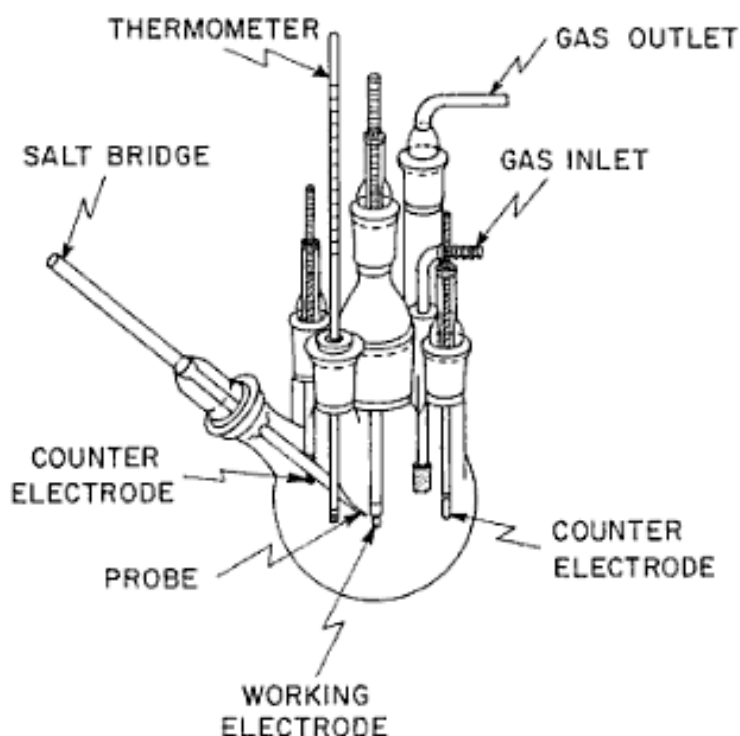
Fig. 3.5: Schematic of electrochemical cell for corrosion study [32].

3.5.2 Potentiodynamic anodic polarization study

Potentiodynamic polarization is the one of the most popular and advanced techniques often used for laboratory scale corrosion testing of materials. The information provided by this technique regarding the corrosion mechanisms, corrosion rate and susceptibility of specific materials to corrosion in a particular environment is significant. This technique is applied to assess the behaviour of the materials in term of their corrosion resistance. One of the major advantages of potentiodynamic polarization study is the rapid determination of corrosion rates as compared to traditional methods like weight loss measurements. In this technique the corrosion rate is determined by extrapolating the linear segment of cathodic and anodic regions which is known as Tafel extrapolation. The intersection of the Tafel lines gives the value of corrosion potential and corrosion current density. Polarization methods involve changing the potential of the working electrode and monitoring the current which is produced as a function of time or potential. A polarization curve indicates whether or not a material is in active, passive or active-passive state. Apart from this, passivity and corrosivity can be determined in the presence of oxidizing-reducing species also.

The instrumentation for carrying out the polarization study is similar to the set-up employed for impedance measurements.

A three electrode set up connected to a potentiostat has been used for the polarization studies reported in this thesis. The nickel base superalloys were used as working electrodes. All potentials were measured with reference to saturated calomel electrode (SCE) using luggin probe using the same electrolyte as the bridge. The specimens were allowed to stabilize at OCP for 30 minutes and subsequently subjected to potentiodynamic anodic polarization at a potential of 200 mV below OCP, at a scan rate of 10 mV per minute under aerated

conditions. The experiments were stopped beyond transpassive region where there was a monotonic increase in anodic current. From the polarization curve obtained, corrosion potential (E_{corr}), transpassive potential ($E_{TP)}$ and passivation current density ($I_{pass)}$ were derived.

3.5.3 Double loop electrochemical potentiokinetic reactivation test

For detecting the susceptibility to intergranular corrosion (IGC) in austenitic stainless steel, five methods have been described by ASTM Practice A 262 [33], which has been adopted for austenitic nickel base alloys. However, none of these tests meets the dual requirement of providing a quantitative and nondestructive method. Practice A is rapid and nondestructive, but not quantitative. The other four tests are quantitative; however, require testing of specimens in hot, concentrated acids for long durations. Cihal et al. [34] and Prazak et al. [35] have proposed a technique called electrochemical potentiokinetic reactivation (EPR) test to comply to the requirement of a rapid, quantitative and nondestructive method for detecting the extent of sensitization, which was further modified by Novak et al. [36]. The EPR test is based on the preferential breakdown of the passive film on the sensitized grain boundaries, where chromium is depleted during a controlled potential sweep from the passive to active regions. The test assumes that only sensitized grain boundaries become active, while grain bodies and unsensitized grain boundaries remain passive. Thus, highly sensitized materials should show a greater increase in current density than the less sensitized or unsensitized materials. Double loop electrochemical potentiokinetic reactivation (DL-EPR) is the advanced and improved method of measuring the degree of sensitization, wherein the results are more accurate and reproducible. In the double loop test, the specimen

is first polarized anodically through the active region and then the reactivation scan in the reverse direction is carried out. When the specimen is polarized anodically at a given scan rate from the corrosion potential to a higher potential in the passive area, it leads to the formation of a passive film on the whole surface of the specimen. When scanning direction is reversed and the potential is decreased at the same rate to the corrosion potential, the passive film breaks down on chromium depleted area. Figure 3.6 shows that two loops are generated, an anodic loop and a reactivation loop during the test. The DL-EPR test is independent of surface finish and the presence of random pitting or metallic inclusions because of the cleaning effect on the specimen surface during the forward anodic scan, which is a major advantage compared to the single loop EPR test [37-39]. The reproducibility of the double loop test is excellent when optimum conditions are maintained. The optimum conditions are determined by examining parameters such as surface finish, scan rate, temperature and potassium thiocyanate concentration which is used as an activator. The standard test solution for DL-EPR test is sulphuric acid containing potassium thiocyanate. KSCN is a strong corrosive agent and a grain boundary activator [40]. It has been used as a depassivating agent in the test, since it reactivates the Cr depleted regions by destroying preferentially the oxide films formed on those regions [35]. To selectively attack only the Cr depleted grain boundary zones with a high discriminating power of reactivation, appropriate addition of KSCN is necessary in the DL-EPR test [41]. With increasing concentration of KSCN, the corrosion current density increases sharply due to the pitting corrosion around the inclusions in the matrix [42]. Optimization of KSCN concentration depends upon the reactivation of Cr depleted regions and suppression of other types of corrosion such as pitting. Degree of sensitization (DOS) is defined as the percent ratio of the

maximum current density in the reactivation loop to that of anodic loop. The DOS is calculated using the following equation [41-43]

$$DOS \% = I_r/I_a \times 100 \tag{3.6}$$

where I_r is the reactivation peak current density and I_a is the anodic peak current density.

The ratio I_r/I_a, is sensitive towards solution concentration, temperature and scan rate [44, 45]. Higher current ratio is associated with larger degree of sensitization in the material [46, 47].
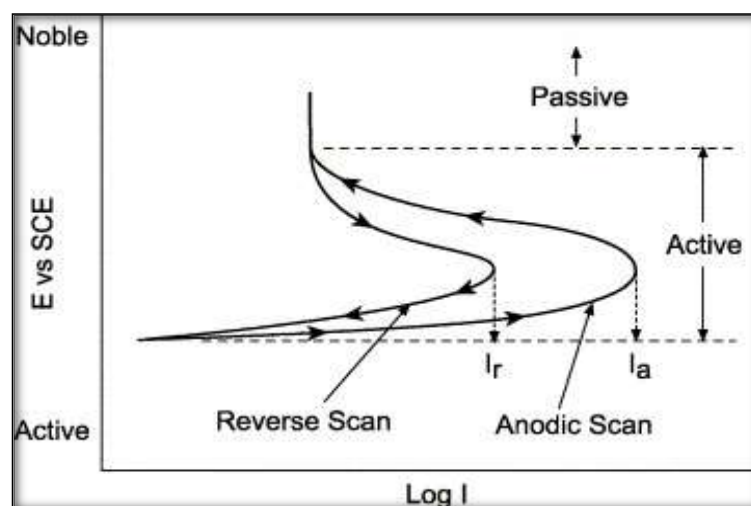
Fig. 3.6: Schematics of DL-EPR test

The DL-EPR test was carried out to measure the DOS of solution-annealed, sensitized and laser surface melted specimens. For the testing, specimens were polished up to 1000 grit using silicon carbide emery paper. All specimens were cleaned with soap solution and further cleaned with acetone. DL-EPR test was conducted in 0.5 M sulphuric acid containing 0.0001 M potassium thiocyanate (KSCN), taken in a polarization cell [48, 49]. Dry, oxygen free argon gas was purged for one hour before and during the test, to remove dissolved oxygen from the aqueous solution. The mounted specimen was immersed in the solution and

the OCP was noted after 30 minutes of immersion. The polarization test was carried out using the specimen as working electrode, platinum as counter electrode and saturated calomel electrode (SCE) as the reference electrode. In the anodic polarization, the specimen was polarized to a potential of 600 mV (SCE) in the passive region, after which the scanning was reversed. A scan rate of 60 mV per minute was maintained for the forward and reverse scans. All the experiments were carried out at room temperature. The maximum anodic current (I_a) and maximum reactivation current (I_r) were measured from the anodic and reactivation anodic curves respectively. The degree of sensitization was calculated using Eq 3.6.

3.6 Pitting corrosion testing

Metals and alloys, which are resistant to corrosion usually depend on their ability to form and maintain a thin film of passivated oxide for protecting their surface. The passive film is self-healing in nature and forms new layer whenever damage occurs on the surface. The thickness of such self-healing passive oxide layer ranges from a monolayer to a few angstrom [50]. However, under the influence of aggressive anions such as halides, the breakdown of such passive films occur at weak sites on the surface. The localized anodic corrosion site is generally surrounded by a cathodic area that remains passive, which usually leads to severe pitting. Pitting corrosion is the formation of microscopic cavities on the surface of metal/alloys, due to direct corrosion of heterogeneities present on the surface or due to localized damage caused to a protective film present on the surface [50, 51]. Pits always initiate at some chemical or physical heterogeneity on the surface, such as inclusions, second phase particles, solute-segregated grain boundaries, mechanical damage, or

dislocations [52]. Pitting is considered to be autocatalytic in nature, i.e. once a pit starts to grow, the surroundings are altered such that further pit growth is promoted [52]. Pitting corrosion resistance of various alloys are significantly affected by the metallurgical parameters, properties of chemical environment and the properties of passive film. Metallurgical parameters include alloy composition, heat treatment, cold working, sensitization, grain size, inclusions and secondary precipitates [53-64]. The properties of chemical environment like pH, temperature, concentration, velocity etc. and that of the passive film like conductivity, structure, composition, capacitance etc. are known to influence pitting corrosion [61, 62, 65-67]. Among the chemical environment parameters, chloride ions are the most aggressive species inducing pitting of nickel base alloys [68].

The pitting corrosion studies were carried out using potentiodynamic anodic polarization technique, in 3 M HNO_3 solution containing different concentrations of chloride ions (500, 1000, 2000 and 3000 ppm) for the present work. The solutions were prepared using reagent grade nitric acid, sodium chloride and double distilled water. Before conducting anodic polarization experiments, the specimens were allowed to stabilize at OCP for 30 minutes and subsequently subjected to polarization at a potential of 200 mV (SCE) below OCP, at a scan rate of 10 mV per minute under aerated conditions. The experiments were stopped beyond transpassive region where there was a monotonic increase in anodic current. All potentials were measured with reference to saturated calomel electrode (SCE) using luggin probe with the same electrolyte as the bridge. The potential at which the current increases monotonically beyond 25 μA after the passive region was confirmed as E_{pit} [63, 69]. E_{pit} is the potential above which passive alloys are susceptible to pitting corrosion, but below

which pits cannot be formed, although existing pits can grow, if the applied potential is greater than the protection potential.

3.7 Intergranular corrosion

Though the passive film formed on a material is uniform and free of pores, their stability may be weakened locally. The properties of the film change in the areas where the material surface is associated with the grain boundary precipitates. Such a heterogeneity is very dangerous since it weakens the material without producing much change in the outward appearance. Corrosion attack under such circumstances leads to intergranular attack, which may result in the loss of strength and ductility of the material. Intergranular attack is accelerated by potential differences between grain and grain boundaries, i.e. attack is determined by availability of anodic sites at grain boundaries. Therefore, to create andic sites, the specimen should get passivated. The usual form of intergranular corrosion (IGC) occurs due to sensitization which is the depletion of chromium and formation of chromium carbide precipitates adjacent to grain boundaries. The degree of sensitization of a material depends upon the concentration of chromium and carbon and generally increases with increase in the concentration of carbon and decreases with chromium concentration. Chromium from the solid solution is utilized for Cr-rich $Cr_{23}C_6$ formation resulting in lower chromium content adjacent to such carbides along the grain boundaries. Such chromium depleted regions are vulnerable to corrosive attack, because it does not contain sufficient chromium to form passive film.

The evaluation of the susceptibility to intergranular corrosion is made according to the ASTM A-262, Standard Practice C (a procedure for conducting the boiling nitric acid test)

by calculating an average corrosion rate over the five 48 hour time period. However, the results of the test is only a measure of intergranular corrosion resistance of a material and not necessarily a measure of the performance of the material in other corrosive environments, and not a basis for predicting resistance from other forms of corrosion like general corrosion, pitting and stress corrosion cracking.

The schematic of the set up for practice C test is represented in Fig. 3.7. A 1 litre Erlenmeyer flask equipped with a cold finger type condenser was used for the test. The specimen was hanged using a glass hook. The test solution was 65 % nitric acid, prepared by adding distilled water to concentrated nitric acid. After immersing the specimen in the acid taken in the flask, cooling water was passed through the condenser and the acid was heated to boiling on a hot plate throughout the test period. After each test period, the specimen was removed, rinsed with water, and dried, cleaned with acetone and the weight of the specimen was taken with accuracy up to 0.0001 g.

The effect of the acid on the material was estimated by determining the loss of weight of the specimen after each test period and for the total of the test periods. The corrosion rates are reported as mils per year.

The rate of corrosion is measured using the following equation;

Rate of corrosion = 472 x (7290 x W) / (A x d x t) mils per year   (3.7)

where:

t = time of exposure in h,

A = total surface area in cm^2,

W = Weight loss in g and

d = density of the specimen in g/cm^3.

The results are reported for individual periods as well as the average for the five test periods. In the present investigation the intergranular corrosion resistance of the three nickel base superalloys under various conditions (as-received, solution-annealed and sensitized) were tested using Huey test (in 65% boiling nitric acid for 240 h) and the corrosion rates were determined using Eq. 3.7. The IGC tested specimens were observed under SEM to investigate the nature and extent of corrosion attack after the Huey test.
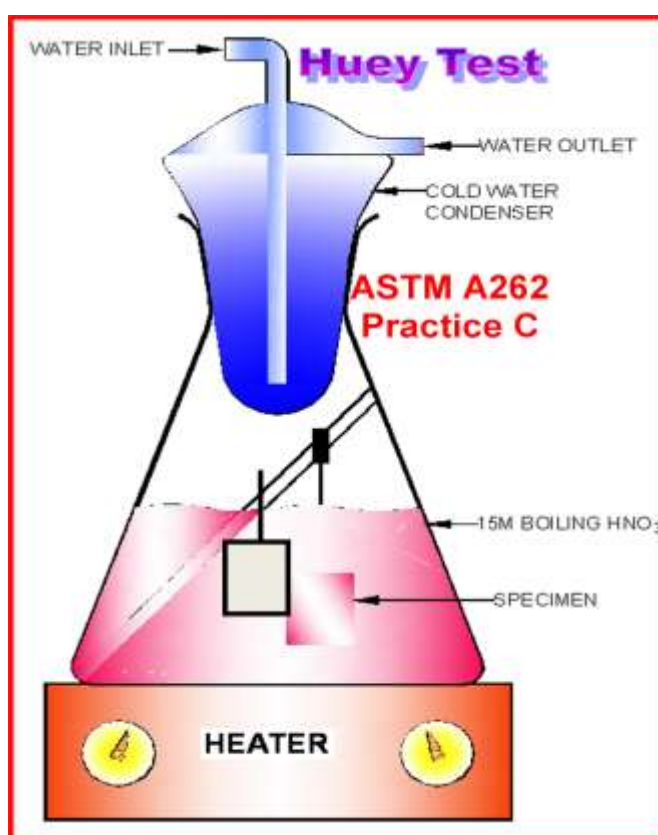
Fig. 3.7: Schematic set up for practice C test

References:

[1]   T. M. Pollock, S. Tin, J. Propulsion and Power, 22 (2006) 361.

[2]   S. T. Picraux, L. E. Pope, Science, 226 (1985) 615.

[3]   E. Kannatey-Asibu, Jr. Principles of laser materials processing, John Wiley & Sons, Inc., Publication.

[4]   www.microscopyu.com.

[5]   http://www.purdue.edu/rem/rs/sem.htm.

[6]   H. C. Swart, G. L. P. Berning, Mater. Chem. Phys. 41 (1995) 251.

[7]   J. H. Liu, R. Mendonca, R. W. Bosch, M. J. Konstantinovic, J. Nucl. Mater. 393 (2009) 242.

[8]   J. M. Sanz, L. Soriano, P. Prieto, G. Tyuliev, C. Morant, E. Elizalde, Thin Solid Films, 332 (1998) 209.

[9]   B. Elsener, A. Rossi, Electrochim. Acta, 37 (1992) 2269.

[10] C. Donik, D. Mandrino, M. Jenko, Vacuum, 84 (2010) 1266.

[11] N. Khalil, J. S. L. Leach, Electrochim. Acta, 40 (1995) 1769.

[12] S. J. Kerber, J. J. Bruckner, K. Wozniak, S. Seal, S. Hardcastle, T. L. Barr, J. Vac. Sci. Technol. A 14 (1996) 1314.

[13] D. Briggs, M. P. Seah, Practical Surface Analysis by Auger and X-ray Photoelectron Spectroscopy, John Wiley and Sons, Chichester (1983).

[14] D. R. Baer, M. H. Engelhard, J. Electron. Spectrosc. Relat. Phenom., 178–179 (2010) 415.

[15] B. D. Cullity, Elements of X-ray Diffraction, Addison-Wesley Publishing Co., Inc. Massachusetts, USA (1956).

[16] A. R. West, Solid State Chemistry and its Applications, John Wiley & Sons, Singapore (2008).

[17] R. A. Butera, D. H. Waldeck, J. Chem. Education, 74 (1997) 115.

[18] R. G. Kelly, J. R. Scully, D. W. Shoesmith, R. G. Buchheit, Electrochemical Techniques in Corrosion Science and Engineering. Marcel Dekker, Inc. New York, 2003.

[19] J. R. Dygas, Solid State Ionics, 176 (2005) 2065-2078.

[20] I. Betova, M. Bojinov, V. Karastoyanov, P. Kinnunen, T. Saario, Electrochim. Acta, 55 (2010) 6163.

[21] R. Cabrera-Sierra, J. M. Hallen, J. Vazquez-Arenas, G. Vazquez, I. Gonzalez, J. Electroanal. Chem. 638 (2010) 51.

[22] T. Ohtsuka, T. Otsuki, Corros. Sci. 40 (1998) 951.

[23] M. Kendig, F. Mansfeld, S. Tsai, Corros Sci, 23 (1983) 317.

[24] V. Freger, S. Bason, J. Membrane Sci, 302 (2007) 1.

[25] R. L. Zeller, R. F. Savinell, Corr. Sci. 26 (1986) 389.

[26] A. Popova, M. Christov, Corros. Sci. 48 (2006) 3208–3221.

[27] J. E. B. Randles, Discuss. Faraday Soc. 1 (1947) 11.

[28] J. G. Fletcher, A. R. West, J. T. S. Irvine, J. Electrochem. Soc. 142 (1995) 2650.

[29] L. Chao, H. Hui, N. Liyong, Z. Chungen, Chinese J. Aeronautics 24 (2011) 514.

[30] M. K. Orazem, B. Tribollet, Electrochemical impedance spectroscopy, Eds: M. E. Orazem, B. Tribollet, Wiley Inter-Science, 2008.

[31] J. R. Macdonald, W. B. Johnson, Fundamentals of impedance spectroscopy, Eds: E. Barsoukov, J. R. Macdonald, John Wiley and Sons, 2005.

[32] Z. Ahmad, Principle of corrosion engineering and corrosion control, Ed: Zaki Ahmad, Elsevier, 2006.

[33] ASTM Standard Practice A 262-93a, "Standard Practice for Detecting Susceptibility to Intergranular Attack in Austenitic Stainless Steels," in Annual Book of Standards, Vol. 3.02 (Philadelphia, PA: ASTM, 1988).

[34] C. Cihal, A. Desestret, M. Froment, G. H. Wagner, "Tests for Evaluation of Sensibility of Stainless Steels to Intergranular Corrosion," Proc. 5th European Corros. Cong. (Paris, France: European Federation on Corrosion, 1973), p. 249.

[35] M. Prazak, Corrosion 19 (1963) 75.

[36] P. Novak, R. Stepec, F. Franz, Corrosion 31 (1975) 344.

[37] M. Akashi, T. Kawamoto, F. Umemura Corros. Eng. 29 (1980) 163.

[38] A. P. Majidi, M. A. Streicher, Corrosion 40 (1984) 584

[39] Z. Fang, Y. S. Wu, L. Zhang, J. Q. Li, Corrosion 54 (1998) 339.

[40] J. D. Kim, J. H. Moon, Corros Sci. 46 (2004) 807.

[41] M. K. Ahn, H. S. Kwon, J. H. Lee, Corrosion 51 (1995) 441.

[42] Y. S. Lim, H. P. Kim, J. H. Han, J. S. Kim, H. S. Kwon, Corros Sci. 43 (2001) 1321.

[43] M. Casales, V. M. Salinas-Bravo, A. Martinez-Villafane, J. G. Gonzalez-Rodriguez, Mater. Sci. Eng. A 332 (2002) 223.

[44] A. Roelandt, J. Verrecken, Corrosion 42 (1986) 289.

[45] M. F. Maday, A. Miginone, M. Vittori, Corros. Sci. 28 (1988) 995.

[46] Y. S. Sato, P. Arkom, H. Kokawa, T. W. Nelson, R. J. Steel, Mater. Sci. Eng. A 477 (2008) 250.

[47] M. Shimada, H. Kokawa, Z. J. Wang, Y. S. Sato, I. Karibe, Acta Mater. 50 (2002) 2331.

[48] M. Casales, M. A. Espinoza-Medina, A. Martinez-Villafane, V. M. Salinas-Bravo, J. G. Gonzalez-Rodriguez, Corrosion 56 (2000) 1133.

[49] H. T. Lee, J. L. Wu, Corros. Sci. 52 (2010) 1545.

[50] U. Kamachi Mudali, M. G. Pujar, Corrosion of austenitic stainless steels-mechanism, mitigation and monitoring (Eds. H. S. Khatak, Baldev Raj), Narosa Publications (2002) p. 74.

[51] G. T. Burstein, Nature 350 (1991) 188.

[52] G. S. Frankel, J. Electrochem. Soc. 145 (1998) 2186.

[53] Y. M. Kolotykin, Corrosion 19 (1963) 261.

[54] Z. Szklarska-Smialowska, Pitting corrosion of metals (NACE, Houston, TX, 1986) p.144.

[55] J. B. Lumseden, Proc. Int. Conf. on Corrosion of Nickel Base Alloys, Cincinnati, OH, p. 181 ASM, (1985).

[56] R. Stefec, F. Franz, A. Holecek, Werkst. Korro. 30 (1979) 189.

[57] C. R. Rarey, A. H. Aronson, Corrosion 28 (1972) 255.

[58] B. Mazza, P. Pedeferri, D. Sinigaglia, A. Cigada, G. A. Mondora, G. Re, G. Taccani, D. Wenger, J. Electrochem. Soc. 126 (1979) 2075.

[59] A. J. Sedriks, Corrosion of Stainless Steels, John-Wiley and Sons, New York (1996).

[60] A. J. Sedriks, Proc. Int. Conf. on Stainless Steels-85, p. 125, The Institute of Metals, London (1985).

[61] U. Kamachi Mudali, P. Shankar, S. Ningshen, R. K. Dayal, H. S. Khatak, Baldev Raj, Corros. Sci. 44 (2002) 2183.

[62] Z. Szklarska-Smialowska, Corrosion 27, 223 (1971).

[63] U. Kamachi Mudali, R. K. Dayal, J. B. Gnanamoorthy, P. Rodriguez, ISIJ Int. 36 (1996) 799.

[64] S. Ningshen, U Kamachi Mudali, J. Mater. Eng. Perform. 19 (2010) 274.

[65] C. J. Semino, P. Pedeferri, G. T. Burstein, T. P. Hoar, Corros. Sci. 19 (1979) 1069.

[66] J. Hickling, N. Wieling, Corrosion 37 (1981) 147.

[67] G. Palumbo, P. J. King and K. T. Aust, Corrosion 43 (1987) 37.

[68] M-Y. Chang, G-P. Yu, J. Nucl. Mater. 202 (1993) 145.

[69] S. Girija, U. Kamachi Mudali, V. Shankar, R.K. Dayal, Trans. Indian Inst. Met. 55 (2002) 439.

CHAPTER 4

Corrosion Behaviour of Nickel Base Superalloys in Simulated High Level Waste Medium

Corrosion Behaviour of Nickel Base Superalloys in Simulated High Level Waste Medium

Corrosion behaviour of three nickel base superalloys (Alloy 600, 690 and 693) in as-received condition was studied in simulated high level waste (HLW) medium. Electrochemical studies were carried out in simulated HLW medium, using potentiodynamic anodic polarization and electrochemical impedance spectroscopic techniques. All the alloys, in the as-received condition were found to possess good corrosion resistance in simulated HLW. Microstructural characterizations revealed austenitic microstructure for all the Alloys. X-ray photoelectron spectroscopic (XPS) study of the passive film formed in simulated HLW medium revealed the formation of mixed oxides of Ni-Cr-Fe for Alloy 690 and 693 whereas predominantly oxides of Cr only were observed for Alloy 600. Studies were undertaken to evaluate the pitting corrosion resistance of the alloys in 3 M HNO_3 containing various concentrations of chloride ions under aerated condition. Alloy 690 showed superior pitting corrosion resistance compared to Alloy 693 and Alloy 600. Huey test as per ASTM A262 practice C revealed superior intergranular corrosion resistance of Alloy 690 compared to Alloy 693 and Alloy 600.

4.1 Introduction

Austenitic stainless steels are widely used in nuclear industries for the storage of radioactive nuclear waste. However, they are susceptible to sensitization in the heat affected zones during welding. Since sensitization involves chromium depletion at grain boundaries, it makes the materials susceptible to intergranular corrosion (IGC). These alloys also suffer from pitting corrosion and transgranular stress corrosion cracking

(TGSCC) in chloride containing solutions [1]. These can cause concern over radioactive leakage and hence, environmental safety. This necessitates the search for some advanced materials which can minimize these problems.

Austenitic nickel base alloys appear to be a promising alternative to austenitic stainless steels because of their better corrosion resistance, thermal conductivity and mechanical properties. Using these alloys, complex processes and waste streams can be handled safely due to their versatility [2]. These alloys possess higher tolerance for alloying elements in solid solution than stainless steels and other iron base alloys. The good metallurgical stability of the nickel base alloys make them a better alternate to stainless steel. Owing to the excellent mechanical and physical properties, nickel base superalloys are extensively employed in nuclear power plants.

Alloy 600 is one of the nickel base solid solution strengthened superalloy with major elemental composition as Ni-16Cr-9Fe [2]; it is non-magnetic, corrosion and oxidation resistant alloy. The major elements nickel and chromium, provide good resistance to oxidizing environments. In nuclear power plants, Alloy 600 is used as steam generator tubes [2-5]. The selection of this material is because of its good mechanical strength, thermal conductivity, high formability and corrosion resistance [6, 7]. Alloy 690 is a solid solution strengthened, austenitic nickel base superalloy with the composition similar to that of Alloy 600 except that its chromium content has been approximately doubled from about 15 to 30%. This alloy was developed to mitigate corrosion related problems encountered in high temperature aqueous environments associated with nuclear steam generator tubing material [8]. In addition to the increase in chromium content, the carbon content was decreased to below 0.03% in Alloy 690, which results in good stress corrosion cracking (SCC) and intergranular stress corrosion cracking (IGSCC) resistance and mechanical properties [9, 10]. Alloy 693 is another nickel base superalloy, which is

a modified version of Alloy 690 and is expected to offer high corrosion resistance and longer service life. The investigations of corrosion behaviour on Alloy 693 have been limited as compared to Alloy 690. In the present thesis, three nickel base superalloys viz. Alloy 600, Alloy 690 and Alloy 693 have been investigated as candidate materials for the fabrication of waste storage tank. The general, pitting and intergranular corrosion behaviour of these alloys in the as-received condition have been discussed in this Chapter.

4.2 Experimental

- The corrosion assessment of the three nickel base superalloys in the as-received condition was made by using electrochemical impedance spectroscopy and potentiodynamic anodic polarization techniques in two different environments, 3 M HNO_3 and simulated HLW.

- The passive film composition of the alloys was analyzed using XPS, after electrochemically passivating the specimens in 3 M HNO_3 and simulated HLW.

- Pitting corrosion resistance of the alloys was evaluated in 3 M HNO_3 containing various concentrations of chloride ions from 500 to 3000 ppm at room temperature.

- Intergranular corrosion resistance of the nickel base superalloys was evaluated using Huey's test (ASTM A262 practice C) followed by microscopic examination.

4.3 Results and discussion

4.3.1 Microstructural analysis

The optical micrographs of as-received and electrolytically etched nickel base superalloys are represented in Fig. 4.1. All the alloys possessed austenitic structure with distinct grain boundaries. Figure 4.1(a) shows a typical γ phase matrix for as-received

Alloy 600. The average grain size of the alloy was about 70-80 μm. The average grain size of Alloy 690 was about 80-100 μm whereas for Alloy 693 it was about 20-30 μm. Figure 4.1(b) shows an austenitic phase matrix with twin boundaries and titanium nitride (TiN) precipitates for as-received Alloy 690. TiN appeared as golden color under optical microscope [11].

Figure 4.2 shows the surface morphology of the as-received Alloys 600, 690 and 693 observed under Scanning electron microscope (SEM). Figure 4.2a represents the surface morphology of the as-received Alloy 600. The precipitates of titanium rich particles, present on the surface were were confirmed by EDS. This blocky-shaped titanium rich titanium nitride is often observed in commercial Alloy 600 [2, 12, 13]. The grain boundaries were found to contain nickel and chromium rich precipitates.
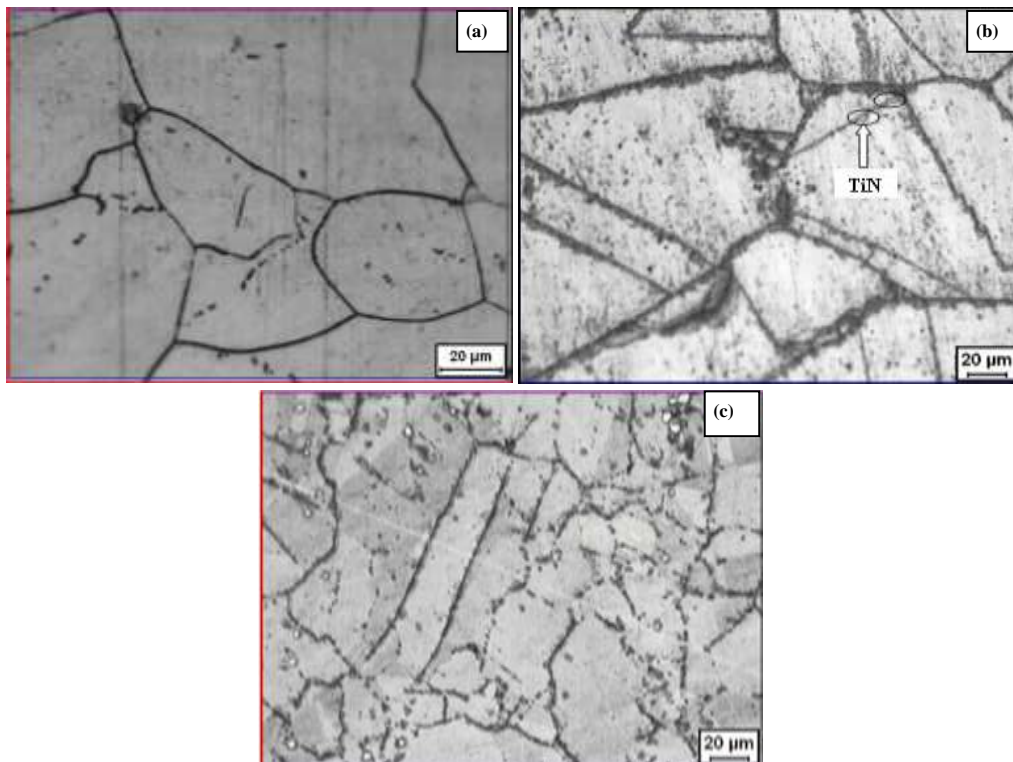
Fig. 4.1: Optical micrographs of as-received (a) Alloy 600, (b) Alloy 690 and

(c) Alloy 693

Figure 4.2b gives the surface morphology of Alloy 690. Two kinds of precipitates were observed in the specimen. Chromium rich precipitate formed along the grain boundary was confirmed by EDS. Ti rich precipitates found at regions adjacent to the grain boundaries, are shown in the magnified version (Fig 4.2b). The EDS of the precipitate confirmed it as TiN. The size of these precipitates were in the range 2-5 μm and were distributed randomly throughout the matrix.
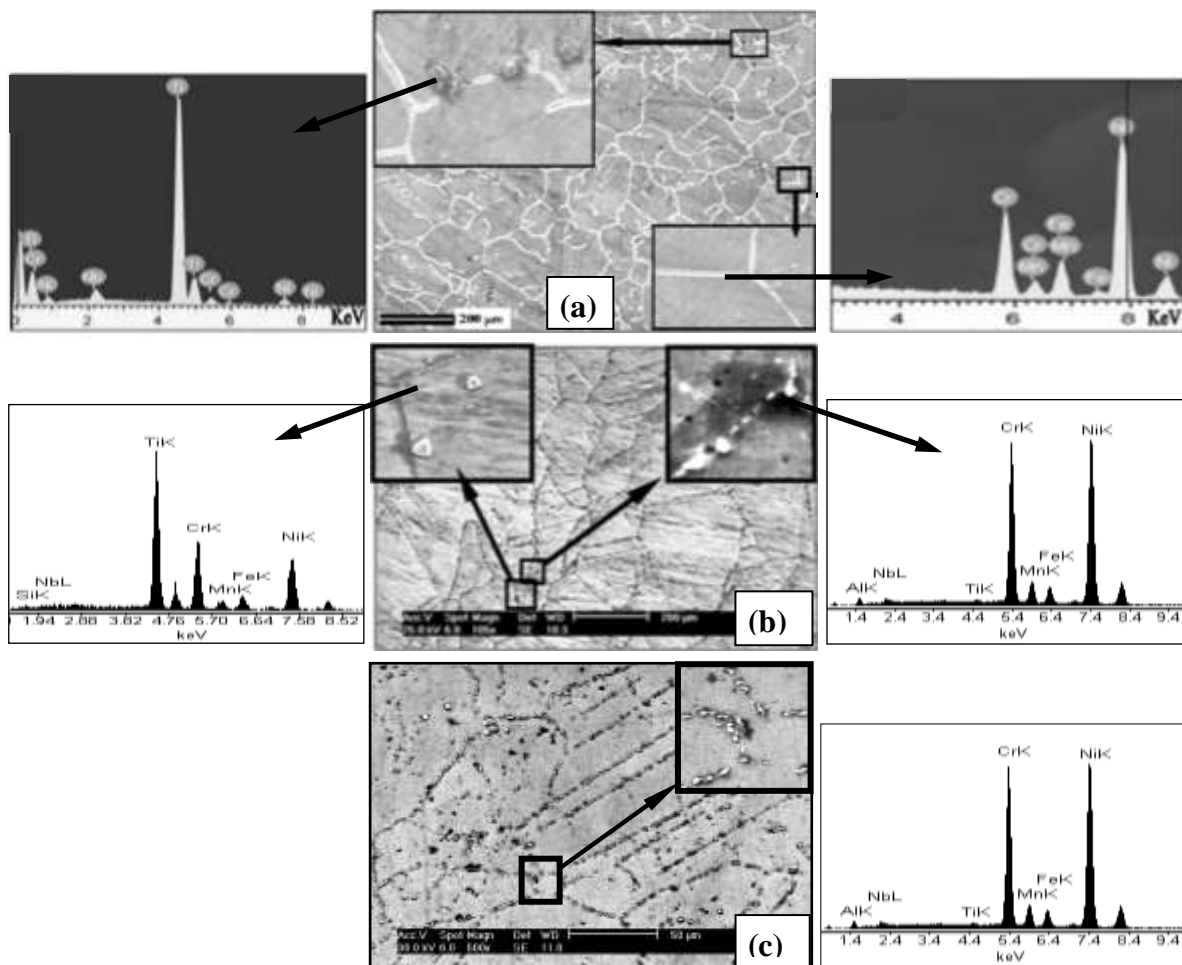
Fig. 4.2: SEM images of as-received (a) Alloy 600 (b) Alloy 690 and (c) Alloy 693

Figure 4.2c represents the surface morphology of Alloy 693 observed under SEM. Twin boundaries were not found in Alloy 693. Chromium rich precipitates found near and on the grain boundaries were confirmed by EDS analysis. The presence of 0.097% C and

high chromium had resulted in the precipitation along the grain boundaries and at the regions adjacent to the grain boundaries.

4.3.2 Electrochemical impedance spectroscopic analysis in 3 M HNO$_3$ and simulated HLW

The electrochemical impedance spectroscopic results of the nickel base superalloys obtained at the open circuit potential (OCP) in 3 M HNO$_3$ and simulated HLW medium, under as-received condition, are represented in Fig. 4.3 in the form of Nyquist plots, in which the imaginary impedance (Z'') is plotted against the real time impedance (Z'). It could be noticed from the plots that the impedance features were similar for all the three alloys in both the media, i.e. one depressed semicircle over the whole frequency range and all of them are characteristic of capacitive behaviour. The formation of such a semicircle arc is attributed to the charge transfer process at the electrode/electrolyte interface and it relates the changes in the passive oxide property to the chemical composition [14-16]. This indicates that there is one interfacial reaction process over the measured frequency range. However, a distinct difference was observed in all the impedance spectra in 3 M HNO$_3$ and in simulated HLW. The semicircle radius was smaller in simulated HLW compared to that in 3 M HNO$_3$ for all the three alloys. The larger semicircle radius in 3 M HNO$_3$ indicated a better passive film stability and hence, better corrosion resistance.

The experimental data from Fig. 4.3 are fitted in to the Randles circuit (given in Fig. 4.4) and the electrochemical parameters derived from the fitting are listed in Table 4.1. The circuit has the element arrangement of R$_S$ (CPE∥R$_P$), where R$_S$ is the solution resistance which depends on the resistivity of the solution, the electrode and cell geometry; [17], R$_P$ is the polarization resistance which represents the resistance of the passive film as a

result of its ionic conductivity and CPE is the constant phase element which corresponds to the capacitance parameter of the passive film due to its dielectric properties [18]. Replacing the capacitor by CPE is a common practice in the empirical EIS models [19].

It could be observed from Table 4.1 that all the alloys showed higher R_P value in 3 M HNO_3 compared to simulated HLW. The decrease in R_P could be attributed to increased ionic conductivity through the passive film or thinning of passive film, resulting in non-protective property [20]. Among the three alloys, highest R_P value was shown by Alloy 690 followed by Alloy 693 and Alloy 600. The R_P is the sum of the film resistance and the charge transfer resistance. The charge transfer processes take place at the metal/film or metal/electrolyte interface and control the rate of passive film growth on the specimens. The R_P values are strongly dependent on the passive film characteristics and are a measure of corrosion resistance.

Higher R_P value implies good corrosion resistance (e.g. slow rate of metal ion release and oxide growth). Low capacitance value of the passive film indicates long term stability of the passive film. [21-23]. Higher R_P value observed in Alloy 690 could be attributed to increased stability of the passive oxide layer due to the formation of enriched oxide of chromium or nickel or both. In contrast, the decreased R_P values for Alloy 693 and Alloy 600 specimens imply deterioration or reduction in the passive film stability. The variation in R_S could be attributed to a small difference between the specimen and reference electrode in the EIS measurement. The values of the CPE parameter are relatively lower in 3 M HNO_3 compared to simulated HLW for the alloys (Table 4.1). The CPE parameter is used to represent double layer capacitance of the film/electrolyte interface. Lower value of CPE indicated that the ion adsorption occurring at the surface of the specimens in 3 M HNO_3 is low, thereby confirming better corrosion resistance. Lower value of CPE also indicates the formation of thicker and more

protective passive film on the surface whereas higher value indicates non-homogeneous nature of film, which could be due to local defects weakening the passive film.
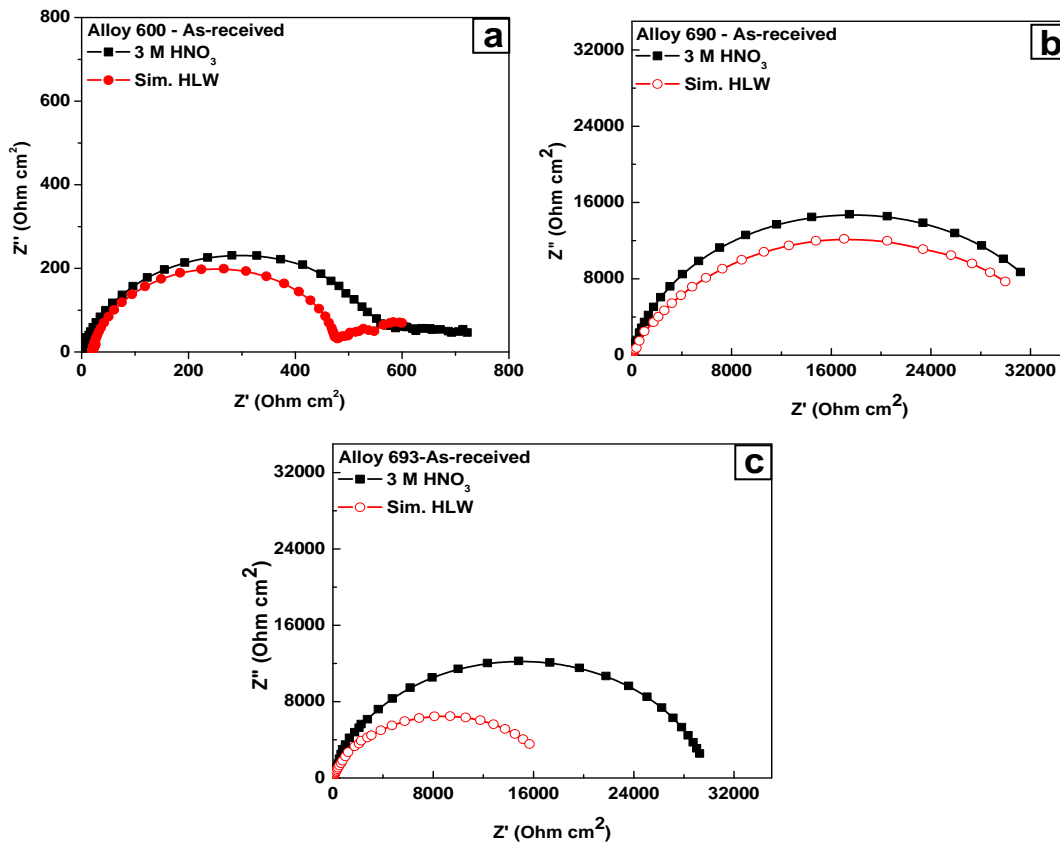
Fig. 4.3: Nyquist plot for as-received (a) Alloy 600, (b) Alloy 690 and (c) Alloy 693.
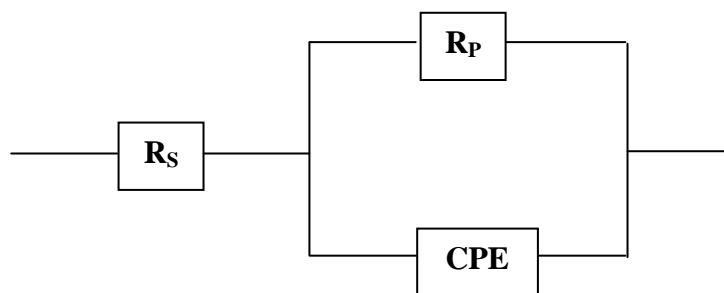
Fig. 4.4: Equivalent circuit used for EIS analysis

The values of n (Table 4.1), which gives the deviation of capacitance of the passive film from the ideal capacitive behaviour was in the range 0.75-0.9. These values indicate that the deviation from purely capacitive behaviour was relatively small for all the alloys in both the media.

Table 4.1 Electrochemical parameters derived from EIS curves

Material	Medium	R_s $(\Omega \, cm^2)$	R_p $(k\Omega \, cm^2)$	CPE $(Fcm^{-2}S^n)$	n
Alloy 600	3M HNO_3	2.17	0.124	33.1×10^{-6}	0.908
	Sim. HLW	1.90	0.100	37.5×10^{-6}	0.885
Alloy 690	3M HNO_3	2.02	35.4	42.2×10^{-6}	0.885
	Sim. HLW	0.45	35.4	57.9×10^{-6}	0.786
Alloy 693	3M HNO_3	0.75	30.0	34.0×10^{-6}	0.873
	Sim. HLW	1.30	18.5	52.1×10^{-6}	0.911

4.3.3 Potentiodynamic anodic polarization studies in 3 M HNO_3 and simulated HLW

The potentiodynamic anodic polarization curves obtained for the three as-received nickel base superalloys (Alloy 600, 690 and 693) in 3 M HNO_3 and simulated HLW at the solution temperatures of 25 and 50 ^{0}C are given in Fig. 4.5. Electrochemical parameters like corrosion potential (E_{corr}), passivation current density (I_{pass}), passive range and transpassive potential (E_{TP}) derived from the polarization curves are tabulated in Table 4.2. It could be seen from the Table that in 3 M HNO_3 at 25 ^{0}C, the potentiodynamic anodic polarization curve for Alloy 600 was characterized by an E_{corr} of 50 mV (SCE). The specimen passivated spontaneously after an initial active dissolution. The I_{pass} was found to be 160 $\mu A/cm^2$. The material was observed to be passive over a wide range of potential before transpassive dissolution occurred at 920 mV (SCE). In simulated HLW medium at 25 ^{0}C, the E_{corr} of as-received Alloy 600 was found to be higher than in 3 M

HNO_3. The I_{pass} of Alloy 600 in simulated HLW was found to be 170 $\mu A/cm^2$, which is marginally higher compared to 3 M HNO_3. When the solution temperature was increased to 50 ^0C in both 3 M HNO_3 and simulated HLW, an increase in E_{corr} as well as I_{pass} was observed. However, the potential for transpassive dissolution was similar to that at 25 ^0C. The potentiodynamic anodic polarization curves for Alloy 690 in 3 M HNO_3 at temperatures of 25 and 50 ^0C represented in Fig. 4.5b show that Alloy 690 is characterized by a corrosion potential of 140 mV (SCE) in 3 M HNO_3 at 25 ^0C. The specimen passivated spontaneously and maintained an I_{pass} of 1 $\mu A/cm^2$ (which is very low when compared to Alloy 600) without exhibiting the active to passive transition peak. The material was found to be passive over a wide range of potential (680 mV (SCE)) before transpassive dissolution occurred at 910 mV (SCE). When the temperature of nitric acid solution was increased to 50 ^0C, the E_{corr} increased to 420 mV (SCE) and the I_{pass} increased to 3 $\mu A/cm^2$ and the E_{TP} decreased to 875 mV (SCE). In simulated HLW at 25 ^0C, the E_{corr} of Alloy 690 was found to be higher than in 3 M HNO_3. Though there was an increase in I_{pass} in simulated HLW compared to 3 M HNO_3, still it was in the lower range (2 $\mu A/cm^2$). At 50 ^0C, the E_{corr} further increased and a substantial increase in the I_{pass} (8 $\mu A/cm^2$) could be observed in simulated HLW.

The potentiodynamic anodic polarization curves for Alloy 693 in 3M HNO_3 and simulated HLW for the temperatures 25 and 50 ^0C are reproduced in Fig. 4.5c. This material showed similar corrosion behaviour as that of Alloy 690, passivated spontaneously in both 3 M HNO_3 and simulated HLW with low I_{pass} and without active to passive transition. The material also exhibited high E_{TP} and long passive range in both 3 M HNO_3 and simulated HLW. However, Alloy 693 was found to possess marginally higher I_{pass} than Alloy 690 under all the conditions studied.

The increase in E_{corr} observed for all the three as-received specimens with increase in temperature from 25 ^{0}C to 50 ^{0}C in 3 M HNO_3 as well as simulated HLW could be attributed to the enhanced autocatalytic reduction of nitric acid [24-32]. Nitric acid is indirectly reduced by an autocatalytic mechanism to generate the electroactive species, nitrous acid, the amount of which increases at higher temperatures and in high concentrations of nitric acid. But at concentrations as low as 3 M nitric acid used in this study, nitrous acid doesn't accumulate, rather completely reduces to nitric oxide (NO). Electrochemical studies carried out on the reduction of nitric acid revealed that the final reduction product of nitric acid is NO depending on the process conditions and at concentrations below 8 M nitric acid [24, 31]. HNO_2 is further regenerated at the electrode according to a heterogeneous chemical reaction involving NO and HNO_3 [24, 28-30]. The reduction is thus, autocatalytic as the oxidant is generated at a geometrically increasing rate, which catalyses the reduction process. The autocatalytic mechanism of reduction prevailing in the nitric acid concentration involved in the present study has been discussed in the literature [24-34];

$$HNO_3 \longleftrightarrow H^+ + NO_3^- \tag{4.1}$$

$$NO_3^- + 3H^+ + 2e^- \longleftrightarrow HNO_2 + H_2O \ (E_{25\,^oC} = 934 \ mV/ \ SHE) \tag{4.2}$$

$$HNO_2 + H^+ + e^- + s \longleftrightarrow (NO)_{ads} + H_2O \tag{4.3}$$

$$HNO_3 + (NO)_{ads} \longleftrightarrow (HNO_2)_{el} + (NO_2)_{ads} \tag{4.4}$$
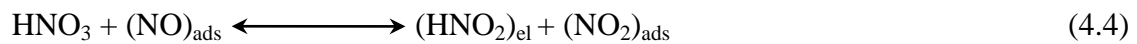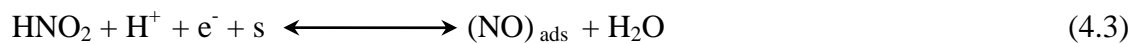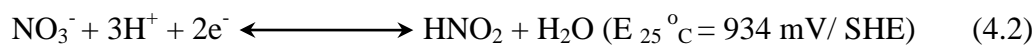
Further reaction occurs between nitric acid and nitrous acid, to produce nitrogen dioxide (NO_2).

$$HNO_3 + (HNO_2)_{el} + 2s \longleftrightarrow 2(NO_2)_{ads} + H_2O \tag{4.5}$$

$$(NO)_{ads} \longleftrightarrow NO \ (g) + s \tag{4.6}$$

$$(HNO_2)_{el} \longleftrightarrow (HNO_2)_{sol} \tag{4.7}$$
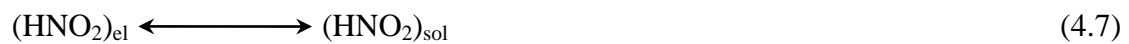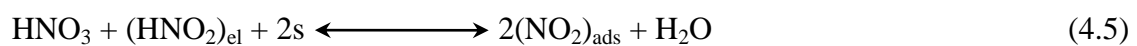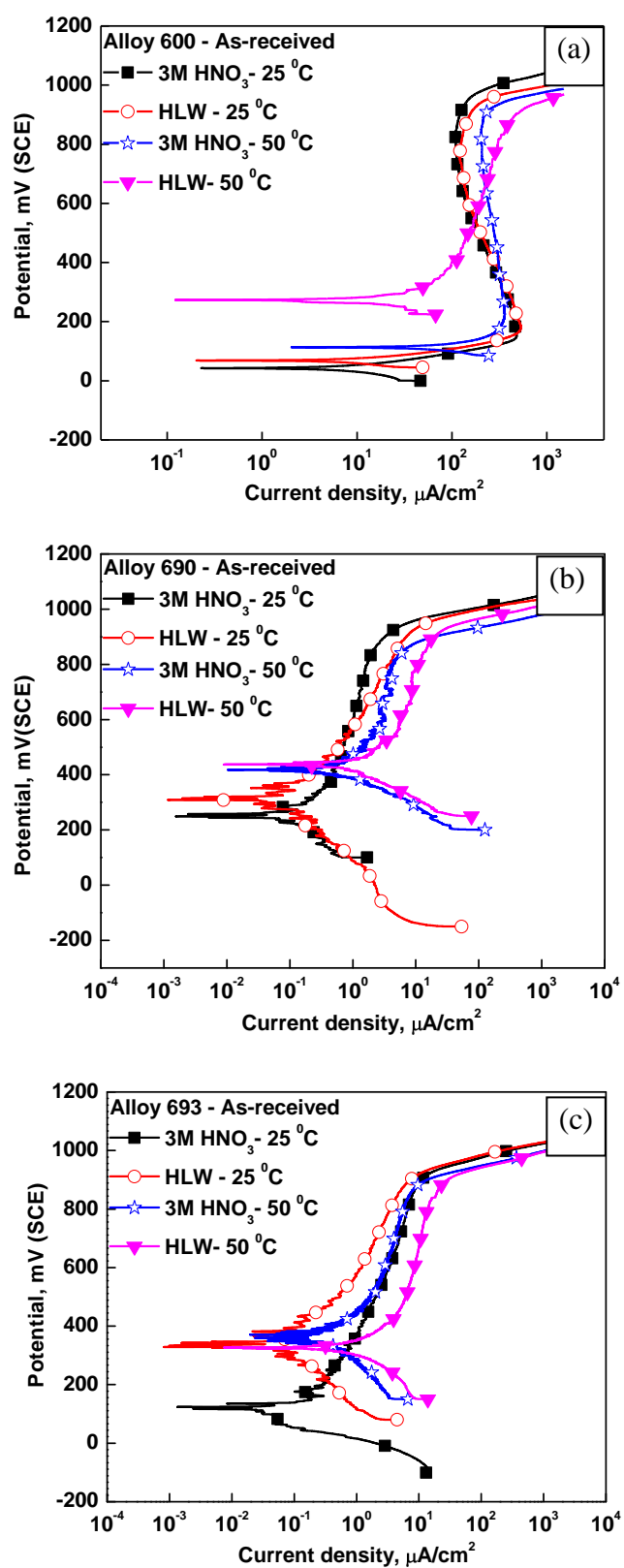
Fig. 4.5: Potentiodynamic anodic polarization curves of as-received specimens (a) Alloy 600, (b) Alloy 690 and (c) Alloy 693.

$(NO)_{ads}$ represents the NO adsorbed on the surface of electrode. $(HNO_2)_{el}$ and $(HNO_2)_{sol}$ represent the nitrous acid concentration at the electrode and solution respectively and 's' represents a free adsorption site at the electrode surface. Nitrogen dioxide, the product formed in Eqs 4.4 and 4.5, being unstable below the concentration of 8 M nitric acid, gets consumed to regenerate acid, which means the reverse reaction is favourable.

The reduction product, HNO_2 plays an ambivalent role in the nitric acid media. From thermodynamic point of view, it is the reduced species of nitric acid. Higher the HNO_2 concentration, more reducing the medium is, which in turn increases the redox potential of the medium. From kinetic point of view, it increases the reduction rate of nitric acid by autocatalytic mechanism. The formation of reduction products of nitric acid such as nitrous acid and nitric oxide, which catalyze the reduction process is accelerated with increase in temperature. This leads to an increase in current density and the cathodic curve shifts towards higher potential which in turn shifts the corrosion potential towards noble direction.

In simulated HLW, the E_{corr} is further ennobled as compared to 3 M HNO_3 for all the alloys. This could be attributed to the presence of several cations present in simulated HLW solution, which are available for reduction. The presence of oxidizing ions such as Fe(III), Cr(VI) etc, catalyses the nitrate reduction [28, 30, 33]. In the autocatalytic reduction process of nitric acid, NO, formed as a product, acts as a reductant. This reduces the cations (Fe^{3+}, Cr^{6+} etc.) present in the simulated HLW, which in turn catalyze further reduction of HNO_3 and thus, shifts the E_{corr} to noble direction [28]. The net reduction due to presence of many cations depends upon the relative aggressiveness of ions. More the oxidizing species, rapidly it will be reduced by NO [33]. It has been reported by Armstrong et al. [33] that the presence of NO could lead to the reduction of these cations and thus increasing the reduction rates.
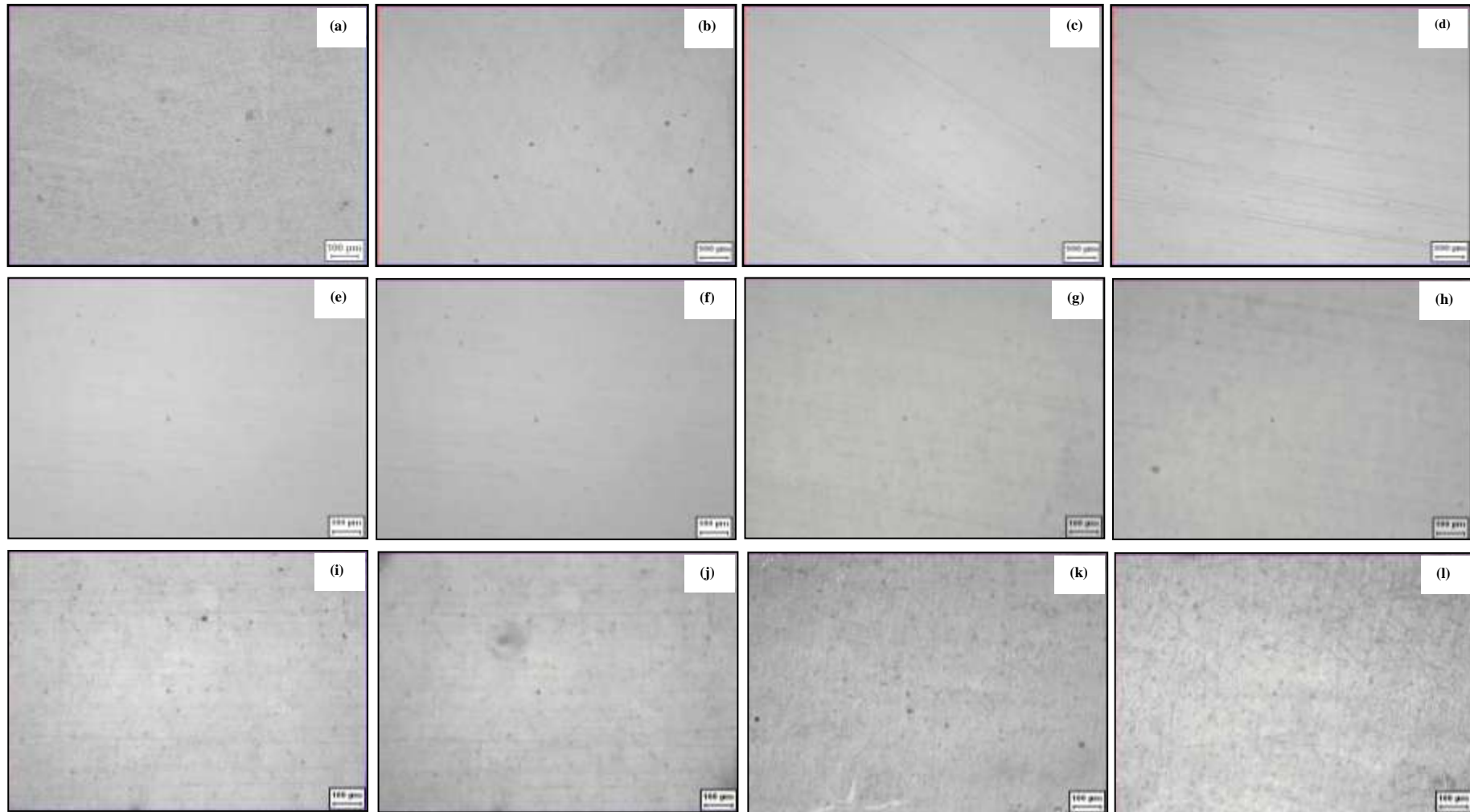
Fig. 4.6: Optical micrographs after polarization experiments: Alloy 600 in (a) 3 M HNO_3 at 25 ^{0}C, (b) Sim. HLW at 25 ^{0}C, (c) 3 M HNO_3 at 50 ^{0}C, (d) Sim. HLW at 50 ^{0}C; Alloy 690 in (e) 3 M HNO_3 at 25 ^{0}C, (f) Sim. HLW at 25 ^{0}C, (g) 3 M HNO_3 at 50 ^{0}C, (h) Sim. HLW at 50 ^{0}C and Alloy 693 in (i) 3 M HNO_3 at 25 ^{0}C, (j) Sim. HLW at 25 ^{0}C, (k) 3 M HNO_3 at 50 ^{0}C and (l) Sim. HLW at 50 ^{0}C

Increasing the temperature increases the reduction rate and the cathodic part of the current-potential curve shifts towards higher potentials; consequently, the E_{corr} of the alloy increases. Increase in temperature also favours the transformation of the stable, insoluble chromium (III) oxide (Cr_2O_3) to soluble chromium (VI) oxide ($Cr_2O_7^{2-}$). The oxide film thus, becomes unstable leading to its dissolution and thereby increasing the I_{pass}.

In the present investigation, Alloy 690 was found to show better corrosion resistance compared to Alloy 693 followed by Alloy 600.

Optical microscopic examination of the specimens after polarization studies, revealed that the Alloys 600 and 693 were attacked on the surface after transpassive dissolution (Fig. 4.6) which could be due to the presence of precipitates (Fig. 4.2) whereas no attack was observed on Alloy 690 specimens at all conditions. In the Alloy 693, the attack was found along the grain boundaries.

Table 4.2 Electrochemical parameters derived from polarization curves

Material	Medium	25 ^{0}C				50 ^{0}C			
		E_{corr}	I_{pass}	Pass. Range	E_{TP}	E_{corr}	I_{pass}	Pass. Range	E_{TP}
Alloy 600	3M HNO$_3$	47	164	756	920	114	246	716	910
	HLW	68	170	710	900	298	206	530	890
Alloy 690	3M HNO$_3$	140	1	679	907	420	3	389	875
	HLW	329	2	491	930	438	8	413	916
Alloy 693	3M HNO$_3$	107	2.9	690	920	366	4	428	885
	HLW	376	2	467	930	328	9	501	903

All potentials and current densities are in mV(SCE) and µA/cm^2 respectively.

4.3.4 X-ray photoelectron spectroscopic study

After potentiostatic polarization of the nickel base specimens in both 3 M HNO_3 and in simulated HLW, the specimens were subjected to X-ray photoelectron spectral analysis. Potentials at which the electrochemical passivations were carried out are reported in Table 4.3. All the spectra were recorded after the sputtering time of 30 s, for the purpose of removing the adventitious hydrocarbon layer present over the surface of the unsputtered specimens.

Table 4.3 Potentials applied for electrochemical passivation

Material	Passivation Potential, mV (SCE)	
	3 M HNO_3	**Sim. HLW**
Alloy 600	590	490
Alloy 690	590	680
Alloy 693	590	720

<u>Alloy 600</u>

High resolution spectra were recorded for Ni 2p3/2, Cr 2p and O 1s electrons for Alloy 600 in 3 M HNO_3 as well as simulated HLW. The specimen that was passivated in 3 M HNO_3, region showed two peaks in the high resolution spectrum of the Cr 2p3/2 indicating the presence of oxides at the binding energy of 576.3 eV and elemental chromium at 574.0 eV (Fig. 4.7a). The high resolution spectrum of the Ni $2p_{3/2}$ region composed of a single peak at the binding energy of 852.6 eV corresponding to the metallic state on the surface (Fig. 4.7c). The high resolution spectrum of the O 1s region showed two peaks at the binding energies 530.2 and 531.1 eV corresponding to chromium(VI) oxide and chromium (III) oxide

respectively (Fig. 4.7e). After sputtering the Cr 2p region for 3 minutes, the intensity of the peak corresponding to the metallic state was found to increase whereas that of the oxide state decreased.

For the specimen that was passivated in simulated HLW, the high resolution spectrum of the Cr 2p3/2 region showed two peaks indicating the presence of oxides at the binding energy of 576.2 eV and elemental Cr at 573.9 eV (Fig. 4.7b). The high resolution spectrum of the Ni $2p_{3/2}$ region composed of a single peak at the binding energy of 852.6 eV corresponding to the metallic state on the surface (Fig. 4.7d). The high resolution spectrum of the O 1s region showed two peaks at the binding energies 530.1 and 531.1 eV corresponding to chromium (VI) oxide and chromium (III) oxide respectively (Fig. 4.7f). After sputtering the Cr 2p region for 3 minutes, the intensity of the peak of the metallic state was observed to increase whereas that of the oxide state decreased.

The XPS studies confirmed that the surface films of the specimens in both the electrolytes are composed of mixed oxides of chromium i.e. chromium trioxide and chromium (III) oxide. It was apparent that Alloy 600 developed thicker surface oxide film when passivated in simulated HLW containing different types of cations than that which was passivated in 3 M HNO_3. The high resolution spectra of Cr 2p region of both the specimens at different sputter depths validated this observation. Both the specimens showed almost the same concentration of elemental chromium after 30 sec sputter depth, but, at the depth of 3 min sputtering, the concentration of elemental chromium in the specimen passivated in 3 M HNO_3 (Fig. 4.8) is much higher than that in the other specimen. The overall intensity of chromium in both the metallic and oxide states was also less in the former case.

Alloy 690

The survery spectra of Alloy 690, showed the presence of Ni, Cr, Mn, Fe and N in 3 M HNO_3 as well as simulated HLW. The XPS spectra of Ni $2p_{3/2}$, Cr $2p_{3/2}$ and Fe $2p_{3/2}$ electrons for the specimen passivated in 3 M HNO_3,were composed of two peaks corresponding to the predominantly oxidized state in the surface films and the metallic state in the underlying oxide film. The peak binding energies of the Ni $2p_{3/2}$ electrons at 852.7, 854.2 and 859.0 eV corresponded to elemental Ni, NiO and Ni_2O_3 respectively (Fig. 4.9a). Similarly the high resolution scans for the Cr $2p_{3/2}$ region showed the presence of Cr_2O_3 at 576.6 eV and elemental Cr at 574.1 eV (Fig. 4.9c) and for the Fe $2p_{3/2}$ electrons the peak binding energies at 712.2 and 707.5 eV corresponded to Fe_2O_3 and metallic Fe respectively (Fig. 4.9e). For O 1s, the peak positions at 530.6, 531.7 and 531.9 eV matched well with the metal oxides of Ni, Cr and Fe (Fig. 4.9g). After sputtering for 3 minutes, the area under the peak for the metallic state started to build up.

High resolution spectra were recorded for Ni $2p_{3/2}$, Cr $2p_{3/2}$ and Fe $2p_{3/2}$ electrons for the specimen passivated in simulated HLW. The spectra revealed the presence of oxidized film at the surface followed by metallic state underneath the oxide film. The peak binding energies of Ni $2p_{3/2}$ electrons at 852.7, 854.0 and 858.9 eV corresponded to elemental Ni, NiO and Ni_2O_3 respectively. Similarly the high resolution scans for the Cr $2p_{3/2}$ region showed the presence of Cr_2O_3 at 576.6 eV and elemental Cr at 574.1 eV and for the Fe $2p_{3/2}$ electrons the peak binding energies at 712.3 and 707.1 eV corresponded to Fe_2O_3 and metallic Fe respectively. For O 1s, the peak positions at 530.5, 531.5 and 531.9 eV matched well with the metal oxides of Ni, Cr and Fe. Similar to the behaviour exhibited by Alloy 690 inn 3 M HNO_3, the area under the peak for the metallic state was observed to build up when
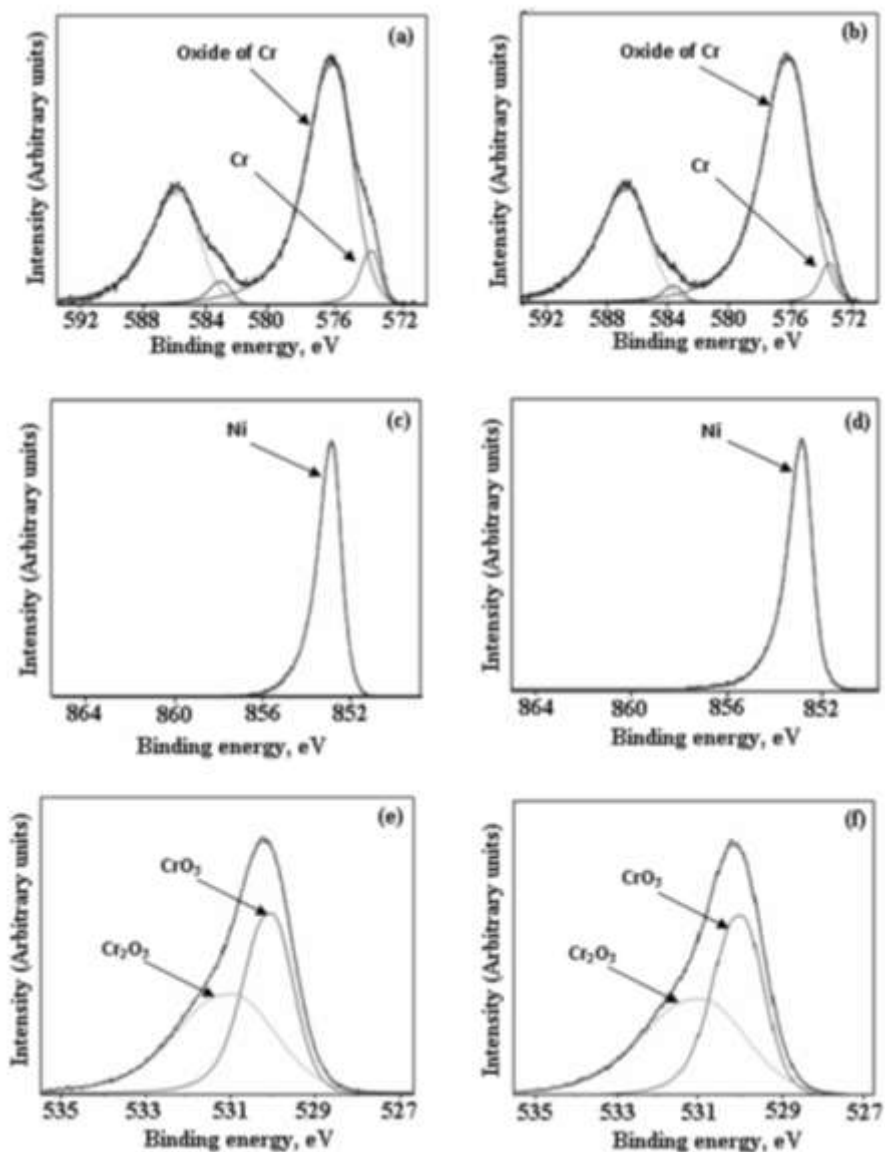
Fig. 4.7: XPS profile of Alloy 600 in 3 M HNO$_3$ & Sim. HLW: (a) & (b) for Cr 2p$_{3/2}$, (c) & (d) for Ni 2p$_{3/2}$, (e) & (f) for O 1s respectively.
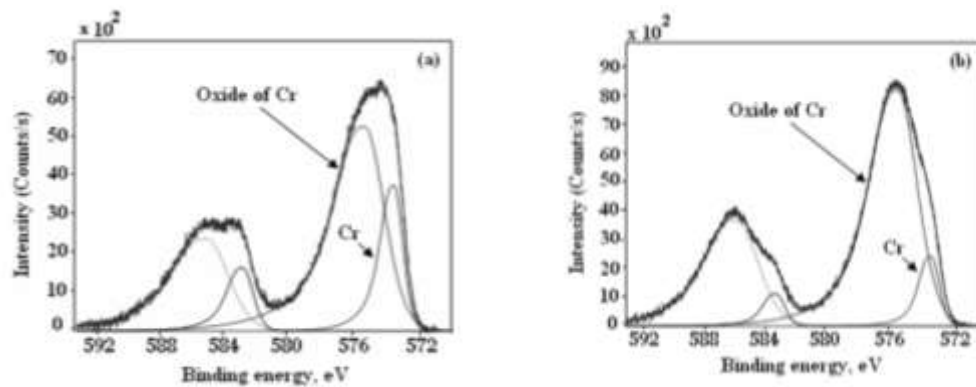
Fig. 4.8: XPS profile of Cr 2p$_{3/2}$ after 3 min. of sputtering in (a) 3 M HNO$_3$, (b) Sim. HLW.
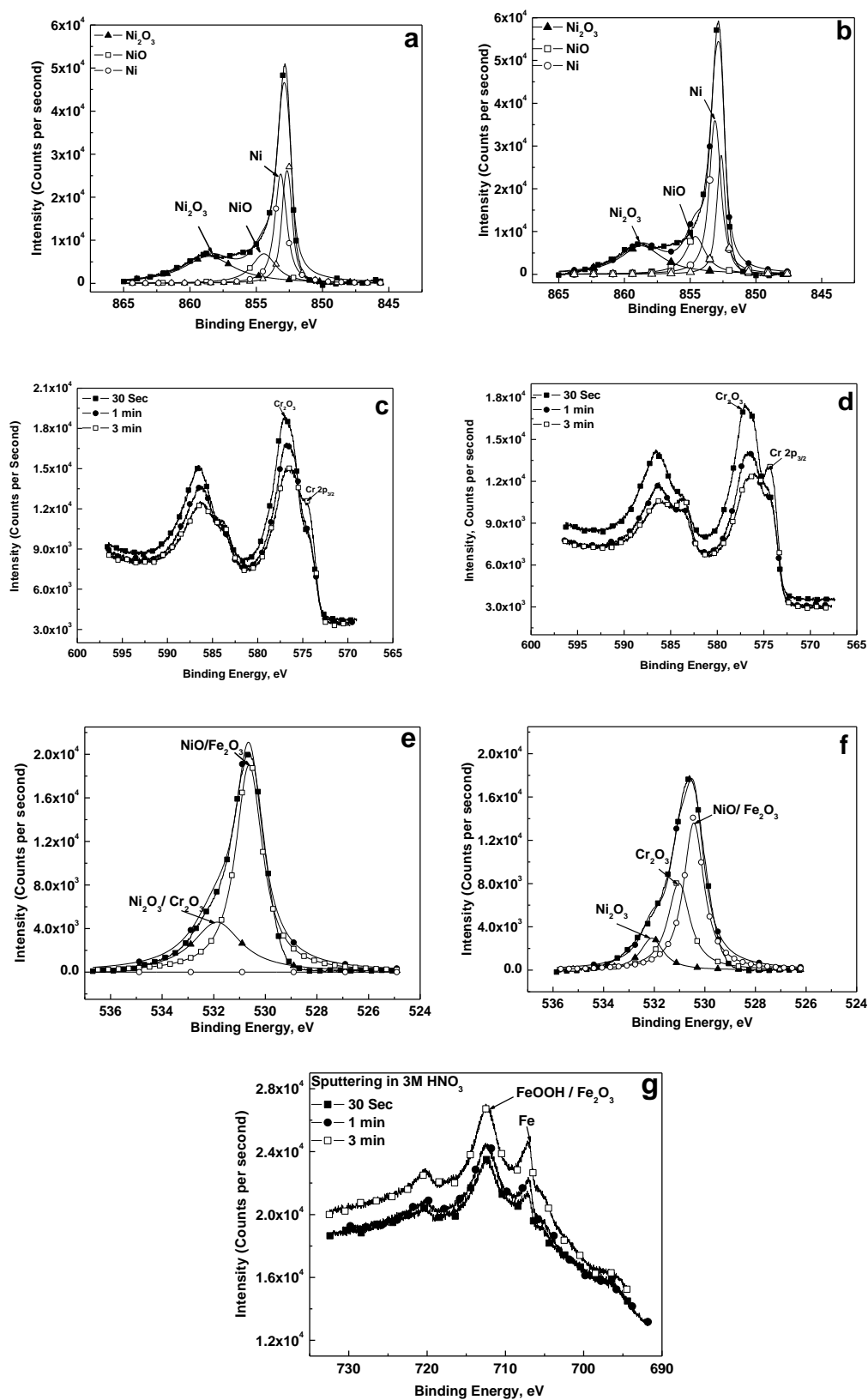
Fig. 4.9: XPS profile of Alloy 690 in 3 M HNO$_3$ & Sim. HLW: (a) & (b) for Cr 2p$_{3/2}$, (c) & (d) for Ni 2p$_{3/2}$, (e) & (f) for O 1s and (g) for Fe 2p$_{3/2}$.
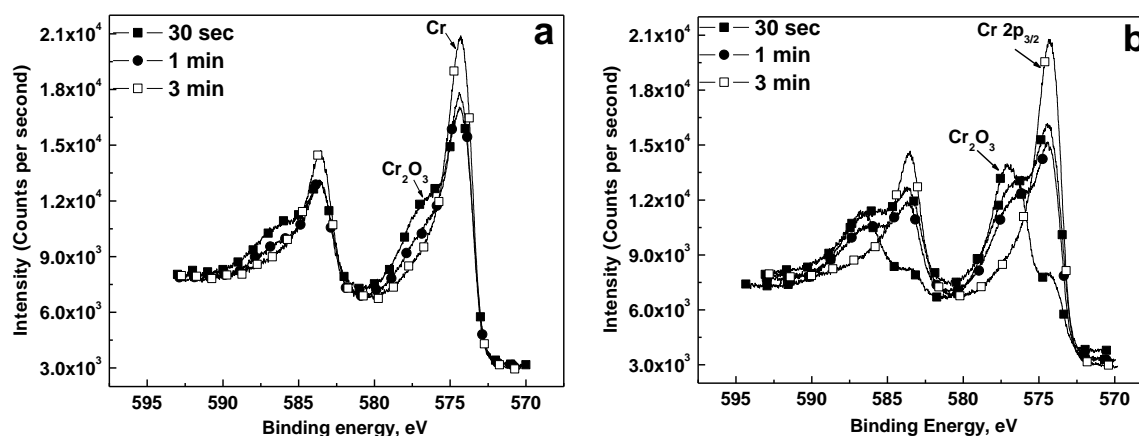
Fig. 4.10: XPS profile of Alloy 693 in 3 M HNO$_3$ & Sim. HLW: (a) & (b) for Cr 2p$_{3/2}$

sputtered for 3 minutes. Thus, the surface film for both the specimens is composed of a mixed oxide of Ni$_2$O$_3$-NiO-Cr$_2$O$_3$-Fe$_2$O$_3$. However, a noticeable difference observed in the two Alloy 690 specimens passivated in different media is that better surface oxide film developed when passivated in 3 M HNO$_3$ than that which was passivated in simulated HLW containing different types of cations. This is also supported by the fact that the area under the peak corresponding to the oxidized state was more for the specimen passivated in 3 M HNO$_3$ than for the specimen passivated in simulated HLW.

Alloy 693

High-resolution spectra were acquired for the Ni 2p$_{3/2}$, Cr 2p$_{3/2}$ and Fe 2p$_{3/2}$ electrons after 30 s of sputtering for the alloy 693 specimen passivated in 3 M HNO$_3$. The spectrum showed a thin oxide layer of Cr, Ni and Fe similar to that obtained for Alloy 690. The area under the peak for the oxide and the metallic peak below the oxide surface film were comparable. Metallic peak was predominantly seen after sputtering for 3 minutes. High-resolution spectra were also acquired for the Ni 2p$_{3/2}$, Cr 2p$_{3/2}$ and Fe 2p$_{3/2}$ electrons after 30 s of sputtering for

the specimen polarized in simulated HLW. Unlike the previous case, it was found that the specimen had developed a better oxidized layer when passivated in simulated HLW than that in 3 M HNO_3 as the area under the peak corresponding to the oxidized state was more in the former case than that the latter. This observation upholds the polarization data which showed the anodic current density as 2.9 $\mu A/cm^2$ for Alloy 693 polarized in 3 M HNO_3 and 2 $\mu A/cm^2$ for the same polarized in simulated HLW. It is also found that between Alloy 690 and 693, the former gives a better oxide film compared to the latter.

4.3.5 Pitting corrosion study

The pitting corrosion resistance of the nickel base superalloys under as-received condition were evaluated using potentiodynamic anodic polarization technique in 3 M HNO_3 containing different concentrations of chloride ions (500, 1000, 2000 and 3000 ppm) at 25 ^{0}C. The corresponding polarization curves are represented in Fig.4.11. The electrochemical parameters viz. corrosion potential, passivation current density and pitting potential, obtained from various polarization curves are listed in Table 4.4.

The as-received Alloy 600 showed a negative corrosion potential followed by a critical current peak during active dissolution (Fig. 4.11). The initial active dissolution was followed by a passive region which extended until oxygen evolution and then breakdown where an abrupt increase in current was recorded. The breakdown of passive film depends upon the electrode potential, environment and inhomogeneities at the surface and it results in either pitting or transpassive dissolution. For Alloy 600, the I_{pass} was found to be 5 $\mu A/cm^2$ at 500 ppm chloride ion concentration. Further increase in chloride ion concentration caused a decrease in the E_{corr} and an increase in the I_{pass}. Increase in peak current density was also

observed in the active region with increase in chloride ion concentration. Pitting may occur during active dissolution, if specific regions of the specimen are more susceptible to corrosion and dissolve faster than the rest of surface.

For the Alloys 690 and 693 in as-received condition, in 3 M HNO_3 medium containing 500 ppm chloride ions, the E_{corr} found at about 150 mV (SCE), decreased further with increase in chloride ion concentration. Unlike Alloy 600, no active-passive transition was observed for the as-received Alloys 690 and 693. Both these alloys passivated spontaneously without any active dissolution at all concentrations of chloride ions. The spontaneous passivation is attributed to the autocatalytic reduction of nitric acid, a mechanism which has been discussed in Section 4.3.3. The I_{pass} found in the range of 1-2 $\mu A/cm^2$ with 500 ppm chloride ion concentration for both the alloys is quite low. Similar to Alloy 600, the E_{corr} was found to decrease and I_{pass} increased with increase in chloride ion concentration. Unlike Alloy 600, the increase in I_{pass} was insignificant even with 3000 ppm chloride ion concentration and was found to be less than 5 $\mu A/cm^2$.

A decrease in OCP was observed with increase in chloride ion concentration. This is due to the fact that chloride addition promotes anodic reaction and retards the cathodic reaction, which in turn reduces the OCP [34]. Inhibition of the cathodic reaction was a result of chloride adsorption on the surface that prevents the reduction of nitric acid to nitrous acid. According to Kolman et al. [29], during active corrosion, the increase in anodic kinetics is greater than the increase in cathodic kinetics, resulting in the decrease in OCP.
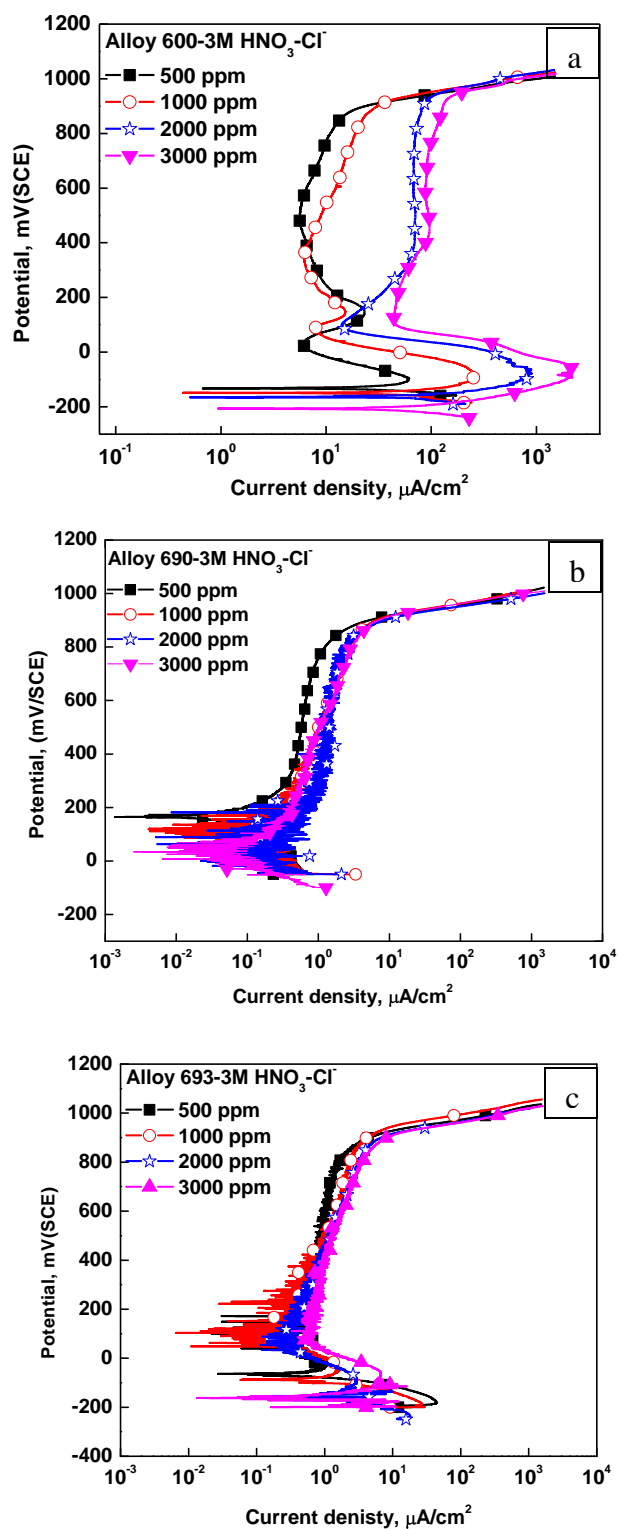
Fig. 4.11: Potentiodynamic polarization behaviour in acidic chloride medium: (a) Alloy 600, (b) Alloy 690 and (c) Alloy 693

Table 4.4: Electrochemical parameters obtained from pitting corrosion study

Material	Chloride ion Conc. (ppm)	E_{corr}	I_{pass}	E_{pit}
Alloy 600	500	-130	5.6	890
	1000	-145	8.9	870
	2000	-165	69.5	870
	3000	-200	94.2	870
Alloy 690	500	170	0.7	935
	1000	120	1.1	940
	2000	90	1.3	940
	3000	35	1.25	935
Alloy 693	500	100	0.8	950
	1000	100	0.9	970
	2000	55	1.2	930
	3000	50	1.3	935

*All potentials and current densities are in mV(SCE) and µA/cm^2 respectively.

The E_{corr} reduced with the addition of chloride ions for all the alloys. With increase in chloride ion concentration, more chloride ions get adsorbed on the surface of the specimen and shift the E_{corr} to negative values. The shift in E_{corr} towards negative direction in chloride containing solutions indicates that the working electrode becomes electrochemically unstable and is susceptible to anodic corrosion. Increase in chloride ion concentration, promotes the active dissolution and hence, a larger overpotential is required for passivation, which leads to larger peak current density.

With increase in chloride ion concentration, the I_{pass} increased substantially for Alloy 600 and marginally for Alloy 690 and Alloy 693. The increase in I_{pass} is associated with increase in anodic dissolution. Higher value of I_{pass} could be attributed to the less stable and less

protective nature of the passive film. The chloride ions tend to adsorb on the oxide film formed on the surface of the specimen leading to enhanced dissolution of the oxide film, which in turn increases the passivation current density.
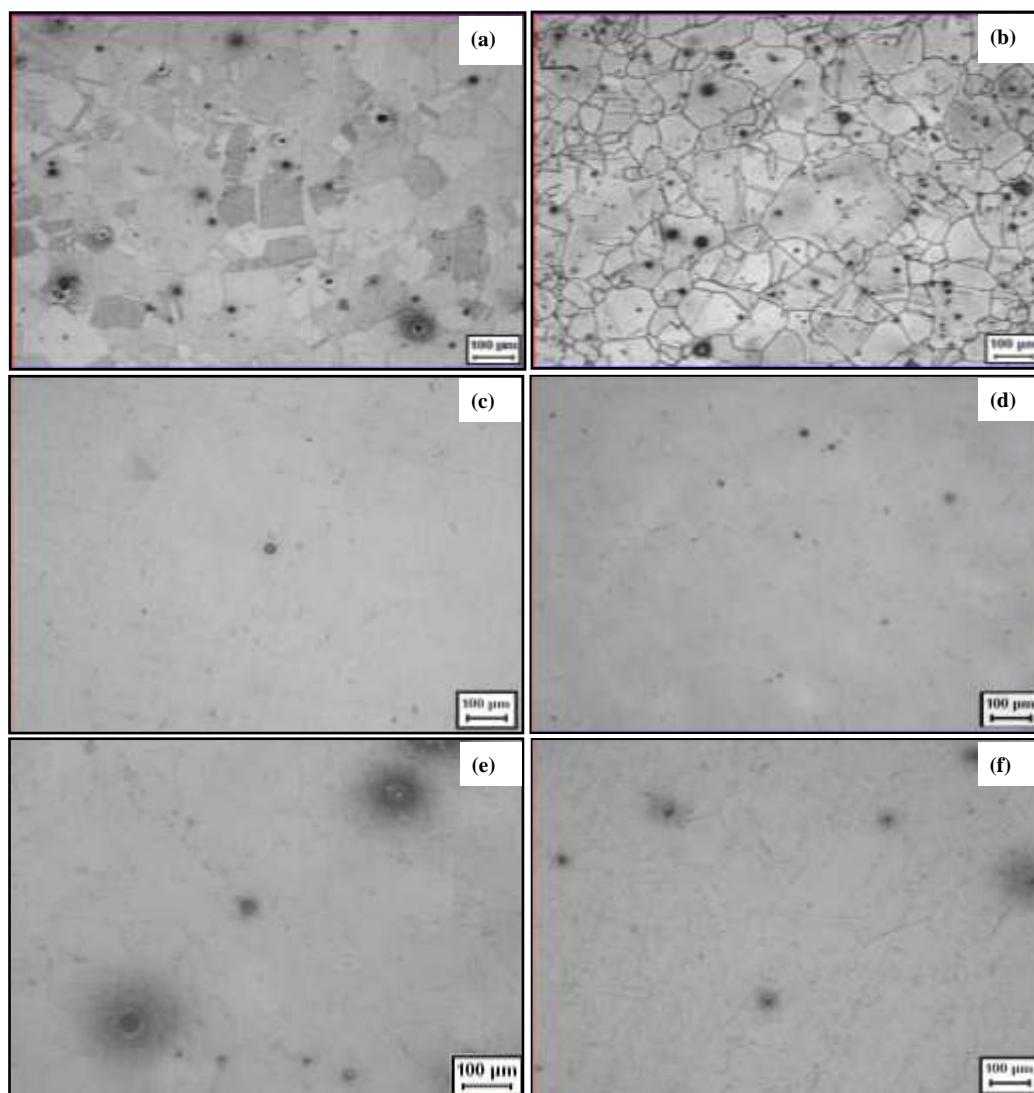
Fig. 4.12: Optical micrographs after pitting corrosion in acidic-chloride medium: (a) Alloy 600 with 500 ppm, (b) Alloy 600 with 3000 ppm, (c) Alloy 690 with 500 ppm, (d) Alloy 690 with 3000 ppm, (e) Alloy 693 with 500 ppm and (f) Alloy 693 with 3000 ppm chloride ion concentration.

Many authors [29, 35, 36] have investigated the corrosion behaviour of different materials in electrolytes containing nitrate and chloride both, and reported that nitrate ion effectively inhibit pit initiation in halide solutions. Green et al. [37] have reported that nitrate ions effectively prevent pit initiation in chloride solutions, but accelerates pit growth when the nitric acid was added after pit initiation. According to Newman et al. [38], nitrate ion has no inhibition effect on the active dissolution, however it passes through the salt film formed at higher potentials during diffusion controlled dissolution, causing abrupt passivation of an electrode surface. According to Ma et al. [39] the pitting inhibition of nitrate ion strongly depends on the pH of the solution. The decrease in pH is advantageous for promoting the passivation action of nitrate ions.

In the present investigation, the E_{pit} values were found to be high and remain in close proximity, with increase in chloride concentration from 500 to 3000 ppm for all the alloys. Presence of precipitates like titanium nitride may behave as weak points in the oxide layer and become initiation sites for pitting corrosion. Pits of size ranging from submicron to micron were observed on the specimens and their size and population generally increased with increase in concentration of chloride ions (Fig. 4.12). However, with a few micropits even in 3000 ppm chloride ion concentration, Alloy 690 exhibited superior pitting corrosion resistance in nitric acid-chloride medium, compared to Alloy 600 and 693. The size and population of pits in Alloy 600 were large and the attack was severe with exposed grain boundaries at 3000 ppm chloride ion concentration.

The difference in pitting corrosion behaviour of Alloy 600, 690 and 693 could be attributed to the differences in their chemical composition. Alloying composition and microstructure play a significant role in affecting the pitting corrosion resistance of the passive film and

hence the tendency to pit. The concentration of chromium plays a dominant role in conferring passivity as its presence in any alloy is responsible for the formation of the corrosion-resistant oxide film. The inferior pitting corrosion resistance of Alloy 600 could be attributed to the lower percentage (nearly 15%) of Cr whereas it is almost double in the case of Alloy 690 and Alloy 693. The higher concentration of manganese and sulphur may also lead to more pitting in Alloy 600. The inferior pitting corrosion resistance of Alloy 693 compared to Alloy 690 could be attributed to the higher percentages of carbon (0.097%), which resulted in carbide precipitation that provides sites prone to pitting corrosion [40].

4.3.6 Intergranular corrosion study

The intergranular corrosion resistance of the three nickel base superalloys in as-received condition were evaluated by Huey test (ASTM 202A, practice C) [41, 42] in which the specimens were immersed in 65% boiling nitric acid for five periods with durations of 48 h for each period. The weight loss was measured after each period of testing and corrosion rate was calculated using the following formula;

Rate of corrosion = (3,440,880 x W) / (A x t x d) mils per year   (4.8)

where W = Weight loss in g,

       A = Surface area of the specimen in cm^2,

       t = Time of exposure in h,

       d = Density of the specimen in g/cm^3.
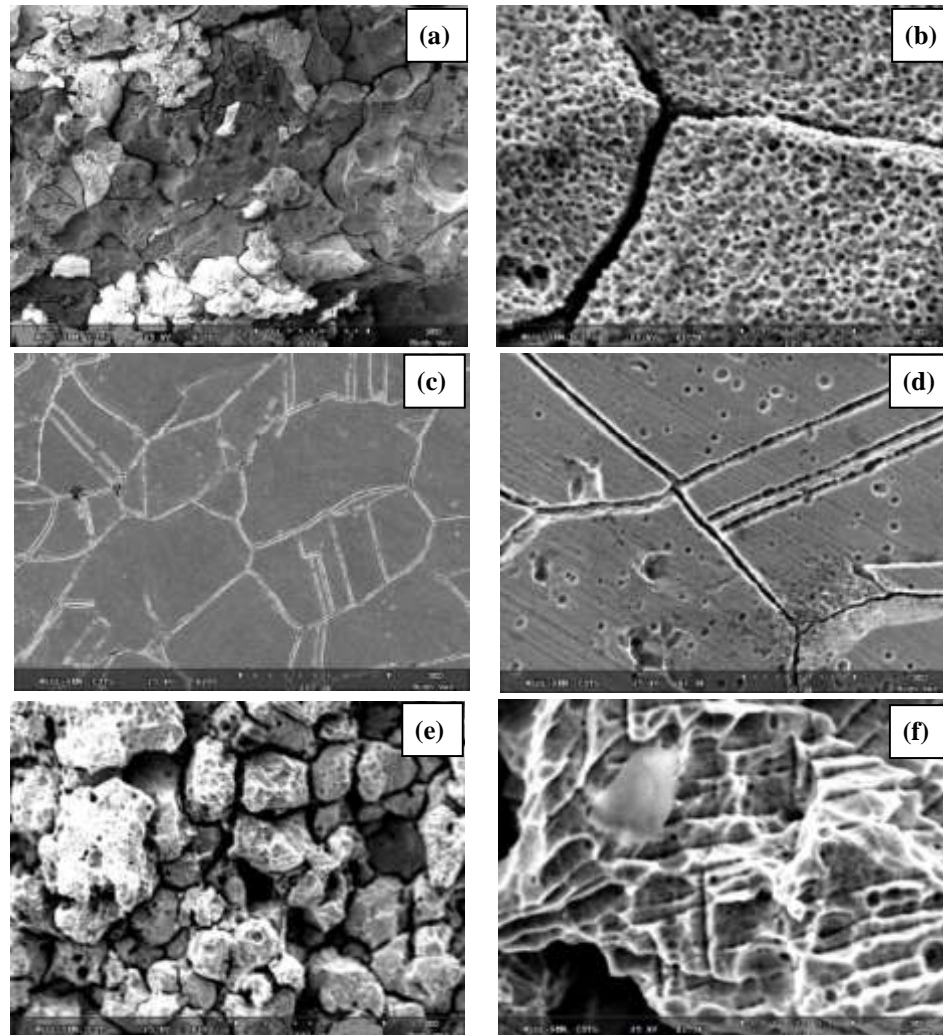
Fig. 4.13: SEM images obtained after Huey's test: (a) and (b) for Alloy 600, (c) and (d) for Alloy 690, (e) and (f) for Alloy 693

The primary purpose of the Huey test is to detect the susceptibility of the alloys to intergranular corrosion due to harmful carbide precipitation. During the test, selective dissolution occurs in the chromium depleted zones and the dissolution of carbides, intermetallics, phosphides and sulphides, if present [43]. During each period of testing use of fresh nitric acid is essential. This is because the concentration of hexavalent chromium ions in 65% boiling nitric acid keeps on increasing with time, which would accelerate the corrosion attack on the specimen [44]. This attack is most dramatic above the concentration

of 30 ppm chromium ions in the solution [45]. It has been demonstrated that change of nitric acid after every 48 h minimizes the buildup of chromium ions even when severe sensitized specimen is tested. However, the hexavalent chromium ion must be kept to a minimum concentration during the entire exposure period.

Table 4.5 Corrosion rates obtained after Huey's test for the as-received specimens

Material	Corrosion Rate (mils per year)						
	24	48	96	144	192	240	Average
Alloy 600	2829	-	-	-	-	-	2829
Alloy 690	-	3.2	2.6	2.5	2.8	3.1	2.8
Alloy 693	-	258	832	1034	1042	960	825

The corrosion rate of the nickel base superalloys after each period of testing in 65% boiling nitric acid is given in Table 4.5. During the testing of Alloy 600, the material failed completely in the first 48 h, and the weight loss was more than 50% which implies very poor intergranular corrosion resistance of the alloy. Hence, the testing was restricted to only 24 h and weight loss was measured to evaluate the corrosion rate. The corrosion rate calculated for this alloy was 2829 mils per year. It could be observed from Table 4.5 that the corrosion rate of Alloy 693 is very high compared to Alloy 690. Alloy 690 showed an average corrosion rate of 2.8 mils per year, whereas Alloy 693 showed 825 mils per year. The SEM images of the specimens after Huey test are represented in Fig. 4.13. Severe intergranular corrosion with grain drop was observed in Alloy 600 and Alloy 693, whereas the grain boundary attack was very less in Alloy 690 with no grain drop. However, intergranular attack was observed at the twin boundaries of Alloy 690. Severe dissolution with pitting identified in the matrix of Alloy 600, (Fig. 4.13b) along with higher corrosion rate could be

attributed to the lower chromium content in the matrix. The higher corrosion rate of Alloy 693 is due to the higher percentage of carbon (0.09%). Microstructural characterization of Alloy 693 revealed the presence of higher amount of precipitates in the matrix as well as adjacent to grain boundaries, where selective dissolution occurs during the testing and hence, increased the corrosion rate. In addition, the smaller grain size of Alloy 693 could be responsible for higher intergranular corrosion. Smaller grain size implies shorter diffusion path and quicker carbon consumption and hence, higher intergranular corrosion [46].

4.4. Conclusions

➢ At ambient conditions, all the three alloys (Alloy 600, 690 and 693) in the as-received condition were found to possess good corrosion resistance in both 3 M HNO_3 and simulated HLW. Passivation occurred in Alloy 600 after an initial active dissolution whereas Alloy 690 and 693 were passivated spontaneously without showing any active-passive transition. The passive films formed over the specimens were found to be stable over a wide potential range.

➢ Increasing the solution temperature to 50 ^{0}C increased the passivation current density indicating a decrease in corrosion resistance. Though the stability of the passive film was low at 50 ^{0}C, all the alloys possessed good passive range.

➢ Microstructural characterization using SEM, revealed austenitic structure for all the three alloys with the presence of few precipitates at and adjacent to the grain boundary. Alloy 690 exhibited significant twin boundaries in the microstructures.

➢ Thin layer of oxides of chromium-nickel-iron formed on the surface, after electrochemical passivation of Alloy 690 and Alloy 693 in both 3 M HNO_3 and

simulated HLW was ascertained from XPS studies. Alloy 600 was found to consist of mainly film of oxides of chromium in both the media.

➢ Pitting corrosion study indicated high pitting potential for all the alloys in acidic-chloride media with concentrations of chloride ions from 500 ppm to 3000 ppm. The alloys exhibited pits of various sizes and population of pits increased with increase in chloride concentration. However, Alloy 690 exhibited only a few micropits even in 3 M nitric acid containing 3000 ppm chloride ions.

➢ Alloy 690 in the as-received condition showed superior intergranular corrosion resistance compared to Alloy 693 followed by Alloy 600.

References:

[1]   L. Vehovar, M. Tandler, Nucl. Eng. Des. 206 (2001) 21.

[2]   G.S. Was, Corrosion 46 (1990) 319.

[3]   J.D. Kim, J.H. Moon, Corros. Sci. 46 (2004) 807.

[4]   Y.S. Lim, H.P. Kim, J.H. Han, J.S. Kim, H.S. Kwon, Corros. Sci. 43 (2001) 1321.

[5]   B. In, S.P. Kim, Y.I. Kim, W.W. Kim, I.H. Kuk, et al. J. Nucl. Mater. 211 (1994) 223.

[6]   G.P. Airey, Corrosion 36 (1980) 9.

[7]   S. Takaya, T. Suzuki, T. Uchimoto, K. Miya, J. Appl. Phys. 91 (2002) 7011.

[8]   R.S. Dutta, R. Tiwari, Brit. Corros. J. 34 (1999) 201.

[9]   H. Nagano, K Yamanaka, K. Kobayashi, M. Inoue, Sumitomo Metals 40 (1988) 371.

[10] W.L. Mankins, S. Lamb, Nickel and Nickel alloys, in Metals Handbook, vol. 2, 10th edition, ASM, 1992, 428-445.

[11] J-H. Chen, W. Wu, Mater. Sci. Eng. A 489 (2008) 451.

[12] D.R. Johns, F.R. Beckitt, Corros. Sci. 30(2-3), (1990) 223.

[13] Y.S. Sato, P. Arkom, H. Kokawa, T.W. Nelson, R.J. Steel, Mater. Sci. Eng., A 477 (2008) 250.

[14] A.A. Hermas, M.S. Morad, Corros Sci. 50 (2008) 2710.

[15] S. Ningshen, U. Kamachi Mudali, G. Amarendra, Baldev Raj, Corros. Sci. 51 (2009) 322.

[16] S. Ningshen, U. Kamachi Mudali, P. Mukherjee, A. Sarkar, P. Barat, N. Padhy, Baldev Raj, Corros. Sci. 50 (2008) 2124.

[17] M. Sluyters-Rehbach, Pure Appl. Chem. 66 (1994) 1831.

[18] A.K. Shukla, R. Balasubramaniam, S. Bhargava, Intermetallics 13 (2005) 631.

[19] M.R.S. Abouzari, F. Berkemeier, G. Schmitz, D. Wilmer, Solid State Ionics 180 (2009) 922.

[20] E.B. Castro, J.R. Vilche, Electrochim. Acta 38 (1993) 1567.

[21] U. Kamachi Mudali, R. Kaul, S. Ningshen, P. Ganesh, A.K. Nath, H.S. Khatak, Baldev Raj, Mater. Sci. Tech. 22 (2006) 1185.

[22] M. Bojinov, I. Betova, G. Fabricius, T. Laitinen, R. Raicheff, T. Saario, Corros. Sci. 41 (1999) 1557.

[23] M. Sun, K. Xiao, C. Dong, X. Li, Acta Metall. Sin. (Engl. Lett.) 23 (2010) 301.

[24] F. Balbaud, G. Sanchez, P. Fauvet, G. Santarini, G. Picard, Corros. Sci. 42 (2000) 1685.

[25] F. Balbaud, G. Sanchez, G. Santarini, G. Picard, Eur. J. Inorg. Chem. 2 (1999) 277.

[26] U.R. Evans, The corrosion and oxidation of metals, Edward Arnold, London, 1960.

[27] F. Balbaud, G.Sanchez, G.Santarini, G. Picard, Eur. J. Inorg. Chem. 4 (2000) 665.

[28] P. Fauvet, F. Balbaud, R. Robin, Q.-T. Tran, A. Mugnier, D. Espinoux, J. Nucl. Mater. 375 (2008) 52.

[29] D.G. Kolman, D.K. Ford, D.P. Butt, T.O. Nelson, Corros. Sci. 39 (1997) 2067.

[30] S. Ningshen, U. Kamachi Mudali, S. Ramya, Baldev Raj, Corros. Sci. 53 (2011) 64.

[31] V.P. Razygraev, R.S. Balovneva, E.Y. Panomareva, M.V. Lebedeva, Prot. Met. 26 (1990) 43.

[32] O.W.J.S. Rutten, A.V. Sandwijk, G.V. Weert, J. Appl. Electrochem. 29 (1999) 87.

[33] R.D. Armstrong, G.E. Cleland, G.O.H. Whillock, J. Appl. Electrochem. 28 (1998) 1205.

[34] S. Girija, V.R. Raju, U. Kamachi Mudali, R.K. Dayal, Corros. Eng. Sci. Tech. 38 (2003) 309.

[35] H.H. Uligh, J.R. Gilman, Corrosion 20 (1964) 289t.

[36] W. Schwenk, Corrosion 20 (1964) 129t.

[37] N.D. Green, M.G. Fontana, Corrosion 15 (1959) 32t.

[38] R.C. Newman, M.A.A. Ajjawi, Corros. Sci. 12 (1986) 1057.

[39] H.C. Ma, C. Yang, G.Y. Li, W.J. Guo, S.H. Chen, J.L. Luo, Corrosion 59 (2003) 1112.

[40] U. Kamachi Mudali, R. K. Dayal, J. B. Gnanamurthy, P. Rodriguez, Mater. Trans. JIM, 37 (1996) 1568.

[41] W.R. Huey, Trans. Am. Soc. Steel Treating 18 (1930) 1126.

[42] ASTM Standard Practice A 262-93a, "Standard Practice for Detecting Susceptibility to Intergranular Attack in Austenitic Stainless Steels," in Annual Book of Standards, Vol. 3.02 (Philadelphia, PA: ASTM, 1988).

[43] E .Otero, A. Pardo, E. Saenz, M.V. Utrilla, F.J. Perez, Canadian Met. Quart. 36 (1997) 65.

[44] M.H. Brown, Corrosion 30 (1974) 1.

[45] W.B. Delong, Testing multiple specimens of stainless steels in a modified boiling nitric test apparatus, ASTM STP No. 93 (1949) 211.

[46] G-P. Yu, H-C. Yao, Corrosion 46 (1990) 391.

Effect of Heat Treatment on the Corrosion Behaviour of Nickel Base Superalloys

Effect of Heat Treatment on the Corrosion Behaviour of Nickel Base Superalloys

This Chapter discusses the effect of heat treatment on the corrosion behaviour of nickel base superalloys in simulated high level waste (HLW) medium. Heat treatment of the three nickel base superalloys resulted in solution-annealing followed by sensitization. The effect of heat treatment on grain size and dissolution or growth of precipitates was studied by SEM. The solution-annealed specimens were found to possess superior corrosion resistance compared to the sensitized specimens in simulated HLW. Double Loop EPR test was carried out for all the alloys to measure the degree of sensitization. Pitting corrosion resistance of the heat treated specimens was evaluated in 3 M HNO₃ containing various concentrations of chloride ions. The pitting potential and hence, pitting corrosion resistance decreased with increase in chloride ion concentration. Huey test as per ASTM A262 practice C revealed improved intergranular corrosion resistance of the nickel base alloys after solution annealing.

5.1 Introduction

The chemistry and structure of a material plays a critical role in improving the resistance towards corrosion attack. Heat treatment is the controlled heating and cooling of materials to alter their physical and mechanical properties without changing the shape of the product and it encompasses processes like annealing, quenching, tempering, thermochemical and thermomechanical treatments etc. which can affect the corrosion behaviour and induce chromium depletion, segregate the impurities to grain boundaries and also affect the

composition, structure and distribution of intergranular carbide precipitates [1]. The science of heat treatment deals with the factors and mechanism involved in the control of composition and properties. Various studies have been carried out to understand the effect of heat treatments on the corrosion behaviour of nickel base alloys. Kai et al. [2] studied the effect of heat treatment on chromium depletion and the corrosion resistance of Alloy 690. According to them, the superior corrosion resistance of Alloy 690 towards intergranular attack (IGA) was due to the high chromium content, which resulted in the high paraequilibrium chromium concentration at the grain boundary. Dutta et al. [3] investigated the microstructural and corrosion aspects of Alloy 690 in acidic solutions by aging at 700 ^{0}C for 4 h. They observed that discrete chromium carbide precipitation at the grain boundaries brought by aging adversely affected the passivity of the alloy in sulphuric acid medium. Park et al. [4] had studied the effect of heat treatment on the microstructural properties of Alloy 690 with different cooling rates and reported that the formation of carbide precipitates along the grain boundaries depends upon the cooling rate. Briant et al. [5] correlated the corrosion susceptibility of Alloy 600 with the microstructure after various heat treatments.

In Chapter 4, the general, pitting and intergranular corrosion behaviour of as-received Alloys 600, 690 and 693 had been discussed. In the present Chapter, the influence of heat treatment (solution-annealing and sensitization) on the corrosion behaviour of nickel base superalloys under simulated nuclear HLW storage condition has been described.

5.2 Experimental

➢ The as-received specimens were solution-annealed and then a few of them were induced to sensitization as per the temperature mentioned in Table 3.3.

➢ Corrosion assessment of the three nickel base alloys under heat treated (solution-annealed and sensitized) condition was carried out using electrochemical impedance spectroscopy and potentiodynamic anodic polarization techniques in simulated HLW medium.

➢ The degree of sensitization (DOS) of the heat treated specimens was investigated by carrying out double loop electrochemical potentiokinetic reactivation (DL-EPR) test.

➢ Pitting corrosion resistance of the three alloys under heat treated condition was evaluated in 3 M HNO_3 containing various concentrations of chloride ions at room temperature.

➢ Intergranular corrosion resistance of the nickel base superalloys under heat treated condition was evaluated as per ASTM A262 practice C (Huey's test) followed by microscopic examination.

5.3 Results and discussion

5.3.1 Microstructure

The optical micrographs of heat treated Alloys 600, 690 and 693 are shown in Fig. 5.1. All the alloys were found to possess austenitic structure with clear grain boundaries. Solution annealing treatment has resulted in the dissolution of most of the precipitates which were present in the as-received condition; however, it caused substantial grain growth. The sensitized specimens had comparatively smaller grain size, due to the lower heating temperature. Figures 5.2-5.4 represent the surface morphology of the heat treated Alloys 600, 690 and 693 observed under SEM.

The SEM images of solution-annealed and sensitized Alloy 600 are represented in Fig. 5.2. All the intergranular and intragranular chromium-rich carbides were dissolved by solution annealing, making it a homogeneous microstructure. However, few precipitates were observed in the matrix as well as adjacent to the grain boundary, which are highlighted in the magnified portion. These precipitates were found to be titanium-rich, as confirmed by EDS and were confirmed to be titanium nitride. The size of titanium nitride particles varied from 2-5 μm and were distributed randomly all over the matrix. Figure 5.2b shows the typical distribution of intergranular chromium-rich carbides in the sensitized Alloy 600 specimen. Sensitization treatment resulted in the precipitation of nearly continuous chromium-rich carbides at most of the grain boundaries. Additionally, titanium nitride rich precipitates were found in the matrix as well as adjacent to grain boundaries.

The surface morphology of solution-annealed Alloy 690 observed under SEM is given in Fig. 5.3a. A homogeneous microstructure was obtained after solution annealing. The insert in Fig. 5.3a shows the magnified version of grain boundaries consisting of Cr precipitates, which is well supported by EDS. The solution-annealed micrograph showed few precipitates, which are distributed randomly in the austenitic matrix. Titanium-rich precipitates observed in the matrix of solution-annealed Alloy 690 were confirmed by EDS. These precipitates comprised TiN and TiC and their volume fractions are reported to vary as per the titanium, carbon and nitrogen content [3]. These precipitates were formed during solidification. The TiN particles remained undissolved even after solution annealing at 1150 ^{0}C for 30 minutes [3]. The microstructure of Alloy 690 sensitized at 700 ^{0}C after solution annealing (shown in Fig. 5.3b) contained intergranular precipitates. Precipitates were also observed adjacent to the grain boundaries, which were found to be chromium rich. It is

reported in literature that the composition of these intergranular precipitates is $M_{23}C_6$ (M=Cr) [6-8]. Likewise, the SEM micrograph of the solution-annealed Alloy 693 exhibited few chromium rich precipitates near the grain boundaries. Sensitized Alloy 693 also contained chromium rich precipitates at and adjacent to the grain boundaries.
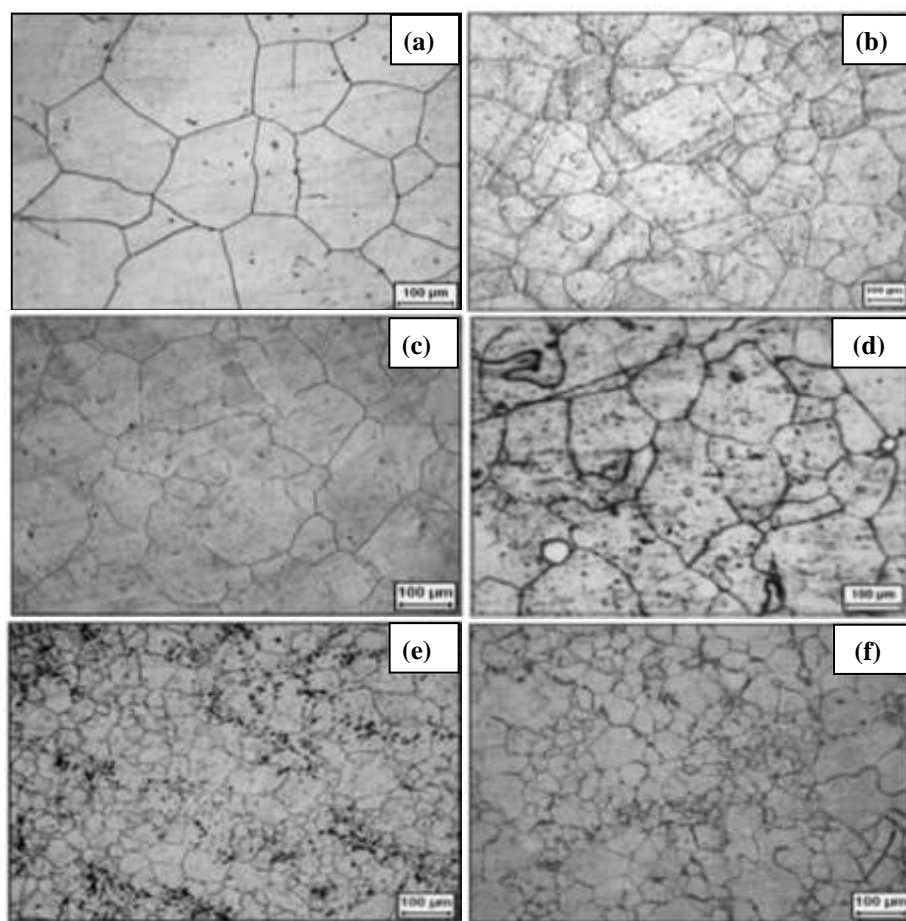
Fig. 5.1: Optical micrographs of (a) Solution-annealed and (b) Sensitized Alloy 600; (c) Solution-annealed and (d) Sensitized Alloy 690; (e) Solution-annealed and (f) Sensitized Alloy 693.
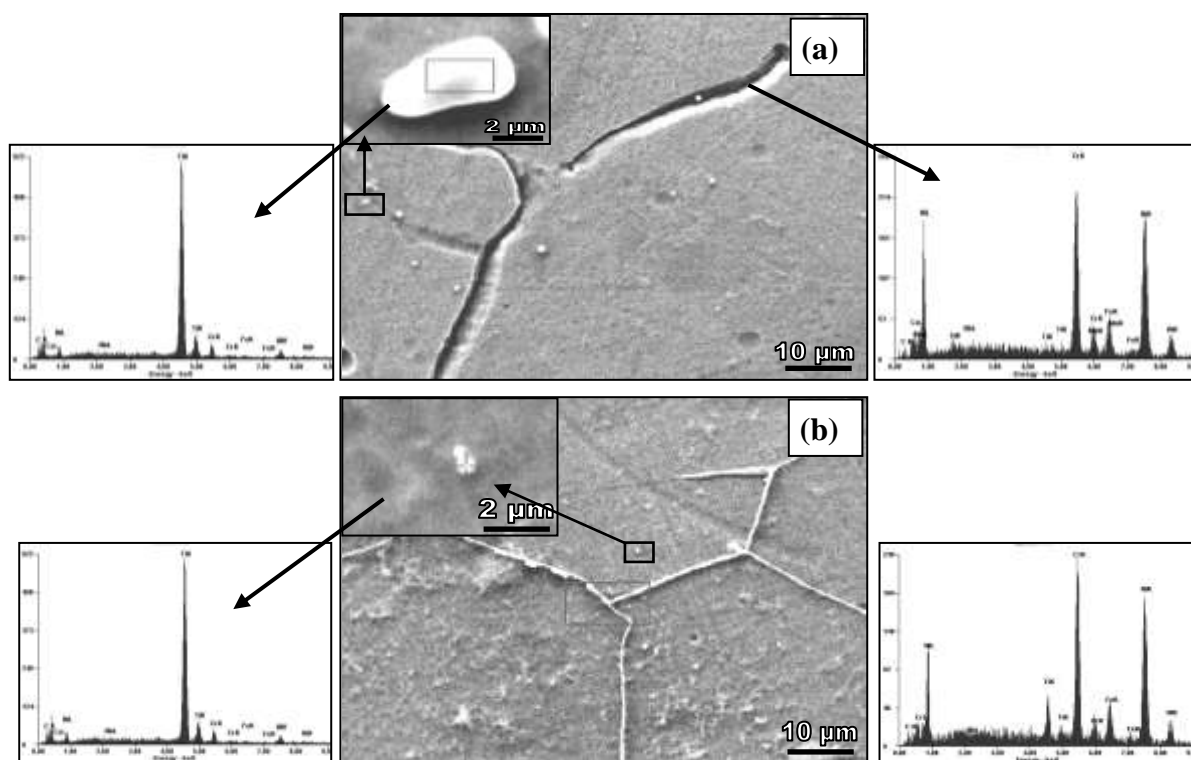
Fig. 5.2: SEM images of Alloy 600: (a) Solution-annealed and (b) Sensitized
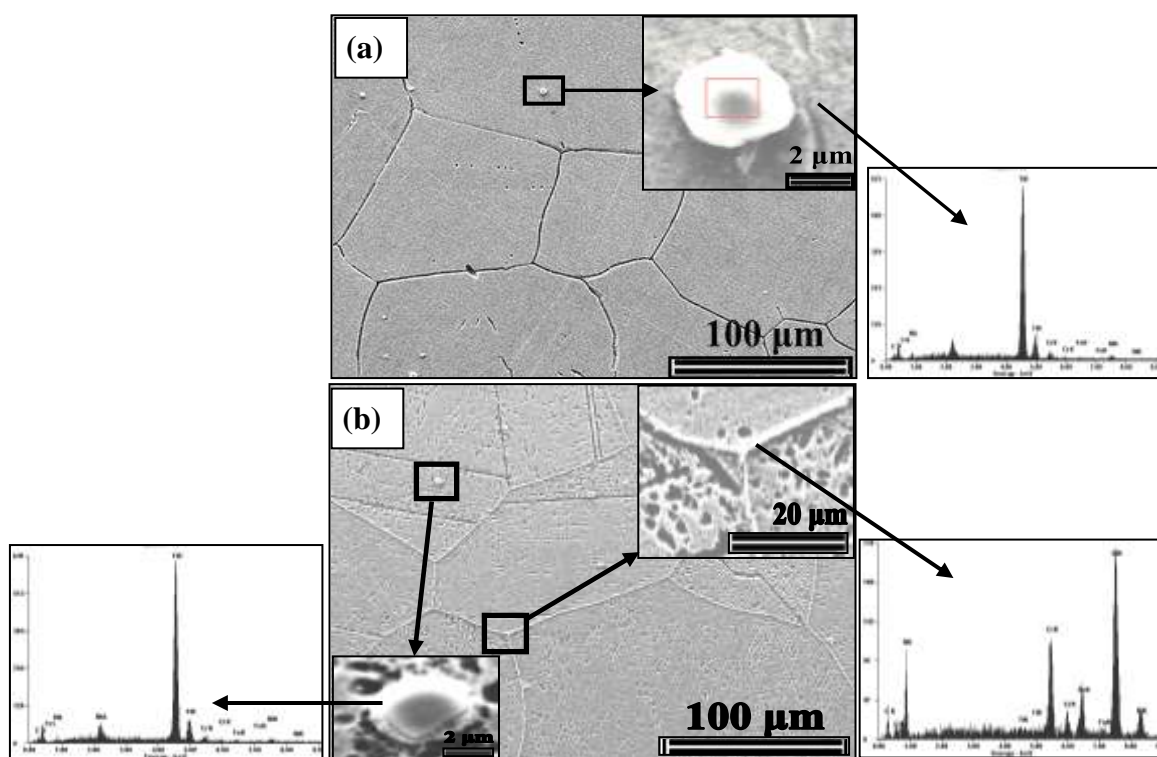
Fig. 5.3: SEM images of Alloy 690: (a) Solution-annealed and (b) Sensitized
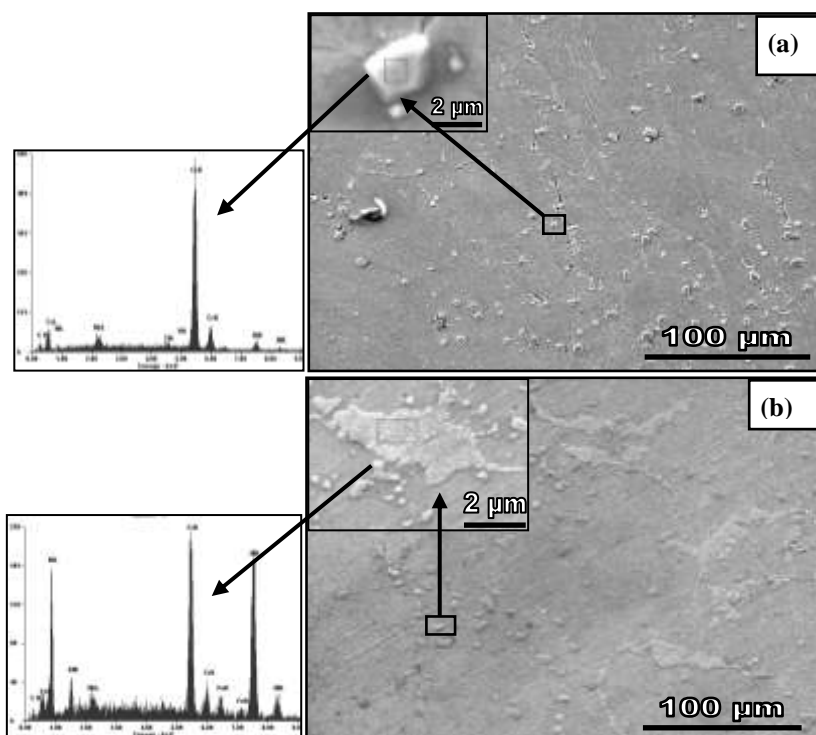
Fig. 5.4: SEM images of Alloy 693: (a) Solution-annealed and (b) Sensitized

5.3.2 Double loop electrochemical potentiokinetic reactivation (DL-EPR) test

The DL-EPR curves for the solution-annealed and sensitized Alloys 600, 690 and 693 in 0.5 M H_2SO_4 containing 0.0001 M KSCN are shown in Fig. 5.5. KSCN is used as a depassivating agent in the EPR tests, since it is a grain boundary activator and it reactivates the Cr depleted regions by destroying preferentially the oxide films formed on those regions [9]. Optimization of KSCN concentration is necessary and it depends upon the reactivation of Cr depleted regions and suppression of other types of corrosion such as pitting. Casales et al. [1] determined the optimum concentration as 0.5 M H_2SO_4 containing 0.0001 M KSCN for the DL-EPR test for Alloy 690 to measure the DOS.

The E_{corr} of solution-annealed Alloy 600 was measured to be -400 mV against Saturated Calomel Electrode (SCE) and passivation occurred at 200 mV (SCE). In the anodic

polarization experiment, the specimen was polarized at a potential of 600 mV (SCE) in the passive region, after which the scanning was reversed. During forward scanning (activation), the specimen's surface undergoes an initial active dissolution and anodic current is generated by the entire surface area which includes grains and grain boundaries, resulting in a higher current density. Once the passivation potential is reached, the specimen gets passivated. Hence, during the reverse scan the specimen is already in the passive state. During reactivation, current is generated exclusively from the defective regions of the passive film (Cr depleted zone adjacent to the grain boundaries), leading to a smaller anodic current density.

From the potentiokinetic curves and using Eq 3.6, the DOS of solution-annealed Alloy 600 specimen was found to be 0.23%, whereas it was 5% for the sensitized specimen, which value is quite high compared to the solution-annealed specimen, as listed in Table 5.1. Similarly, for Alloy 693, DOS of the solution-annealed specimen was calculated to be 0.02%, whereas it was 5.5% for the sensitized specimen. Lower DOS for the solution-annealed specimens could be attributed to the fact that during solution annealing treatment, all the pre-existing chromium rich carbides were dissolved completely leading to homogeneous solid solution without any chromium carbide and its depleted zone. It was also noticed from the potentiokinetic curves that the peak anodic current density for the sensitized specimen was larger than that of the solution-annealed specimen, implying that the corrosion rate of the sensitized specimen is higher than the solution-annealed specimen.

In the DL-EPR test carried out for Alloy 690, the reactivation peak was absent, which is evident from Fig. 5.5b. Similar observations have been reported by other investigators [10, 11]. This could be attributed to the high concentration of chromium and low concentration

of carbon in Alloy 690. Once the specimen was passivated at +600 mV (SCE), the passivation was stable throughout the reverse scanning period and hence no reactivation peak was observed. Under such conditions, Dutta et al. [10] have considered the ratio of I_a (peak activation current density) to I_f (maximum passive current density during forward scanning) as the basis for studying the extent of chromium depletion [10]. According to them, I_a is dependent on the volume fraction of Cr-carbide precipitates whereas, I_f is dependent on the extent of Cr-depletion. Therefore, the ratio of I_a to I_f, was calculated to assess the extent of chromium depletion in the Alloy 690, in the present investigation. These parameters derived from the DL-EPR curves are listed in Table 5.2. The I_a and I_f values were higher for the sensitized specimen compared to the solution-annealed specimen. The ratio of I_a to I_f was also found to be more for sensitized specimen compared to the solution-annealed specimen. The difference between the I_f values for the solution-annealed and sensitized specimens was very small compared to the difference between I_a values. The small difference between I_f values could be attributed to the high equilibrium chromium concentration at the carbide-matrix interface and the larger difference between the I_a values was due to the difference in volume fraction of Cr-carbide precipitates [10].

Table 5.1 Electrochemical parameters derived from DL-EPR curves of Alloys 600 and 693

Specimen		I_r ($\mu A/cm^2$)	I_a ($\mu A/cm^2$)	DOS (%)
Alloy 600	SA[a]	22.2	9550	0.23
	SEN[b]	596	11900	5
Alloy 693	SA	0.5	2253	0.02
	SEN	379.9	6903	5.5

[a]Solution-annealed; [b]Sensitized
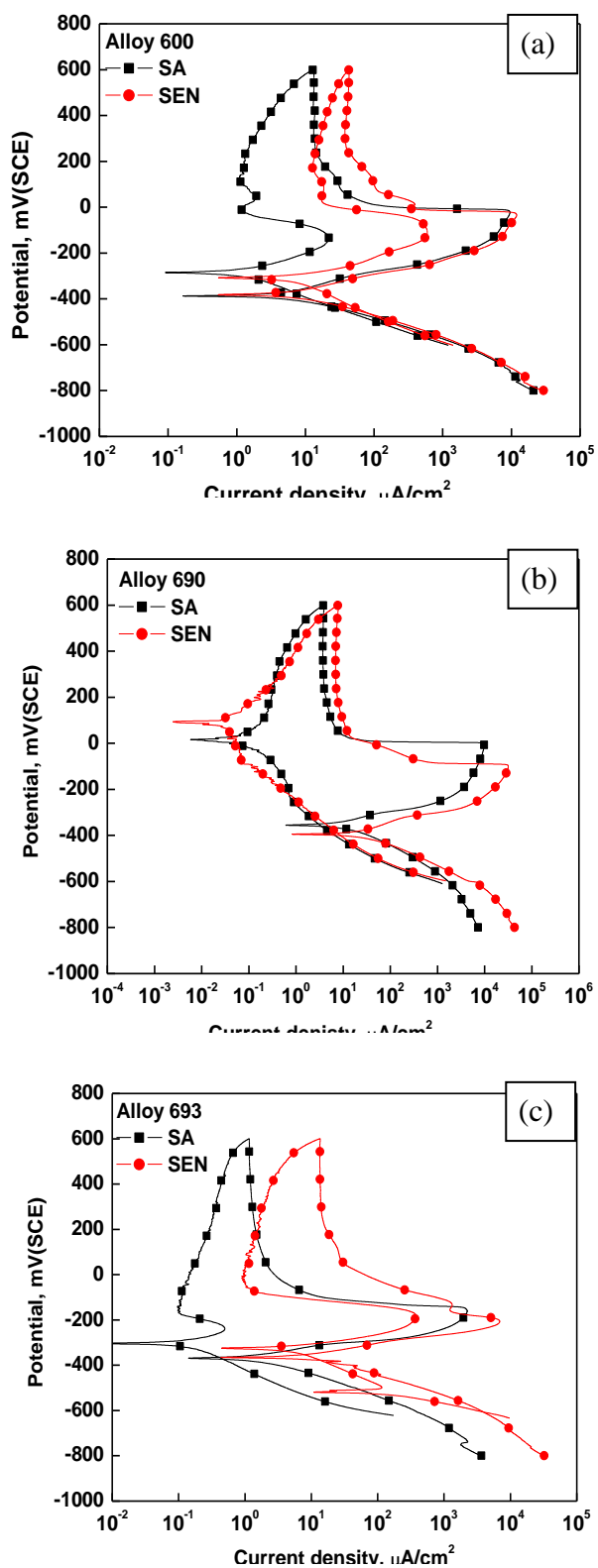
Fig. 5.5: DL-EPR curves of solution-annealed and sensitized specimens

Table 5.2 Electrochemical parameters derived from DL-EPR test of Alloy 690.

Specimen	I_a (μAcm^{-2})	I_f (μAcm^{-2})	I_a/I_f
SA	9830	3.96	2482
SEN	31750	8.12	3910

5.3.3 Electrochemical impedance spectroscopic studies in 3 M HNO₃ and simulated HLW

The electrochemical impedance spectroscopic (EIS) results for the heat treated nickel base superalloys obtained at the open circuit potential (OCP) in 3 M HNO$_3$ and simulated HLW medium are presented in Fig. 5.6 in the form of Nyquist plots. Similar impedance features were observed for all the three alloys in both the media, i.e. one depressed semicircle over the entire frequency range, which is characteristic of capacitive behaviour. Formation of such a semicircle arc is attributed to the charge transfer process at the electrode/electrolyte interface and it correlates the changes in the passive oxide property to the chemical composition [12-14]. Such a behaviour is indicative of one interfacial reaction process over the measured frequency range. The semicircle radius was smaller in the sensitized specimens as compared to the solution-annealed specimens. Similarly, the radius of the semicircle obtained in the simulated HLW medium was smaller than that in 3 M HNO$_3$ for all the three alloys. Larger semicircle radius indicates a better passive film stability and hence, better corrosion resistance.

The experimental data from Fig. 5.6 were fitted in to the Randles circuit (given in Fig. 5.7) and the electrochemical parameters obtained from the fit are reported in Table 5.3. The circuit has the element arrangement of R_S (CPE∥R_P), where R_S is the solution resistance, R_P is the polarization resistance and CPE is the constant phase element.

It could be observed from Table 5.3 that all the alloys exhibit higher R_P value for the solution-annealed specimens compared to the sensitized specimens. Higher R_P value implies good corrosion resistance. Higher R_P value for the solution-annealed specimens could be attributed to the increased stability of the passive oxide layer owing to the formation of enriched oxide of chromium/nickel or both. In contrast, the decreased R_P value for sensitized specimens indicate the deterioration or reduction in the passive film stability. Decrease in R_P could also be attributed to the increased ionic conductivity through the passive film or thinning of passive film, resulting in non-protective property [15]. The CPE parameter represents the double layer capacitance of the film/electrolyte interface. The values for the CPE parameter were relatively lower in solution-annealed specimens than the sensitized specimens for all the alloys. This indicates that less ion adsorption had occurred on the surface of the solution-annealed specimens, thereby confirming better corrosion resistance. Lower value of CPE indicates the formation of thicker and more protective passive film on the surface of solution-annealed specimen, whereas higher value indicates the non-homogeneous nature of the film on the surface of sensitized specimens, which could be the result of local defects, weakening the passive film.

Among the three alloys, highest R_P value was shown by Alloy 690 followed by Alloy 693 and 600. The R_P is sum of the film resistance and charge transfer resistance. Charge transfer processes take place at the metal/film or metal/electrolyte interface and control the rate of passive film growth on the specimens. The R_P values are strongly dependent on the passive film characteristics and is a measure of corrosion resistance.
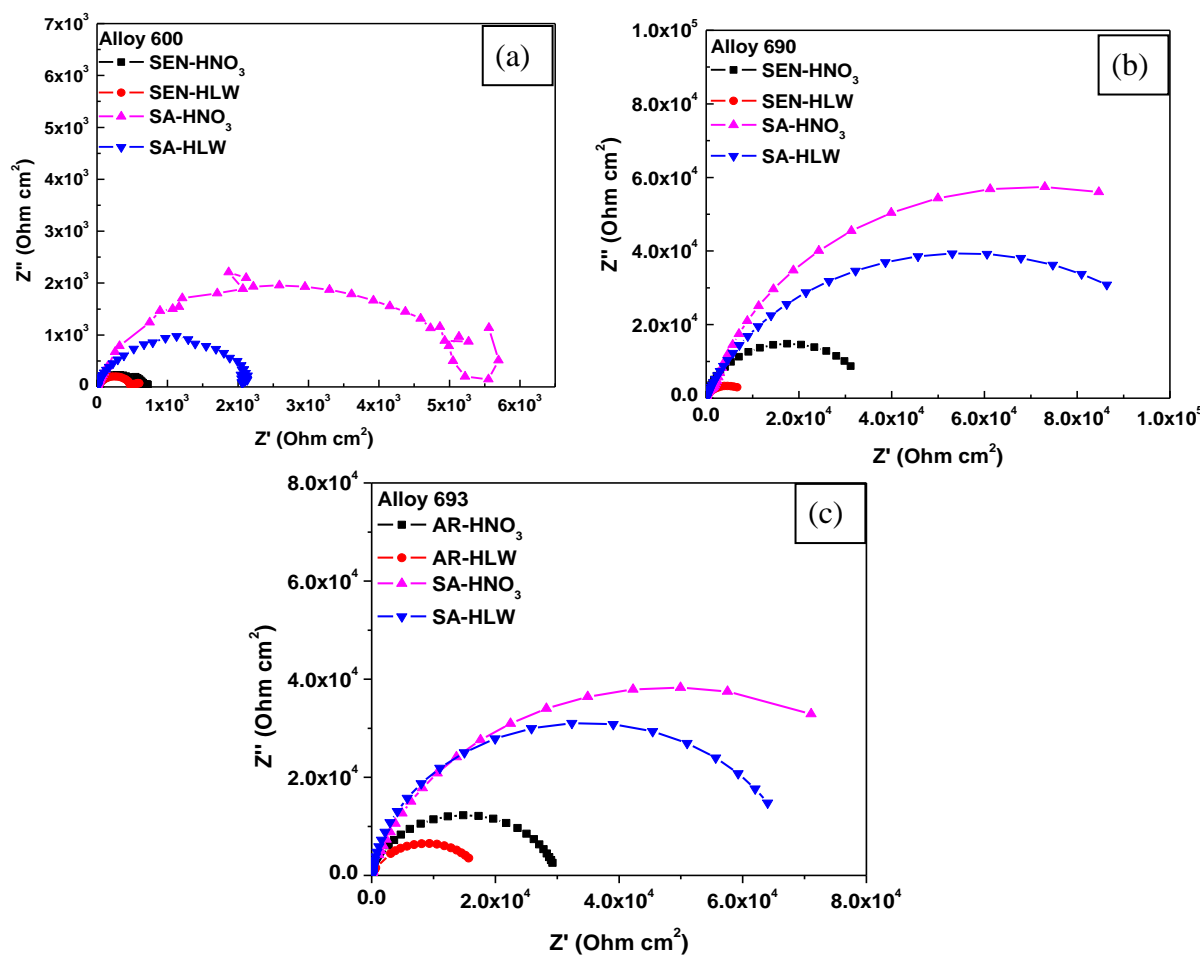
Fig. 5.6: Electrochemical impedance spectra of heat treated nickel base specimens
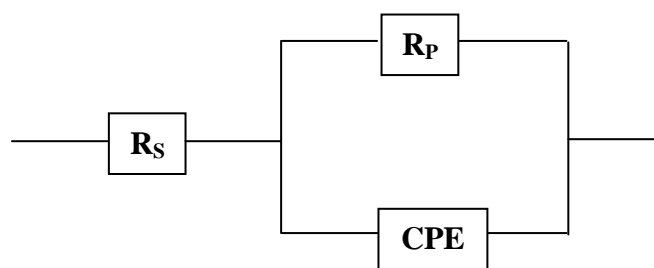
Fig. 5.7: Equivalent circuit used for EIS analysis

Table 5.3 Electrochemical parameters derived from EIS analysis

Material		Medium	R_s (Ω cm^2)	R_p (kΩ cm^2)	CPE F cm^{-2}S^n	n
Alloy 600	[a]SEN	3 M HNO$_3$	2.0	0.115	35.1x10^{-6}	0.887
		Sim. HLW	1.9	0.101	39.5 x10^{-6}	0.885
	[b]SA	3 M HNO$_3$	2.0	5.55	55.6 x10^{-6}	0.757
		Sim. HLW	2.0	2.14	73.7 x10^{-6}	0.876
Alloy 690	SEN	3 M HNO$_3$	2.02	35.4	97.9 x10^{-6}	0.885
		Sim. HLW	0.45	35.4	72.2 x10^{-6}	0.786
	SA	3 M HNO$_3$	1.30	22.3	54.5 x10^{-6}	0.947
		Sim. HLW	1.00	90	35.2 x10^{-6}	0.871
Alloy 693	SEN	3 M HNO$_3$	0.75	30.0	34.0 x10^{-6}	0.873
		Sim. HLW	1.30	23.5	54.5 x10^{-6}	0.911
	SA	3 M HNO$_3$	0.65	69.1	45.6 x10^{-6}	0.881
		Sim. HLW	1.0	90	60.3 x10^{-6}	0.933

[a]Sensitized; [b]Solution-annealed

5.3.4 Potentiodynamic anodic polarization measurements in 3 M HNO$_3$ and simulated HLW

The potentiodynamic anodic polarization curves obtained for the heat treated specimens in 3 M HNO$_3$ and simulated HLW at the solution temperatures of 25 and 50 ^{0}C are given in Fig. 5.8. Electrochemical parameters such as corrosion potential (E$_{corr}$), passivation current density (I$_{pass}$), transpassive potential (E$_{TP}$) and passive range derived from the polarization curves are listed in Table 5.4.

In 3 M HNO$_3$ at the solution temperature of 25 ^{0}C, the E$_{corr}$ of solution-annealed Alloy 600 was 0 mV (SCE) and the specimen passivated spontaneously, maintaining a very low I$_{pass}$ (0.2 µA/cm^2) without exhibiting the active to passive transition peak. The material was

observed to be passive over a wide range of potential (up to 750 mV (SCE)) before transpassive dissolution occurred at 860 mV (SCE). When the temperature of solution was increased to 50 ^{0}C, the E_{corr} and I_{pass} increased to 230 mV (SCE) and 3.5 $\mu A/cm^2$ respectively. The passive range decreased to 550 mV (SCE). The E_{TP} was found to be more or less in the same range. In simulated HLW solution, the E_{corr} of solution-annealed Alloy 600 was found to be comparatively higher than that in 3 M HNO_3 at both 25 and 50 ^{0}C. I_{pass} of these specimens in simulated HLW was also higher compared to 3 M HNO_3 and the passive range was less compared to that in 3 M HNO_3. Similar results were obtained in the case of sensitized specimen. The E_{corr} as well as I_{pass} were found to increase at 50 ^{0}C compared to 25 ^{0}C in both 3 M HNO_3 and simulated HLW.

The polarization curves for solution-annealed specimens of Alloy 690 and 693 in 3 M HNO_3, at 25 ^{0}C were characterized by the E_{corr} values of 310 and 280 mV (SCE) respectively. Both the specimens passivated spontaneously without exhibiting the active to passive transition peak, and maintained a very low I_{pass} value. In simulated HLW at 25 ^{0}C, the E_{corr} was found to increase whereas the I_{pass} increased marginally as compared to that in 3 M HNO_3. Though, the E_{TP} value remained in the same range, a decrease in passive range was observed in simulated HLW. With increase in temperature from 25^0C to 50^0C, the E_{corr} as well as I_{pass} were found to increase in both 3 M HNO_3 and simulated HLW. From the potentiodynamic anodic polarization curves for sensitized Alloys 690 and 693 in 3 M HNO_3 and simulated HLW, an increase in E_{corr} as well as I_{pass} was observed for both the alloys in simulated HLW compared to 3 M HNO_3. Similar observations were found while increasing the solution temperature.

The increase in E_{corr} with increasing temperature could be attributed to the global reduction of nitrates. The autocatalytic mechanism of reduction, prevailing in the nitric acid concentration employed in the present study had been already discussed in Chapter 4. The electrochemical reaction governing the redox potential could be represented as follows [16-18]:

$$NO_3^- + 3\ H^+ + 2\ e^- = HNO_2 + H_2O\ (\ E_{25^oC} = 934\ mV/\ SHE) \qquad (5.1)$$
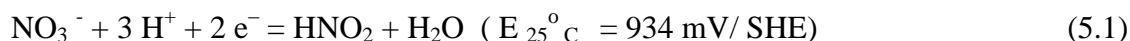
From thermodynamic point of view, the redox potential imposed by $[HNO_2]/[NO_3^-]$ ratio (Eq. 5.1) increases with increase in temperature and ennobles the E_{corr}. From kinetic point of view, the reduction products such as HNO_2 and NO (generated during autocatalytic reduction) catalyze the reduction process [17, 19]. Increasing the temperature increases the reduction rate and hence, the E_{corr} increases. Increasing the temperature also favours the transformation of the stable and insoluble chromium (III) oxide (Cr_2O_3) to soluble chromium (VI) oxide ($Cr_2O_7^{2-}$). The oxide film thus becomes comparatively unstable leading to its dissolution and resulting in an increase in the I_{pass}. In simulated HLW, the E_{corr} was further ennobled due to the presence of oxidizing ions such as Fe (III), Cr (VI) etc., which catalyzes the reduction [17, 18, 20].

In the present study, the solution-annealed specimens exhibited a lower I_{pass} value compared to the as-received and sensitized specimens, due to the homogeneous surface obtained after solution-annealing. However, the difference was not very significant in most of the cases and the I_{pass} values were found to be in close proximity. This could be attributed to the aggressiveness of the media. 3 M HNO_3 solution is too aggressive to distinguish the effect of heat treatment on the specimens. However, the superior corrosion resistance of solution-annealed specimens could be confirmed from the post-experimental optical micrographs of
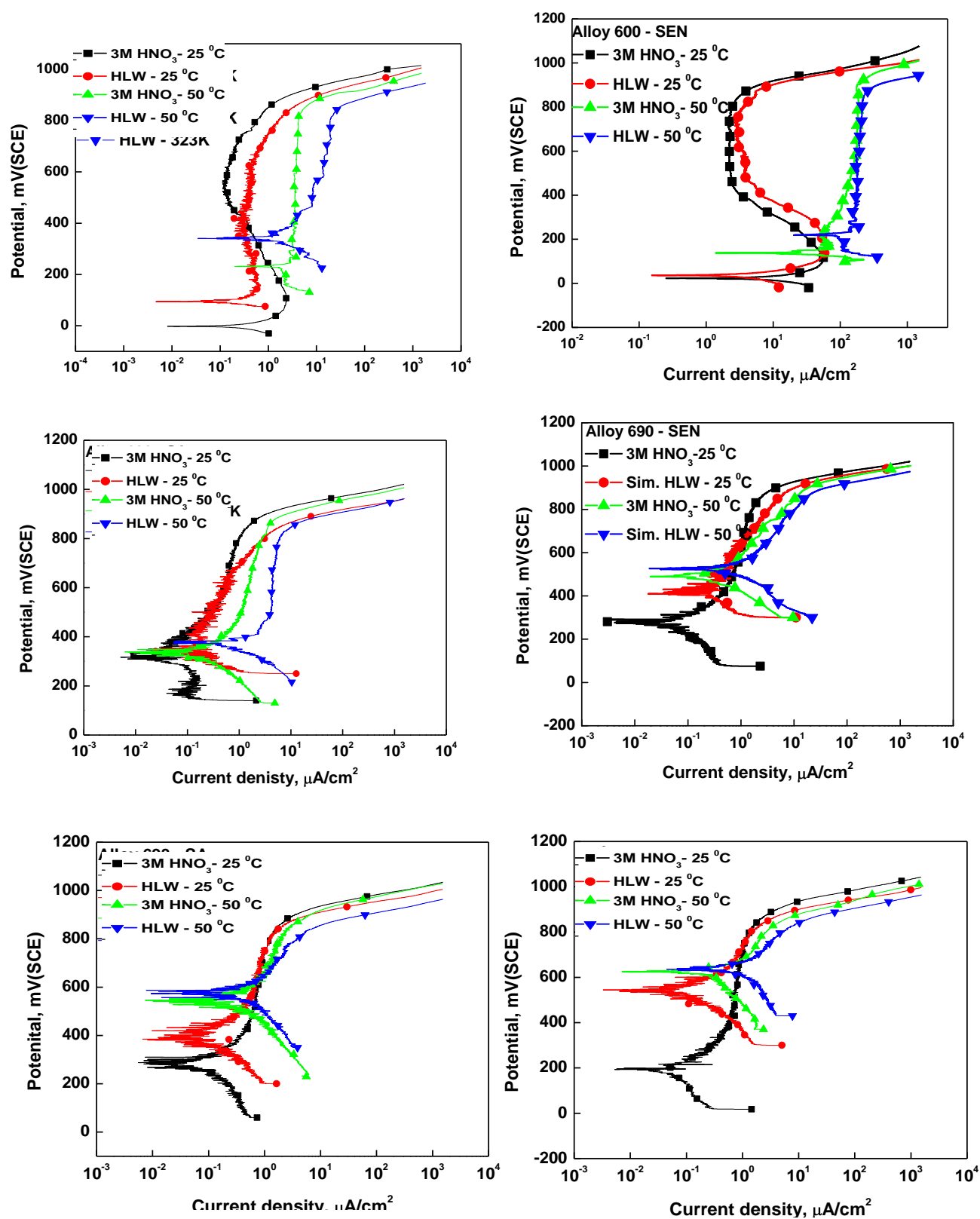
Fig. 5.8: Polarization curves of the heat treated specimens of Alloys 600, 690 and 693

the specimens, which revealed no attack on the surface of solution-annealed specimens; whereas, the sensitized specimens were found to be attacked and the grain boundaries were exposed particularly in the case of Alloys 600 and 693. Formation of chromium depleted zones at the grain boundary during sensitization process, resulted in a less protective passive film at such locations and hence, preferential attack occurred.

Table 5.4 Electrochemical parameters derived from polarization curves for the heat treated specimens

Material	Medium		25 ^{0}C				50 ^{0}C		
		$E_{corr.}$	I_{pass}	E_{TP}	Pass. Range	E_{corr}	I_{pass}	E_{TP}	Pass. Range
Alloy 600	SA	3 M HNO$_3$	0	0.2	860	750	230	3.5	860	550
		Sim HLW	90	0.4	820	650	340	1.4	850	650
	SEN	3 M HNO$_3$	0	2.3	860	750	140	174	860	700
		Sim HLW	04	4.0	860	700	230	185	860	600
Alloy 690	SA	3 M HNO$_3$	310	0.6	880	540	340	1.5	900	500
		Sim HLW	350	0.75	850	480	375	4.2	850	430
	SEN	3 M HNO$_3$	290	1.05	890	440	480	2.5	890	370
		Sim HLW	400	1.3	880	400	530	4.1	875	300
Alloy 693	SA	3 M HNO$_3$	280	0.73	880	540	540	1.3	890	280
		Sim HLW	400	0.8	870	340	575	1.7	840	230
	SEN	3 M HNO$_3$	200	0.8	880	600	625	2.1	870	200
		Sim HLW	540	1.0	850	250	640	3.2	850	180

*All potentials are in mV (SCE) and current in µA/cm^2
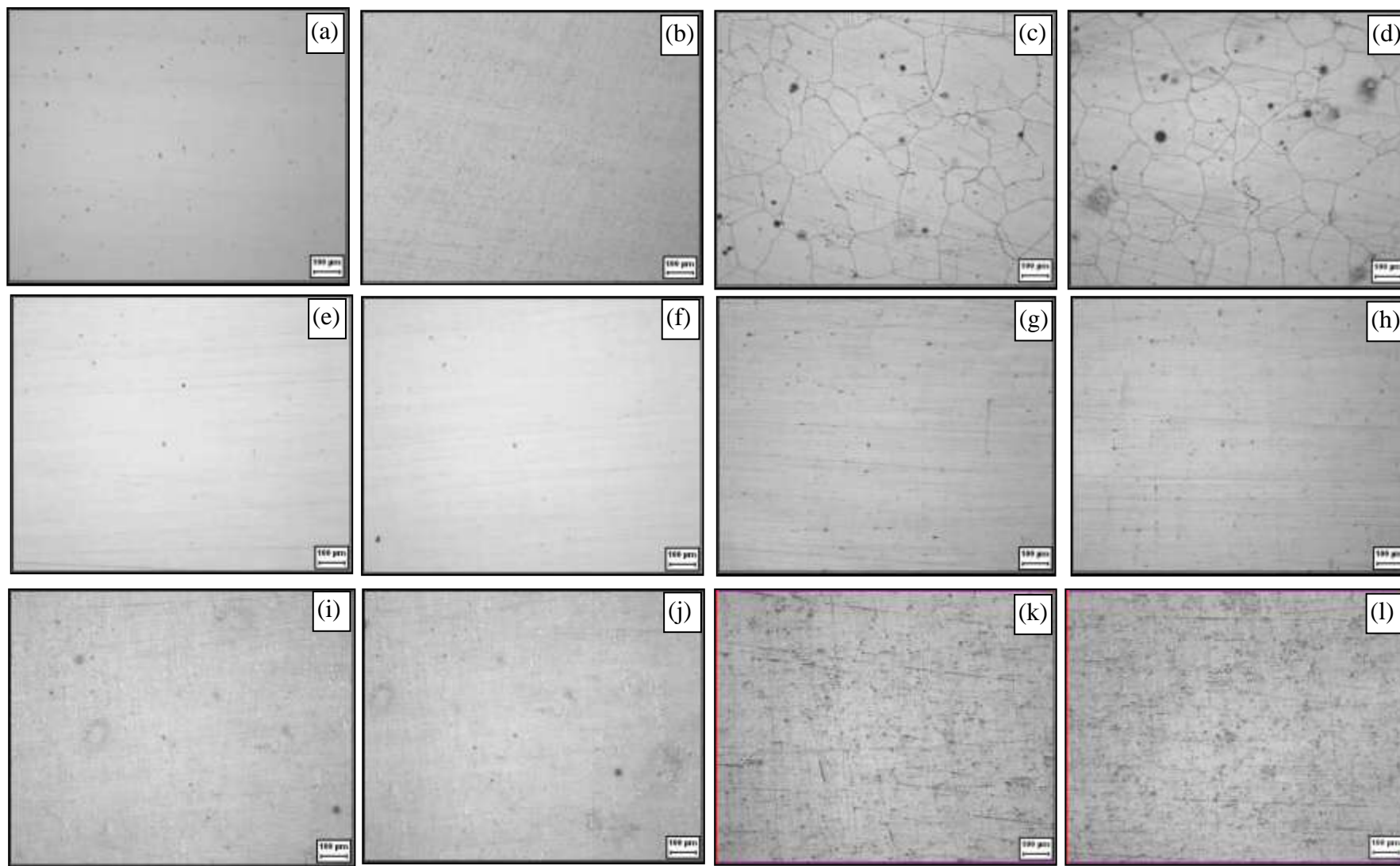
Fig. 5.9: Post-experimental optical micrographs of SA-Alloy 600 in (a) 3 M HNO_3 (b) Sim. HLW; SEN-Alloy 600 in (c) 3 M HNO_3 (d) Sim. HLW; SA-Alloy 690 in (e) 3 M HNO_3 (f) Sim. HLW; SEN-Alloy 690 in (g) 3 M HNO_3 (h) Sim. HLW; SA-Alloy 693 in (i) 3 M HNO_3 (j) Sim. HLW; SEN-Alloy 693 in (k) 3 M HNO_3 (l) Sim. HLW

5.3.5 Pitting corrosion resistance

The potentiodynamic anodic polarization curves for Alloys 600, 690 and 693 under heat treated conditions in 3 M HNO_3 containing various concentrations (500, 1000, 2000 and 3000 ppm) of chloride ions at 25 ^{0}C are reproduced in Fig. 5.10. The electrochemical parameters viz. E_{corr}, I_{pass} and E_{pit} are reported in Table 5.5.

Alloy 600 in both solution-annealed and sensitized conditions showed a negative value for E_{corr} followed by a critical current peak during active dissolution. The active dissolution was followed by a passive region which extended until the occurrence of oxygen evolution and subsequent breakdown, where an abrupt increase in current was recorded. For Alloy 600, the I_{pass} value was found to be 3.8 $\mu A/cm^2$ for the solution-annealed specimen, whereas it was 35 $\mu A/cm^2$ for the sensitized specimen in 500 ppm chloride ion concentration. Further increase in chloride ion concentration caused a decrease in the E_{corr} and an increase in the I_{pass} for solution-annealed as well as sensitized specimens. An increase in peak current density was also observed in the active region with increase in chloride ion concentration. For the Alloy 690 and Alloy 693 under solution-annealed condition in 3 M HNO_3 containing 500 ppm chloride ions, the E_{corr} was found to be in the range of 400 mV (SCE) and it decreased with increase in chloride ion concentration. The I_{pass} was found to be less than 1 $\mu A/cm^2$ at all concentrations of chloride ions for both the alloys. A similar trend was observed in E_{corr} for the sensitized Alloys 690 and 693 specimens with increasing concentration of chloride ions. The I_{pass} of sensitized Alloy 690 was found to be about 1 $\mu A/cm^2$, whereas for the sensitized Alloy 693, it was observed to be in the range 10 $\mu A/cm^2$. The increase in I_{pass} indicates increase in anodic dissolution. Higher value of I_{pass} could be attributed to lower stability and less protective nature of the passive film.

Table 5.5 Electrochemical parameters obtained from polarization curves

Material		Cl^- (ppm)	E_{corr}, mV(SCE)	I_{pass}, $\mu A/cm^2$	E_{pit}, mV(SCE)
Alloy 600	SA	500	-100	3.8	950
		1000	-130	5.3	950
		2000	-170	12.6	925
		3000	-185	35.9	925
	SEN	500	-85	35	920
		1000	-150	40	920
		2000	-155	42	920
		3000	-180	133	920
Alloy 690	SA	500	380	0.6	955
		1000	290	0.7	955
		2000	230	0.8	935
		3000	130	0.9	935
	SEN	500	360	0.8	950
		1000	340	0.8	950
		2000	350	0.9	945
		3000	295	0.8	950
Alloy 693	SA	500	480	0.8	955
		1000	435	0.8	955
		2000	390	0.9	950
		3000	250	0.7	950
	SEN	500	500	7	900
		1000	460	6	900
		2000	455	8	890
		3000	420	9	895

Fig. 5.10: Polarization curves for the heat treated nickel base alloys in 3 M nitric acid-chloride media
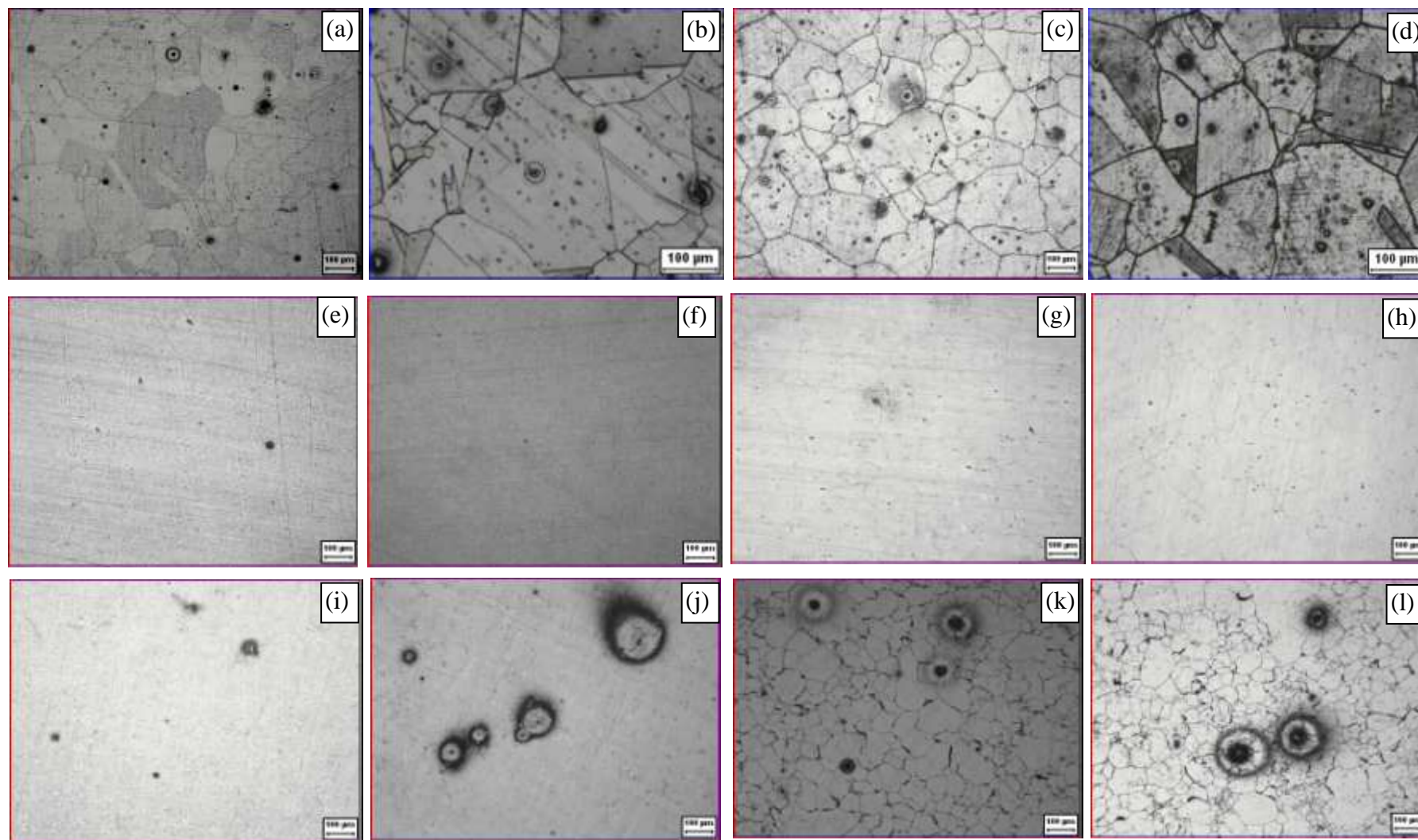
Fig. 5.11: Optical micrographs showing pits after polarization experiment in acidic-chloride media: SA-Alloy 600 in (a) 500 ppm Cl⁻ and (b) 3000 ppm Cl⁻ ; SEN-Alloy 600 in (c) 500 ppm Cl⁻ and (d) 3000 ppm Cl⁻ ; SA-Alloy 690 in (e) 500 ppm Cl⁻ and (f) 3000 ppm Cl⁻ ; SEN-Alloy 690 in (g) 500 ppm Cl⁻ and (h) 3000 ppm Cl⁻ ; SA-Alloy 693 in (i) 500 ppm Cl⁻ and (j) 3000 ppm Cl⁻ and; SEN-Alloy 693 in (k) 500 ppm Cl⁻ and (l) 3000 ppm Cl⁻ .

Unlike Alloy 600, no active-passive transition was observed in the heat treated Alloys 690 and 693. Both these alloys passivated spontaneously without any active dissolution in solution-annealed as well as in sensitized condition at all concentrations of chloride ions. The spontaneous passivation is attributed to the autocatalytic reduction of nitric acid.
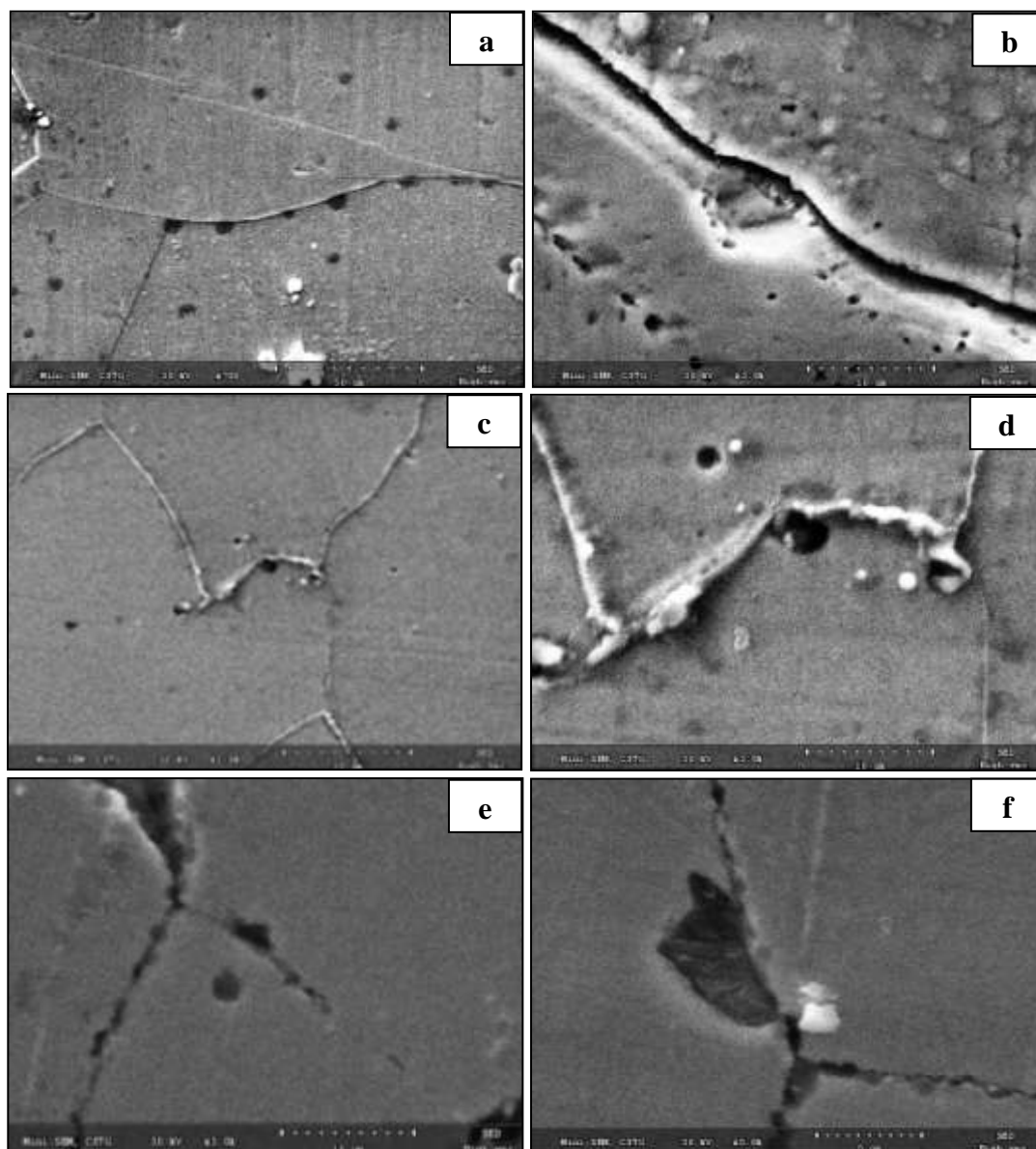
Fig. 5.12: SEM micrographs showing the initiation of pits at grain boundaries: (a) SA Alloy 600; (b) SEN Alloy 600; (c) SA Alloy 690; (d) SEN Alloy 690; (e) SA Alloy 693 and (f) SEN Alloy 693.

Optical microscopic examination showed pits of various sizes in all the specimens (Fig. 5.11). Alloy 690 showed only a few micropits in solution-annealed condition at all concentrations of chloride ions; whereas Alloy 600 and 693 revealed pits of various sizes and shapes with attack at the grain boundaries. The population and size of pits increased with increase in chloride ion concentration. In the case of sensitized specimens, the grain boundaries were exposed and severe pitting was observed. Though the extent of pitting corrosion was found to be different for these alloys, the E_{pit} were observed in the same range. All the solution-annealed specimens showed E_{pit} at around 950 mV (SCE), and all the sensitized specimens showed marginally lower E_{pit} values. Such high values of E_{pit} observed could be due to the highly passivating nature of 3 M HNO_3.

Figure 5.12 shows the SEM images of the pits formed on the surface of various specimens. Most of the pits were generated primarily at the grain boundaries. This could be due to the precipitation of complex carbides, which depletes this region from Cr and other alloying elements [21].

In the present investigation, as a result of homogenised microstructure, stable passive film was formed on the surface of solution-annealed specimen and hence, the solution-annealed specimens were found to exhibit lower I_{pass} compared to the sensitized specimens, for all the alloys. Solution-annealing treatment at high temperatures facilitates the dissolution of second phase particles, leading to marked improvement in pitting resistance [22]. Thus the stable passive film formed on the solution-annealed specimen had resulted in improved corrosion resistance when compared to the sensitized specimens.

5.3.6 Intergranular corrosion resistance

The intergranular corrosion resistance of the three nickel base alloys under heat treated conditions was evaluated by Huey test (ASTM 202A, practice C) [23], in which the specimens were immersed in 65% boiling nitric acid for five periods with durations of 48 h for each period. The weight loss was measured after each period of testing and corrosion rate was calculated using Eq. 4.8.

As discussed in Chapter 4, the intergranular corrosion testing for Alloy 600 under as-received condition was restricted to 24 h; therefore, the same time period was applied to the heat treated Alloy 600 specimens also. The corrosion rate of the heat treated nickel base superalloys after each period of testing in 65% boiling nitric acid is given in Table 5.6.

Table 5.6 Corrosion rates determined after Huey's test for heat-treated specimens

Material		Corrosion Rate (mils per year)						
		24	48	96	144	192	240	Average
Alloy 600	SA	4.8	-	-	-	-	-	4.8
	SEN	3540	-	-	-	-	-	3540
Alloy 690	SA	-	2.16	2.16	2.16	2.16	2.16	2.16
	SEN	-	3.21	3.23	3.23	3.24	3.25	3.23
Alloy 693	SA	-	2.93	2.95	2.96	2.98	2.99	2.97
	SEN	-	1255	1259	1262	1260	1262	1261
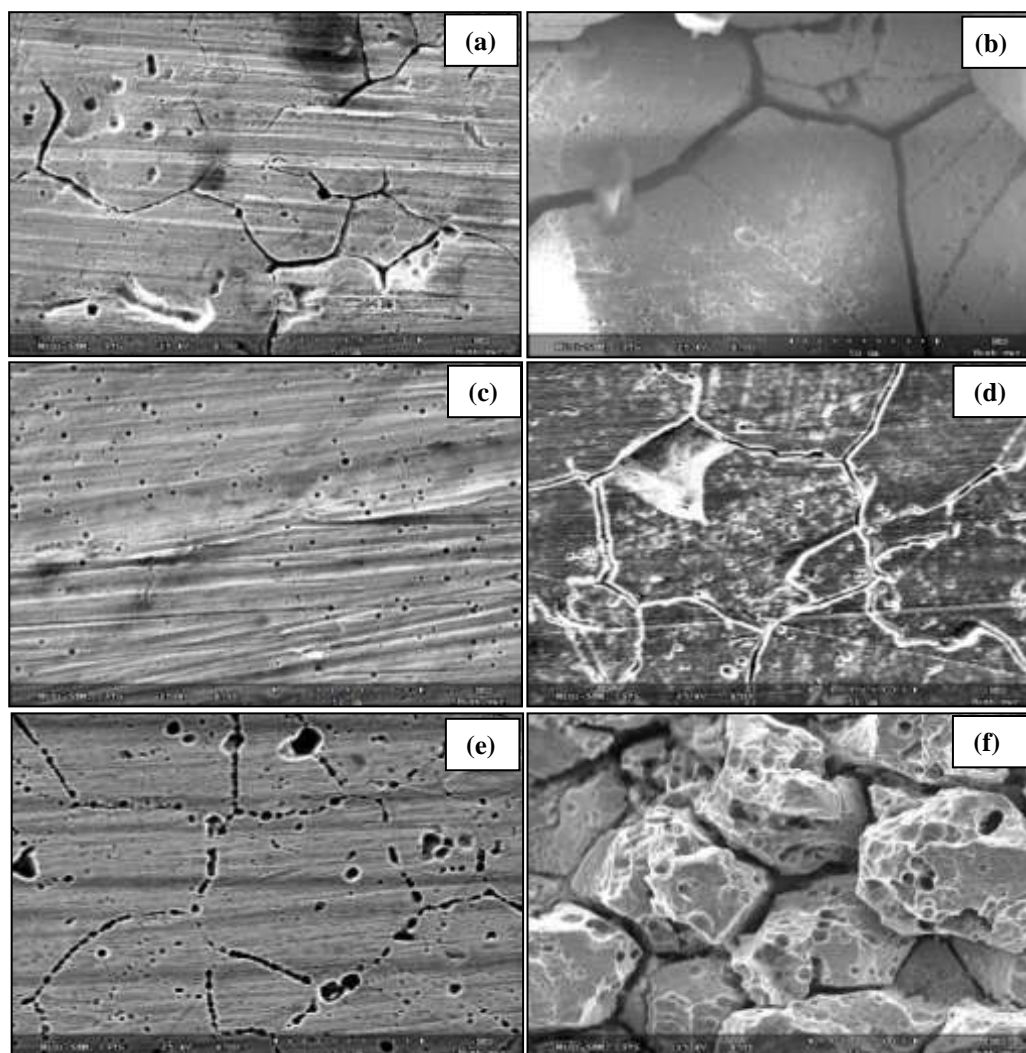
Fig. 5.13: SEM images obtained after Huey test: (a) SA and (b) SEN Alloy 600; (c) SA and (d) SEN Alloy 690; (e) SA and (f) SEN Alloy 693

The SEM images of the specimens obtained after Huey test are shown in Fig. 5.13. Intergranular corrosion was observed in all the cases. The solution-annealed Alloys 690 and 693 did not show any significant weight loss after 240 h test and the corrosion rate was found to be less than 3 mils per year and hence, exhibited excellent intergranular corrosion resistance compared to the as-received and sensitized specimens. Some grain boundaries in the solution-annealed Alloy 600 specimen were corroded; however, along many boundaries,

the corrosion attack was only in localized areas with parts of the boundary remaining unattacked. The corrosion attack on the solution-annealed Alloy 693 was along the grain boundaries. The grain boundaries of solution-annealed Alloy 690 were also marginally attacked. The sensitized Alloy 600 and 693 specimens corroded to an extent that many grains dropped from their surface, but no grain had dropped from the sensitized Alloy 690 specimen. The grain boundaries of the sensitized Alloy 690 were also attacked and the precipitates within the grains had been etched away.

5.4 Conclusions

➢ SEM examination revealed that most of the pre-existing precipitates in the Alloys 600, 690 and 693 had dissolved after solution annealing, though few precipitates were observed on the specimen. The sensitized specimens were found to possess Cr depleted regions in addition to some precipitates in the matrix.

➢ The degree of sensitization had been determined for the alloys in 0.5 M H_2SO_4 containing 0.0001 M KSCN. Low degree of sensitization was observed for the solution-annealed specimens compared to the sensitized specimens. Alloy 690 was found to contain no reactivation peak, which is due to the high chromium and low carbon concentration.

➢ All the alloys exhibited good corrosion resistance in 3 M HNO_3 and simulated HLW at 25 ^{0}C, in the solution-annealed condition. With the increase in solution temperature to 50 ^{0}C, the corrosion potential as well passivation current denisity were found to increase.

> ➢ The sensitized specimens possessed lower corrosion resistance when compared to solution-annealed specimens in both 3 M HNO_3 and in simulated HLW. However, the passivation current densities were found to be in close proximity.

> ➢ Alloy 690 exhibited excellent pitting as well as intergranular corrosion resistance in both solution-annealed and sensitized conditions as compared to both Alloy 693 and Alloy 600.

References:

[1]   M. Casales, M.A. Espinoza-Medina, A. Martinez-Villafane, V.M. Salinas-Bravo, J.G. Gonzalez-Rodriguez, Corrosion 56 (2000) 1133.

[2]   J. J. Kai, G. P. Yu, C. H. Tsai, M. N. Liu, S. C. Yao, Metal. Trans. A, 20 (1989) 2057.

[3]   R. S. Dutta, R. Tiwari, British Corros. J. 34 (1999) 201.

[4]   N. P. Park, J. J. Kim, Y. S. Chai, H. S. Lee, Key Eng. Mater. 353-358 (2007) 1609.

[5]   C. L. Briant, C. S. O'toole, E. L. Hall, Corrosion, 42 (1986) 15.

[6]   G. -P. Yu, H. -C. Yao, Corrosion 46 (1990) 391.

[7]   J. J. Kai, G. P. Yu, C. H. Tsai, M. N. Liu, S. C. Yao, Metal. Trans. A, 20 (1989) 2057.

[8]   V. Cihal, I. Kasova, Corros Sci. 10 (1970) 875.

[9]   M. Prazak, Corrosion 19 (1963) 75.

[10]   R. S. Dutta, R. Tewari, P. K. De, Corros. Sci. 49 (2007) 303.

[11]   H. T. Lee, J. L. Wu, Corros. Sci. 51 (2009) 439.

[12]   A. A. Hermas, M. S. Morad, Corros Sci. 50 (2008) 2710.

[13]   S. Ningshen, U. Kamachi Mudali, G. Amarendra, Baldev Raj, Corros. Sci. 51 (2009) 322.

[14] S. Ningshen, U. Kamachi Mudali, P. Mukherjee, A. Sarkar, P. Barat, N. Padhy, Baldev Raj, Corros. Sci. 50 (2008) 2124.

[15] E. B. Castro, J. R. Vilche, Electrochim. Acta, 38 (1993) 1567.

[16] F. Balbaud, G. Sanchez, G. Santarini, G. Picard, Eur. J. Inorg. Chem. 4 (2000) 665.

[17] P. Fauvet, F. Balbaud, R. Robin, Q. -T. Tran, A. Mugnier, D. Espinoux, J. Nucl. Mater. 375 (2008) 52.

[18] S. Ningshen, U. Kamachi Mudali, S. Ramya, Baldev Raj, Corros. Sci. 53 (2011) 64.

[19] F. Balbaud, G. Sanchez, P. Fauvet, G. Santarini, G. Picard, Corros. Sci. 42 (2000) 1685.

[20] R. D. Armstrong, G. E. Cleland, G. O. H. Whillock, J. Appl. Electrochem. 28 (1998) 1205.

[21] A. J. Sedriks, Corrosion of Stainless Steels, John-Wiley and Sons, New York (1996).

[22] N. D. Tomashov, G. P. Tehernova, N. Mankova, Corrosion 20 (1964) 166t.

[23] ASTM Standard Practice A 262-93a, "Standard practice for detecting susceptibility to intergranular attack in austenitic stainless steels," in Annual Book of Standards, Vol. 3.02 (Philadelphia, PA: ASTM, 1988).

CHAPTER **6**

**Surface Modification of Nickel Base
Superalloys by Laser Treatment**

Surface Modification of Nickel Base Superalloys by Laser Treatment

Laser melting of the surface of the Ni base superalloys was carried out to study the effect of surface modification on their corrosion behaviour in simulated nuclear high level waste (HLW) and chloride media. Surface characterization of the laser melted samples was carried out by optical microscope, scanning electron microscope and x-ray diffraction. The alloys exhibited cubic crystal phase and cellular microstructure. Double loop electrochemical potentiokinetic reactivation test showed lower degree of sensitization. Laser surface melting resulted in the enhancement of corrosion resistance of the alloys in simulated HLW and acid-chloride medium compared to the as-received and heat treated specimens; nevertheless, no discernable difference was found in the corrosion behaviour of laser surface melted alloys in simulated HLW. Laser surface melted Alloy 690 showed superior pitting corrosion resistance compared to Alloys 600 and 693.

6.1 Introduction

Surface treatment techniques like electro-polishing, heat treatment and chemical passivation are used to improve the corrosion resistance of different materials without affecting the bulk mechanical and physical properties. However, compared to these conventional methods, rapid solidification processes can produce a homogeneous distribution of elements and extended solid solutions [1, 2]. In the last few decades, laser surface modification of materials has found increasing use in engineering applications to enhance the surface

properties by altering of surface chemistry and structure. It is one of the important categories of surface engineering tools because of its characteristic features such as rapid heating and melting which facilitate the possibility of extended solid solution, fine microstructure, composition homogenization, excellent metallurgical interface etc. [3-6]. The other advantages of laser surface modification over conventional processes include short processing time, flexibility in operation, time effectiveness, energy, material consumption etc. [5, 7-11]. High power intensities and short interaction durations result in rapid heating as well as cooling. This in turn, produces a shallow heat affected zone (HAZ) and low distortion of the specimen with minimum deterioration of bulk parameters [12]. Additionally, rapid solidification process produces refined and novel microstructures, which improve the surface properties like wear and corrosion [13-17]. Laser surface modification techniques that are used to improve the corrosion resistance of materials include transformation hardening, alloying, cladding, melting and particle injection [18].

Laser surface melting potentially improves the corrosion resistance of materials, without changing the mechanical properties of the bulk. A high power laser beam rapidly melts a thin layer of the surface and the rest of the material provides self-quenching at cooling rates of up to $10^4 - 10^8$ Ks^{-1}[19-21]. The rapid cooling rate results in homogenization of the microstructure and dissolution or re-distribution of second phase particles/inclusions [19, 21, 22]. Typical thickness of laser melted layers ranges from a few micrometer to a few hundred micrometer [23, 24]. The thickness of melted layer can be adjusted by controlling the laser power intensity and the interaction time. These modified microstructural feature, obtained after laser surface melting, usually lead to stronger and harder alloys with better corrosion resistance.

The possibility of nickel base superalloys undergoing sensitization during heat treatment processes like welding has been already discussed in section 5.1. Now, sensitization can be avoided by solution annealing and rapid cooling through the sensitization temperature range. However, such treatments are very difficult to carry out and almost practically impossible for bulk components like high level waste (HLW) storage tanks in nuclear industries. Large thermal stresses may be induced during such rapid cooling. In such cases, laser surface melting is a suitable method for eliminating sensitization [5] and it is desirable to investigate the corrosion behaviour of materials under laser treated condition. In Chapters 4 and 5, the corrosion resistance of nickel base superalloys was evaluated in the as-received and heat treated condition in simulated HLW medium. In the present Chapter the laser surface melted nickel base superalloys were characterized for their corrosion behaviour in simulated HLW medium.

6.2 Experimental

➢ X-ray diffraction (XRD) patterns of the specimen's surface were recorded using a Philips make X'pert pro diffractometer and compared with those of as-received specimens.

➢ Laser melting was obtained on one surface of the specimen using an indigenous continuous wave CO_2 laser beam. The experimental parameters used for the surface melting have been reported in Table 3.4. In order to form a uniformly melted layer with microstructural and compositional homogeneity on the whole surface of the substrate, each beam scan was overlapped to 50 % of the beam size.

➢ The LSM specimens were mounted with resin and polished up to diamond finish, starting with 600 grit SiC paper. Proper care was taken while polishing so that the exposed surface remained well within the laser melted zone (LMZ).

➢ The LSM specimens were subsequently etched electrolytically and observed under "Camscan make" Scanning electron microscope (SEM). To measure the depth of melting, the specimens were polished in the direction of thickness and electrolytically etched.

➢ Polarization experiments were carried out in simulated nuclear HLW medium at the solution temperature of 25 ^{0}C.

➢ Double loop electrochemical potentiokinetic reactivation (DL-EPR) tests were carried out in 0.5 M H_2SO_4 solution containing 0.0001 M KSCN.

➢ The pitting corrosion resistance of LSM specimens were measured out in 3 M HNO_3 containing various concentrations of chloride ions.

6.3 Results and discussion

6.3.1 Microstructure

Figure 6.1 shows the microstructures of LSM Alloys 600, 690 and 693 after electrolytic etching. A cellular solidified structure was observed for the LSM Alloy 600, 690 and 693. The micrographs in Fig. 6.1 indicated that laser surface melting resulted in fine solidification in the structure of the alloys. This could be attributed to the faster cooling rates, developed as a consequence of the temperature gradients generated in the material [25, 26]. Solidification occurred epitaxially from the boundary between the treated region and the untreated matrix.

The Ti and Cr rich precipitates observed in the microstructure of the as-received specimens and the traces of precipitates observed in the solution-annealed specimens were found to be
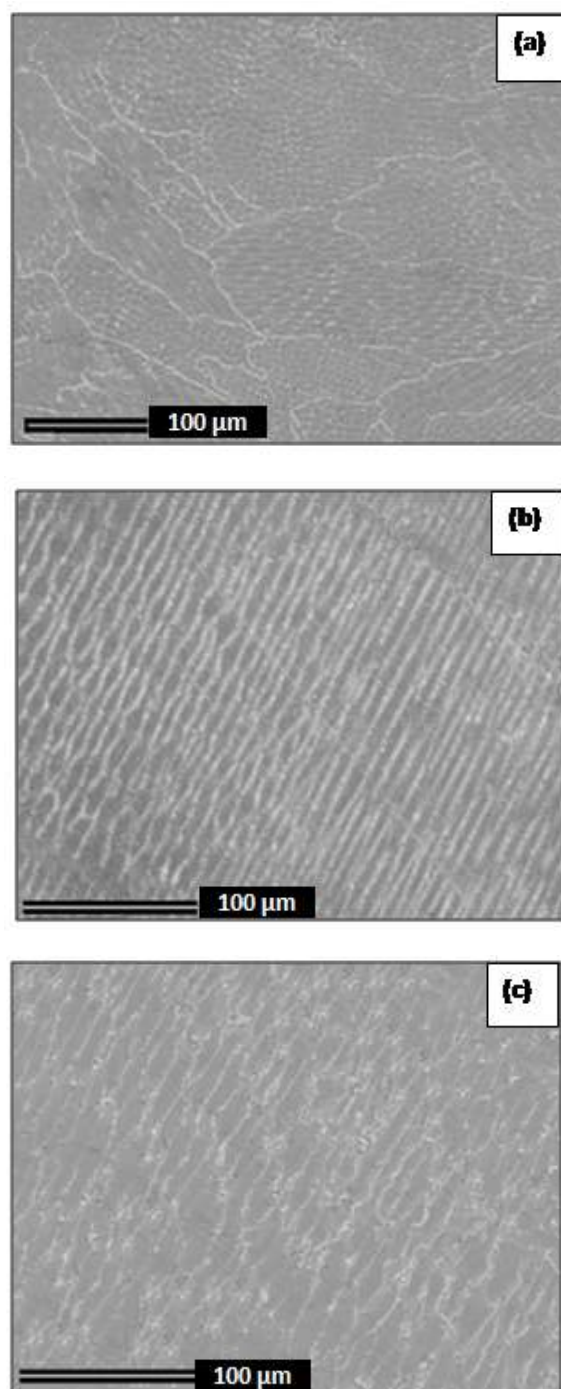

Fig. 6.1: SEM micrographs of LSM (a) Alloy 600, (b) Alloy 690 and (c) Alloy 693

completely absent after laser surface melting, as could be seen in the microstructure [Fig. 6.1]. Owing to the high energy density of laser beam, the pre-existed Ti and Cr-rich carbides have been completely melted and dissolved. Moreover, the Cr-rich carbides were not re-precipitated during cooling due to the high cooling rate during the laser surface melting process [27, 28]. It has been reported by Shin et al. [26] that after laser surface melting of Alloy 600, the percentage of chromium near the grain boundary and in the matrix were the same.

6.3.2 Cross section

To assess the extent of surface melting after laser treatment, the cross sectional optical micrographs of the LSM alloys were taken and are represented in Fig. 6.2. The microstructures showed three distinct zones, namely LMZ, HAZ and an unaffected zone, which is the matrix. It could be seen that the LMZ for Alloy 600 is nearly 600 μm whereas for the Alloys 690 and 693 the zones were nearly 800 and 1000 μm, respectively. In the LMZ, cellular structure was formed due to the rapid solidification, epitaxially from the boundary between the melted region and unmelted region. Similar observations were also reported by Munitz et al. [29] and Shin et al. [26]. In Alloy 600, the HAZ was found to be nearly 200 μm, whereas it was only a few micron in the case of Alloy 690 and 693. In laser surface melting, heating by a laser beam is rapid such that the HAZ is usually very narrow, and is different from conventional heat treatments. The narrow HAZ could be attributed to the high energy density of laser [8]. The melting and solidification occurs simultaneously within a very short interaction time and remains confined only to the top surface and hence,

no change in the microstructure of matrix was observed. The arc observed at the interface of

LMZ and HAZ was due to the overlapping of laser beam tracks of the laser surface melting.
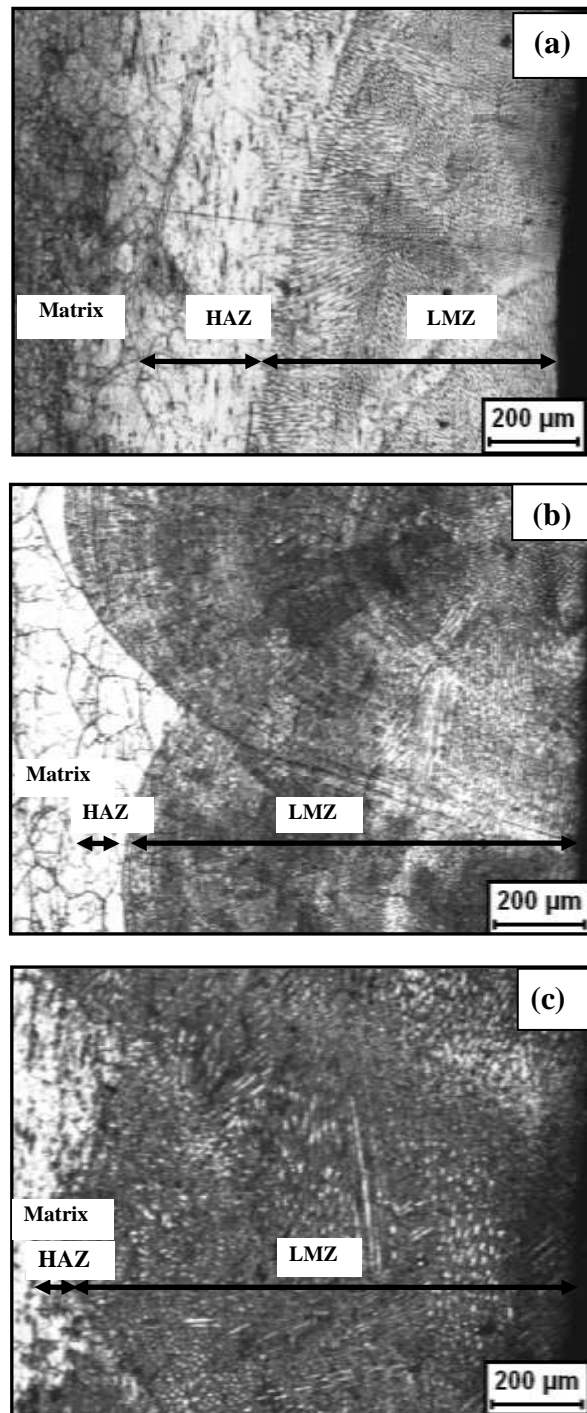
Fig. 6.2: Cross section of LSM (a) Alloy 600, (b) Alloy 690 and (c) Alloy 693

6.3.3 Phase identification by XRD

The XRD patterns of as-received and LSM Alloys 600, 690 and 693 are shown in Fig. 6.3. The lattice constants calculated for different (hkl) planes and d-spacings, using Eq. 6.1 and X'pert plus software for the as-received and LSM specimens are given in Table 6.1.

$$a = d(N)^{1/2} \quad \text{where } N = (h^2 + k^2 + l^2)^{1/2} \tag{6.1}$$
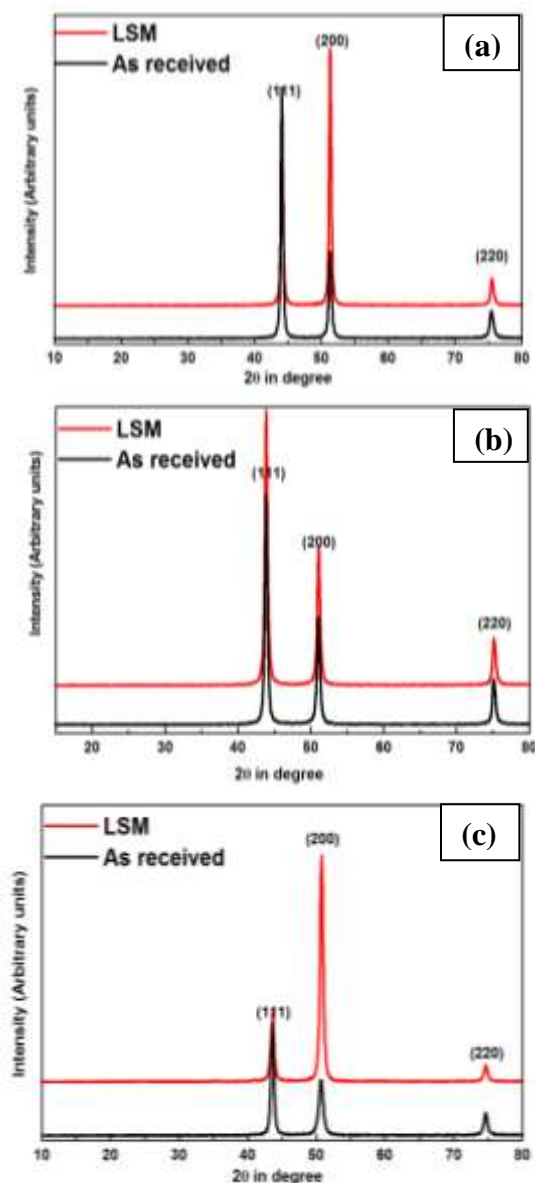
Fig. 6.3: XRD patterns of the as-received and LSM (a) Alloy 600, (b) Alloy 690 and (c) Alloy 693

It is observed from Fig. 6.3 that the as-received and LSM Alloy 600 exhibited the same crystal structure (Cubic and space group: Fm$\bar{3}$m) with the lattice constant (a) of 3.56 A^0. Table 6.1 revelaed that the change in "a" values in the LSM specimens was insignificant when compared to the as-received specimens, which implies that no phase change occurred after laser treatment. Increase in intensity was observed only in (200) reflection, which could be due to the preferred orientation on laser treatment of the surface. Likewise, Alloys 690 and 693 did not show any phase change after laser treatment; however, only an increase in intensity was observed in certain planes.

Table 6.1 Parameters derived from XRD pattern

| Material	Condition	h k l	2θ	d	a
Alloy 600	[a]AR	111	44.02	2.056	3.560
		200	51.25	1.781	3.562
		220	75.41	1.260	3.562
	[b]LSM	110	44.06	2.054	3.557
		200	51.27	1.780	3.561
		220	75.49	1.258	3.559
Alloy 690	AR	111	43.83	2.064	3.579
		200	51.01	1.789	3.578
		220	75.07	1.264	3.576
	LSM	110	43.85	2.063	3.573
		200	51.04	1.788	3.576
		220	75.11	1.264	3.574
Alloy 693	AR	111	43.57	2.076	3.595
		200	50.64	1.801	3.602
		220	74.60	1.271	3.595
	LSM	110	43.57	2.076	3.595
		200	50.73	1.798	3.596
		220	74.63	1.271	3.594

[a]AR: as-received; [b]LSM: laser surface melted specimen

6.3.4 Double loop electrochemical potentiokinetic reactivation (DL-EPR) test

Figure 6.4 shows the DL-EPR curves obtained for the LSM Alloys 600, 690 and 693 in 0.5 M H_2SO_4 containing 0.0001 M KSCN. In the present investigation, the corrosion potential (E_{corr}) of LSM Alloy 600 was found to be 400 mV (SCE) and passivation occurred at 60 mV (SCE). The anodic current density during the forward scanning was generated by grains and grain boundaries, whereas during reactivation the current was generated exclusively from the defective regions of the passive film (Cr depleted zone adjacent to the grain boundaries). Hence, the anodic current density was large and the reactivation current was comparatively low.
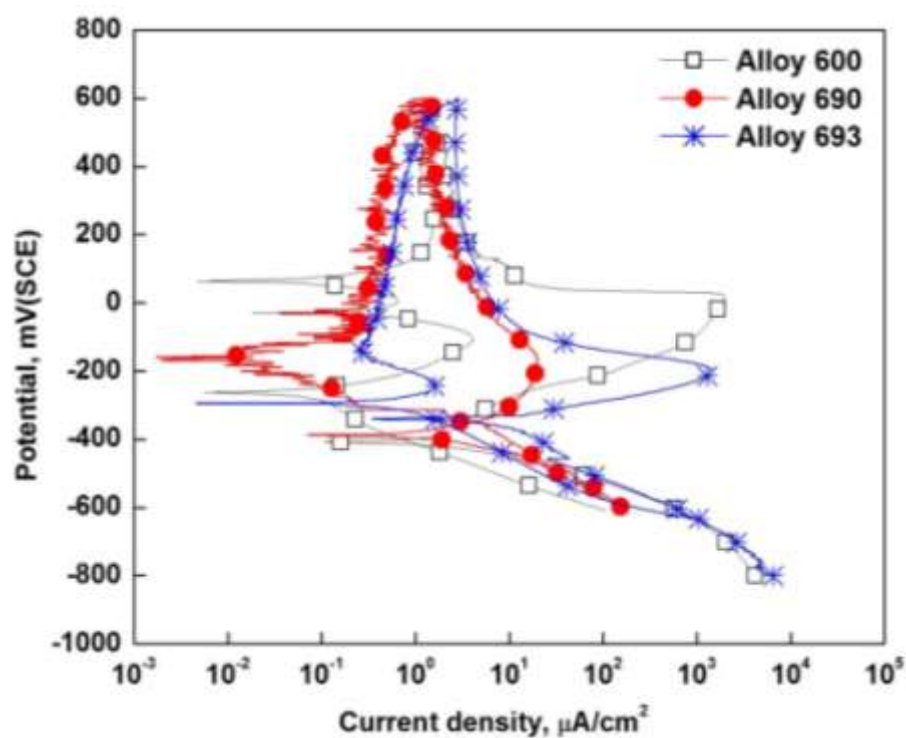

Fig. 6.4: DL-EPR curves of LSM alloys

From the potentiokinetic curves, the degree of sensitization (DOS) of LSM Alloy 600 (using Eq 3.6) was determined to be 0.21%, whereas it was 0.11% for Alloy 693 (Table 6.2). The DOS of the LSM specimens were found to be comparable to that of the solution-annealed specimens. Though the DOS of LSM specimens were observed to be in the same range as that of the solution-annealed specimens, I_a was found to be very low for the LSM specimens as compared to the solution-annealed specimens. The lower I_a value for the LSM specimen indicated the presence of a homogenized microstructure after laser melting and solidification.

Table 6.2 Degree of sensitization of Alloy 600 and Alloy 693

Material	I_r ($\mu A/cm^2$)	I_a ($\mu A/cm^2$)	I_r/I_a	DOS (%)
Alloy 600	4.08	1990	0.0021	0.21
Alloy 693	1.64	1455	0.0011	0.11

In the DL-EPR measurements carried out for Alloy 690, no reactivation peak was observed, which is evident from Fig. 6.4. This could be attributed to the high concentration of chromium and low concentration of carbon in the Alloy. Once the applied potential reached 60 mV (SCE), the passivation was stable throughout the reverse scanning period and hence, no reactivation peak was observed. Therefore, the ratio of I_a to I_f, has been considered as the basis for studying the extent of chromium depletion adjacent to carbide precipitates in Alloy 690 in the present investigation. The ratio of I_a to I_f was found to be less for LSM specimen (13.96) compared to the heat treated specimens (2482 for solution-annealed and 3910 for sensitized). The I_a (20.54 $\mu A/cm^2$) and I_f (1.47 $\mu A/cm^2$) values were also found to be low in the LSM specimen when compared to the solution-annealed specimen (9830 and

3. 96 $\mu A/cm^2$ respectively). These results indicated that during laser surface melting treatment, all the pre-existing Cr-carbide precipitates were dissolved and Cr depleted zones disappeared, resulting in the formation of a homogeneous solid solution.

6.3.5 Electrochemical impedance spectroscopic studies in simulated HLW medium

The electrochemical impedance spectroscopic results for the LSM nickel base alloys obtained at the open circuit potential (OCP) in simulated HLW medium are represented in Fig. 6.5 in the form of Nyquist plots. The experimental data from Fig. 6.5 were fitted in to Randles circuit with the elemental arrangement of R_S (CPE $\|$ R_P), where R_S is the solution resistance, R_P is the polarization resistance and CPE is the constant phase element. The electrochemical parameters derived after fitting are listed in Table 6.3 and the same parameters for as-received, soution annealed and sensitized specimens are mentioned in the Table for comparison.

For all the three alloys, one depressed semicircle over the entire frequency range was observed and they are characteristics of capacitive behaviour, which is attributed to the charge transfer process at the electrode/electrolyte interface [30-32].

All the alloys showed higher R_P values for the LSM specimens compared to the as-received as well as heat treated specimens implying superior corrosion resistance in HLW medium. The higher R_P values for the LSM specimens could be due to the increased stability of the passive oxide layer with the formation of homogeneous and uniform oxide of chromium or nickel or both. The values of the CPE parameter which represent the double layer capacitance of the film/electrolyte interface, are relatively lower in the LSM specimens than the as-received and heat treated specimens for all the alloys. This indicated that there was

less ion adsorption had occurred on the surface of the LSM specimens, thereby providing better corrosion resistance.
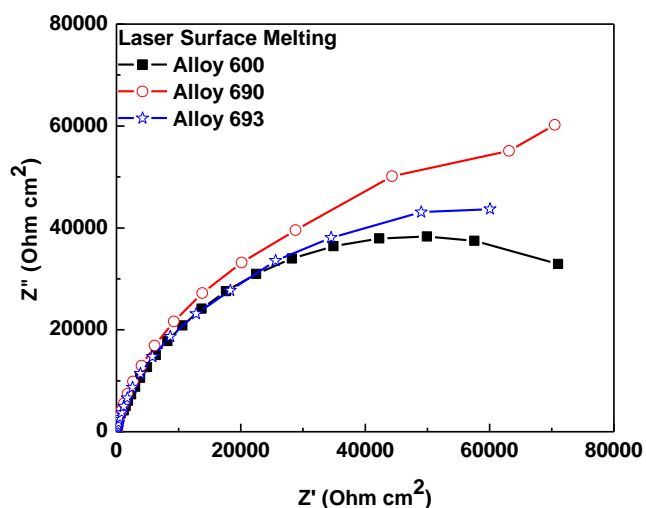
Fig. 6.5: Nyquist plots for the LSM specimens

Table 6.3 Electrochemical parameters derived from EIS curves for LSM, AR, SEN and SA alloys

Material		$\mathbf{R_s}$ $(\Omega\ \mathbf{cm^2})$	$\mathbf{R_p}$ $(\mathbf{k\Omega\ cm^2})$	**CPE** $(\mathbf{F\ cm^{-2}\ S^n})$	**n**
Alloy 600	LSM	0.65	90	60.3×10^{-6}	0.881
	AR	1.90	0.100	37.5×10^{-6}	0.885
	SEN	1.9	0.101	39.5×10^{-6}	0.885
	SA	2.0	2.14	73.7×10^{-6}	0.876
Alloy 690	LSM	0.6	141.6	74.6×10^{-6}	0.862
	AR	0.45	35.4	57.9×10^{-6}	0.786
	SEN	0.45	35.4	72.2×10^{-6}	0.786
	SA	1.00	90	35.2×10^{-6}	0.871
Alloy 693	LSM	0.5	108.5	86.8×10^{-6}	0.846
	AR	1.30	18.5	52.1×10^{-6}	0.911
	SEN	1.30	23.5	54.5×10^{-6}	0.911
	SA	1.0	90	60.3×10^{-6}	0.933

Among the three LSM alloys, Alloy 600 showed lower R_P value compared to Alloy 690 and 693, which could be due to the compositional variation. The higher percentage of chromium in Alloy 690 and 693 make the passive film stable and hence, exhibit superior corrosion resistance.

6.3.6 Potentiodynamic anodic polarization in simulated HLW

The potentiodynamic anodic polarization curves for LSM Alloy 600, 690 and 693 in simulated HLW at the solution temperature of 25 ^{0}C are shown in Fig. 6.6. The polarization curves for as-received and heat treated specimens are also represented for comparison. The electrochemical parameters, E_{corr}, I_{pass}, E_{TP} and passive range, derived from the polarization curves are reported in Table 6.4. The polarization curve for the LSM Alloy 600 was found to be characterized by the E_{corr} value of 280 mV (SCE). The specimen passivated spontaneously in simulated HLW medium without exhibiting any active to passive transition. The material was found to be passive over a wide range of potential (507 mV (SCE)), before transpassive dissolution occurred at 870 mV (SCE). The specimen was found to possess an I_{pass} of 0.9 $\mu A/cm^2$.

Alloy 690 was characterized with the E_{corr} value of 360 mV (SCE), which was nobler than Alloy 600. For Alloy 693, the E_{corr} was found further nobler at 390 mV (SCE). All the specimens were characterized with I_{pass} in the range 1.0 $\mu A/cm^2$.

The LSM specimens showed an improvement in the corrosion resistance in simulated HLW compared to all the as-received specimens, while the corrosion resistance was found to be comparable to that of the solution-annealed specimens. The improvement in corrosion behaviour of LSM specimens as compared to that of the as-received specimens could be

attributed to the elimination of microstructural inhomogenities such as precipitates, inclusions, impurity segregation and the chromium depleted zone along the grain boundaries after laser surface melting. However, all the LSM alloys exhibited similar corrosion behaviour in the simulated HLW medium irrespective of their compositional differences. This could be due to the highly passivating nature of the specimens in 3 M HNO_3 solution. The specimens got passivated spontaneously in the medium and the cations present in 3 M HNO_3 (simulated HLW) had almost no deleterious effect on the corrosion resistance.
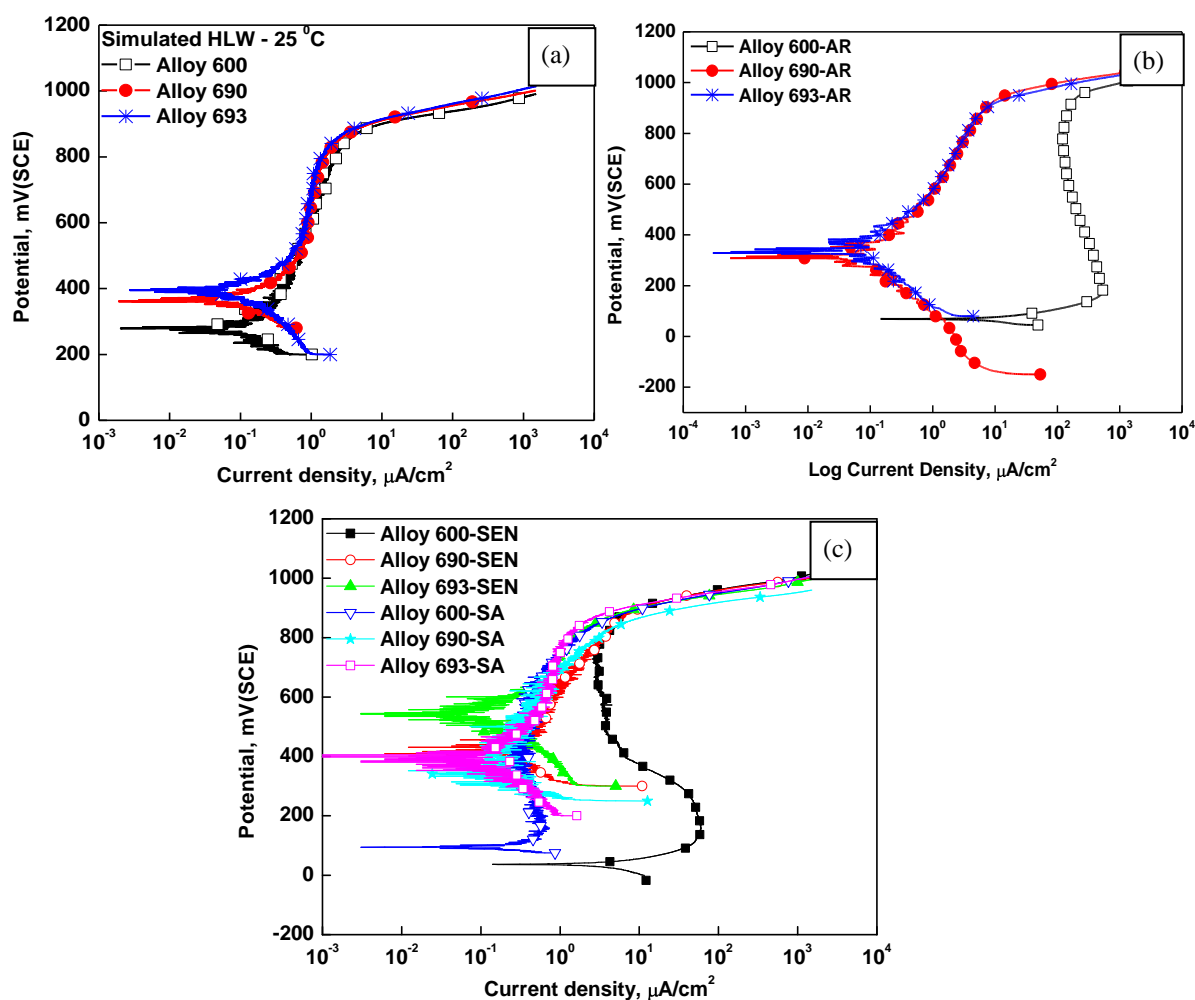

Fig. 6.6: Polarization curves of (a) LSM specimens (b) As-received (c) Heat treated specimens in simulated HLW medium

Table 6.4 Electrochemical parameters derived from polarization curves at 25 ^{0}C.

Material		E_{corr}	I_{pass}	E_{TP}	Passive range
Alloy 600	LSM	280	0.9	870	570
	AR	68	170	900	710
	SEN	04	4.0	860	700
	SA	90	0.4	820	650
Alloy 690	LSM	360	1.0	870	460
	AR	329	2	930	490
	SEN	400	1.3	880	400
	SA	350	0.75	850	480
Alloy 693	LSM	390	0.9	870	420
	AR	376	2	930	467
	SEN	540	1.0	850	250
	SA	400	0.8	870	340

*All potentials are in mV (SCE) and currents in µA/cm^2

6.3.7 Pitting corrosion resistance in acid-chloride medium

Figure 6.7(a-c) shows the polarization curves of LSM Alloys 600, 690 and 693 in 3 M

HNO$_3$ containing different concentrations of chloride ions (500, 1000, 2000, 3000 ppm) at

25 ^{0}C. The electrochemical parameters E_{corr}, I_{pass} and E_{pit} obtained from this figure are

reported in Table 6.

From the graphs, it could be observed that the LSM 600 specimens did not show any active

dissolution and exhibited spontaneous passivation during anodic polarization in the acid-

chloride medium unlike the behaviour observed with as-received and heat treated conditions.

Alloys 690 and 693 also exhibited spontaneous passivation in the acid-chloride media. An

increase in E_{corr} was observed for all the LSM specimens compared to the as-received and

heat treated specimens. This could be attributed to the higher thermodynamic stability of the

laser treated specimen at the open circuit condition. However, a decrease in E_{corr} was observed with increase in chloride ion concentration in the acid-chloride medium.

The E_{pit} values were high for all the three LSM specimens. Increasing the chloride ion concentration in the electrolyte did not affect the E_{pit} and remained in the same range upto 3000 ppm. The E_{pit} values were higher for Alloy 600 specimen after laser surface melting compared to the as-received and heat treated specimens. The superior pitting corrosion resistance of the LSM specimens could be due to the dissolution of precipitates after laser treatment and the formation of homogenous microstructure with less pit initiation sites like precipitates, inclusions etc.

Table 6.5 Electrochemical parameters of LSM specimens in acidic-chloride medium

Material	Chloride (ppm)	E_{corr}	I_{pass}	E_{pit}
Alloy 600	500	270	0.6	945
	1000	235	0.6	945
	2000	235	0.7	940
	3000	185	0.7	940
Alloy 690	500	280	0.8	955
	1000	280	0.8	950
	2000	235	0.9	940
	3000	150	1.0	940
Alloy 693	500	260	0.6	940
	1000	260	0.7	940
	2000	240	0.7	940
	3000	160	1.0	940

All potential in mV (SCE) and current in $\mu A/cm^2$

The optical micrographs of the LSM specimens after potentiodynamic polarization studies in the acid-chloride medium are given in Fig. 6.8. It is evident from the micrographs that the LSM specimens possessed very few micropits even at the current density of 1.5 mA/cm^2 at the E$_{pit}$.
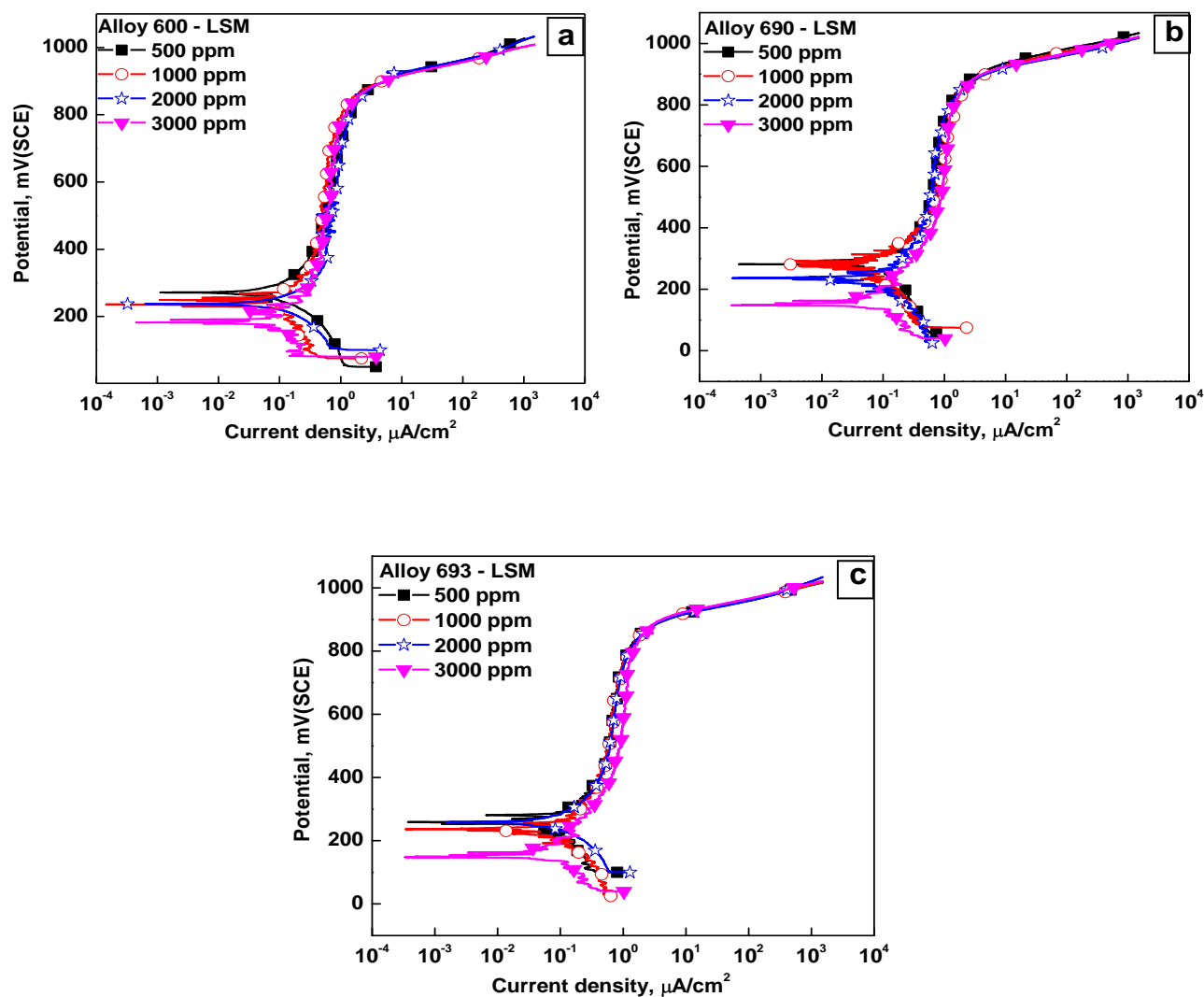

Fig. 6.7: Polarization curves of LSM specimens in acid-chloride medium: (a) Alloy 600, (b) Alloy 690 and (c) Alloy 693
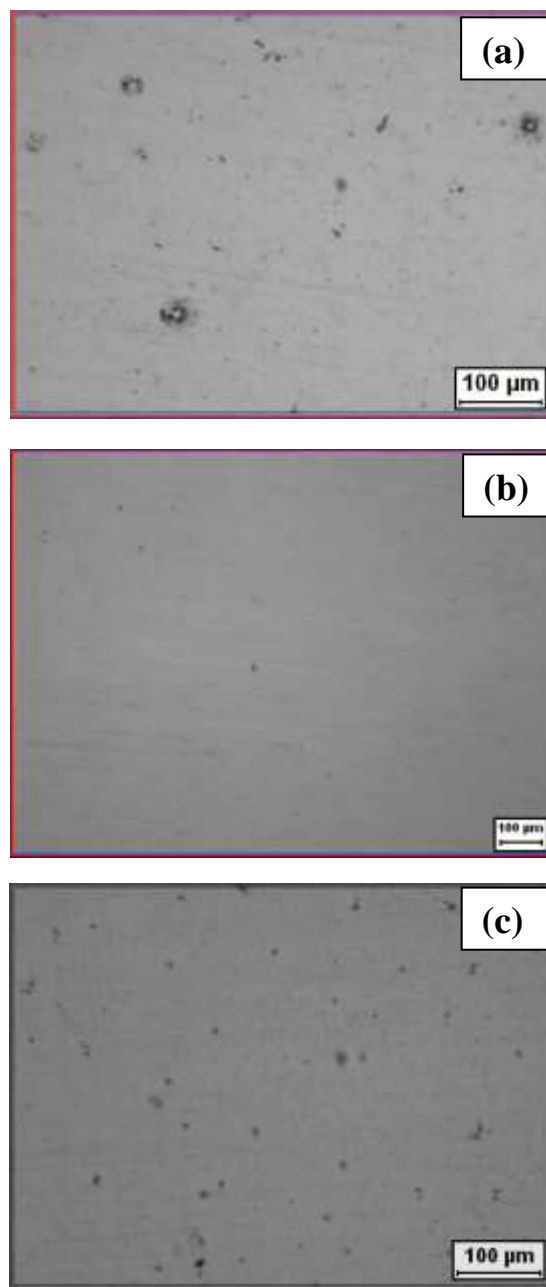
Fig. 6.8: Micrographs of the LSM specimens after pitting corrosion study (a) Alloy 600, (b) Alloy 690 and (c) Alloy 693 in 3 M HNO$_3$ with 3000 ppm chloride ions

6.4 Conclusions

➢ Laser surface melting of the nickel base alloys 600, 690 and 693 resulted in cellular microstructure without any precipitates. These alloys were found to possess the same cubic crystal structure in both as-received and LSM condition.

➢ DL-EPR test revelaed low DOS for the LSM specimens, indicating the non-existence of chromium depleted zones after laser surface melting.

➢ Though all the three LSM alloys exhibited similar corrosion resistance in simulated HLW at 25 ^{0}C, an improved corrosion resistance was observed for LSM alloys compared to as-received and solution-annealed specimens.

➢ An improvement in pitting corrosion resistance was observed after laser surface melting, compared to the alloys in as-received and heat treated condition, which could be due to the refinement of microstructure and dissolution of precipitates and inclusions which are the pit initiation sites.

References:

1. D. Dube, M. Fiset, A. Couture, I. Nakatsugawa, Mater. Sci. Eng. A, 299 (2001) 38.

2. S. K. Das, C. F. Chang: in 'Rapidly Solidified Crystalline Alloys', (ed. S.K. Das et al.), 137-156; 1985, Warrendale, PA, The Metallurgical Society.

3. Z. D. Cui, H. C. Man, F. T. Cheng, T. M. Yue, Surf. Coat. Tech., 162 (2003) 147.

4. A. Viswanathan, D. Sastikumar, U. Kamachi Mudali, H. Kumar, A. K. Nath, Surf. Eng., 33 (2007) 123.

5. C. T. Kwok, K. H. Lo, W. K. Chan, F. T. Cheng, H. C. Man, Corros. Sci., 53 (2011) 1581.

6. R. Vilar, E. C. Santos, P. N. Ferreira, N. Franco, R. C. Da Silva, Acta Mater., 57 (2009) 5292.

7. J. D. Majumdar, R. Galun, B. L. Mordike, I. Manna, Mater. Sci. Eng. A, 361 (2003) 119.

8. C. W. Draper, J. M. Poate, Int. Met. Rev., 30 (1985) 85.

9. W. Darmawan, J. Quesada, R. Marchal, Surf. Eng., 23 (2007) 112.

10. A. R. Shankar, B. J. Babu, R. Sole, U. Kamachi Mudali, H. S. Khatak, Surf. Eng., 23 (2007) 147.

11. C. Huang, Y. Zhang, R. Vilar, J. Shen, Mater. Design, 41 (2012) 338.

12. A. Conde, R. Colaco, R. Vilar, J. de Damborenea, Mater. Design, 21 (2000) 441.

13. B. S. Yilbas, M. Khaled, M. A. Gondal, Opt. Laser. Eng., 36(2001) 269.

14. U. Kamachi Mudali, R. K. Dayal, J. B. Gnanamoorthy, S. M. Kanetkar, S. B. Ogale, Mater. Trans. JIM, 31 (1991) 845.

15. C. Jufang, L. Xingcheng, L. Renxing, S. Laidi, Appl. Mech. Mater., 33 (2010) 607.

16. R. G. Li, J. An, Y. Lu, Surf. Eng., 26 (2010) 347.

17. S. M. Shariff, T. K. Pal, G. Padmanabham, S. V. Joshi, Surf. Eng., 26 (2010) 199.

18. J. D. Majumdar, A. K. Nath, I. Manna, Surf. Coat. Tech., 204 (2010) 1321.

19. N. Parvathavarthini, R. K. Dayal, R. Sivakumar, U. Kamachi Mudali, A. Bharti, Mater. Sci. Tech., 8 (1992) 1070.

20. U. Kamachi Mudali, R.K. Dayal, J. Mater. Eng. Perform., 1 (1992) 341.

21. C. Y. Cui, X. G. Cui, Y. K. Zhang, Q. Zhao. J. Z. Lu, J. D. Hu, Y. M. Wang, Surf. Coat. Tech., 206 (2011) 1146.

22. R. Colaco, R. Vilar, Mater. Sci. Eng. A, 385 (2004) 123.

23. Z. Liu, H. Liu, F. Viejo, Z. Aburas, M. Rakhes, J. Mech. Eng. Sci., 224 (2010) 1073.

24. R. Li, M. G. S. Ferreira, A. Almeida, R. Vilar, K. G. Watkins, M. A. McMohan, W.M. Steen, Surf. Coat. Tech., 81 (1996) 290.

25. S. C. M. d'Oliveira, R. S. C. Paredes, F. P. Weber, R. Vilar, Mater. Res., 4 (2001) 93.

26. J. K. Shin, J. H. Suh, J. S. Kim, S-J. L Kang, Surf. Coat. Tech., 107 (1998) 94.

27. Y. S. Lim, H. P. Kim, J. S. Kim, H. S. Kwon, Key Eng. Mater., 183-187 (2000) 595.

28. Y. S. Lim, J. H. Suh, I. H. Kuk, J. S. Kim, Metall. Trans. A 28 (1997) 1223.

29. A. Munitz: Metall. Trans B, 16 (1985) 149.

30. A. A. Hermas, M. S. Morad, Corros Sci., 50 (2008) 2710.

31. S. Ningshen, U. Kamachi Mudali, G. Amarendra, Baldev Raj, Corros. Sci., 51(2009) 322.

32. S. Ningshen, U. Kamachi Mudali, P. Mukherjee, A. Sarkar, P. Barat, N. Padhy, Baldev Raj, Corros. Sci., 50 (2008) 2124.

CHAPTER 7

Conclusions, Summary and Scope for Future Work

Conclusions, Summary and Scope for Future Study

This Chapter gives the salient conclusions drawn from the results of the investigations carried out on the corrosion behaviour of three nickel base superalloys viz. Alloy 600, Alloy 690 and Alloy 693 (under various metallurgical conditions of the materials) for nuclear high level waste storage application. Apart from this, a summary and scope for further studies which may be carried out in future for understanding the corrosion behaviour of these alloys in various waste storage conditions are also provided in this Chapter.

7.1 Summary

The major conclusions drawn from the investigation of the corrosion behaviour of nickel base superalloys (Alloys 600, 690 and 693) in the as-recevied, heat-treated and laesr surface modifications are listed below:

(a) As-received alloys

➢ At ambient conditions, all the three nickel base alloys were found to possess good corrosion resistance in 3 M HNO_3 and simulated HLW solution. Passivation occurred in Alloy 600 after an initial active dissolution, whereas Alloys 690 and 693 were passivated spontaneously without showing any active-passive transition. The passive films formed over the specimens were observed to be stable over a wide potential range. Increasing the solution temperature to 50 ^{0}C increased the passivation current density, indicating a decrease in corrosion resistance, however all the three alloys exhibited wide passive range.

➤ Microstructural characterization using SEM attached with EDS, revealed the presence of few precipitates at and adjacent to the grain boundary in the austenitic structure for all the three alloys. Alloy 690 exhibited significant twin boundaries.

➤ Thin layer of oxides of chromium-nickel-iron formed on the surface, after electrochemical passivation of Alloy 690 and Alloy 693 in simulated HLW was ascertained from XPS studies. Alloy 600 was found to consist of a film of oxides of chromium only, after pasivation.

➤ The alloys indicated high pitting potential and exhibited pits of various sizes and the population of pits increased with increase in chloride concentration. However, Alloy 690 exhibited only few micropits even in 3 M HNO_3 containing 3000 ppm chloride ions.

➤ Alloy 690 in the as-received condition showed superior intergranular corrosion resistance compared to Alloy 693 followed by Alloy 600.

(b) Heat treated alloys

Following are the major conclusions drawn from the investigation of the corrosion behaviour of the nickel base superalloys under heat treated (solution-annealed and sensitized) conditions:

➤ SEM analysis revealed that most of the pre-existing precipitates were dissolved after solution annealing, though few precipitates were observed on the specimens. The sensitized specimens were found to possess Cr depleted regions on the areas adjacent to grain boundaries, in addition to some TiN precipitates in the matrix.

➢ The degree of sensitization was estimated for the alloys in 0.5 M H_2SO_4 containing 0.0001 M KSCN. Low degree of sensitization was observed in the solution-annealed specimens compared to the sensitized specimens. Alloy 690 did not show any reactivation peak due to the high chromium and low carbon content in its composition.

➢ All the alloys possess good corrosion resistance in 3 M HNO_3 and simulated HLW at 25 ^{0}C, in the solution-annealed condition. With the increase in solution temperature to 50 ^{0}C, the corrosion potential as well as passivation current denisity were found to increase.

➢ The sensitized specimens possessed lower corrosion resistance compared to solution-annealed specimens in both 3 M HNO_3 and in simulated HLW. However, the passivation current densities were found to be in close proximity.

➢ Alloy 690 exhibited excellent pitting as well as intergranular corrosion resistance in both solution-annealed and sensitized conditions.

(c) Laser surface melted alloys

➢ Laser surface melting of the nickel base alloys resulted in cellular microstructure without any precipitates. These alloys were found to possess the same crystal structure in both as-received and LSM conditions.

➢ DL-EPR test showed low degree of sensitization for the laser surface melted specimens, indicating the non-existence of chromium depleted zones after laser surface melting.

➢ Though all the three laser surface melted alloys exhibited similar corrosion resistance in simulated HLW at 25 ^{0}C, an improvement in the corrosion resistance was observed for LSM alloys compared to as-received and heat treated specimens.

➢ Improvement in pitting corrosion resistance also was observed after laser surface melting, compared to the alloys in as-received and heat treated conditions. This could be due to the refinement of microstructure and dissolution of precipitates which are the initiation sites for pitting.

7.2 Conclusions

The results of the present investigation on the "Corrosion behaviour of materials for the nuclear high level waste storage application", employing electrochemical studies and surface morphological and analytical examinations could be summarized as follows.

Investigations on the corrosion behaviour of nickel base alloys, namely Alloys 600, 690 and 693 were performed in 3 M HNO_3 and simulated HLW solution and in different concentrations of chloride ions in the as-received, various heat-treated (solution-annealed and sensitized) as well as in laser surface melted conditions. Though all the three alloys showed good corrosion resistance in 3 M HNO_3 and simulated HLW medium, Alloy 690 was found to possess better corrosion resistance compared to Alloy 693 followed by Alloy 600. Solution-annealing aided in improving the corrosion resistance of the alloys. Laser surface melting had enhanced the general as well as pitting corrosion resistance of all the alloys. Among the alloys studied, Alloy 690 was found to possess excellent intergranular corrosion resistance compared to Alloy 600 and Alloy 693, which could be attributed to the higher chromium content and lower carbon content. The corrosion resistance of the alloys investigated in the present thesis work followed the order:

Laser surface melted > Solution-annealed > As-received > Sensitized

and the Alloys follows the order:

Alloy 690 > Alloy 693 > Alloy 600

7.3 Scope for future study

➢ To ensure the desired lifetime of the high active waste storage tanks, the welded zone of the tanks should have a corrosion resistance similar to that of the parent material. Detailed investigations of the weld is essential because welding causes changes in the microstructure of the material and generate tensile stresses in the welded region and heat-affected zone, which can cause unfavourable corrosion behaviour of the welded material. Therefore, the nickel base alloys (Alloys 600, 690 and 693) investigated for this thesis work in simulated high level waste medium requires to be evaluated under welded condition.

➢ Since online monitoring of corrosion behaviour can be realized from electrochemical noise measurements, electrochemical probes based on this technique can be adopted for evaluating the influence of temperature, acid concentration and oxidizing ions present in HLW on the corrosion propagation of the alloys in the waste storage conditions.

➢ Owing to the high burn-up of FBR fuels, the concentration of fission products is much higher in the HLW generated from the reprocessing of FBR spent fuels. Hence, studying the corrosion behaviour of nickel base alloys in the HLW of spent fuels of FBRs and identifying cost-effective corrosion resistant materials for the long term storage of waste in acid medium solutions of different concentrations are necessary.